

Tectonic consequences of mid-ocean ridge evolution and subduction

Joanne Whittaker

2008

Submitted in fulfilment of the requirements
for the degree of Doctor of Philosophy

Division of Geology and Geophysics
School of Geosciences
The University of Sydney, NSW, 2006
Australia

Declaration

I declare that this thesis is less than 80,000 words in length, and that the work contained in this thesis has not been submitted for a higher degree at any other university or institution.

Joanne Whittaker
March, 2008

Preface

This Ph.D. thesis consists of a series of papers published as internationally peer-reviewed journal articles, book chapter volumes or prepared for submission to an internationally peer-reviewed journal. The publications are appropriate to the discipline of geology and geophysics and form part of an integrated project in marine geophysics. The thesis contains an introductory section outlining the topic of the thesis with a summary of the work conducted. Common themes in the papers are tied together in the discussion and conclusion section of the thesis.

Acknowledgments

There are many people who helped me throughout the course of my PhD both at the University of Sydney and outside of university life. Your academic support and friendship has made my PhD years a wonderful, enjoyable and fulfilling period. Especially, I would like to sincerely thank my supervisor, Dietmar Müller, for his outstanding, enthusiastic supervision and friendship throughout the course of my PhD. His vision, guidance, technical expertise, and ability to teach made my PhD so much better than I ever thought it could be.

Abstract

Mid-ocean ridges are a fundamental but insufficiently understood component of the global plate tectonic system. Mid-ocean ridges control the landscape of the Earth's ocean basins through seafloor spreading and influence the evolution of overriding plate margins during mid-ocean ridge subduction. The majority of new crust created at the surface of the Earth is formed at mid-ocean ridges and the accretion process strongly influences the morphology of the seafloor, which interacts with ocean currents and mixing to influence ocean circulation and regional and global climate. Seafloor spreading rates are well known to influence oceanic basement topography. However, I show that parameters such as mantle conditions and spreading obliquity also play significant roles in modulating seafloor topography. I find that high mantle temperatures are associated with smooth oceanic basement, while cold and/or depleted mantle is associated with rough basement topography. In addition spreading obliquities greater than $> 45^\circ$ lead to extreme seafloor roughness. These results provide a predictive framework for reconstructing the seafloor of ancient oceans, a fundamental input required for modelling ocean-mixing in palaeoclimate studies. The importance of being able to accurately predict the morphology of vanished ocean floor is demonstrated by a regional analysis of the Adare Trough, which shows through an analysis of seismic stratigraphy how a relatively rough bathymetric feature can strongly influence the flow of ocean bottom currents.

As well as seafloor, mid-ocean ridges influence the composition and morphology of overriding plate margins as they are consumed by subduction, with implications for landscape and natural resources development. Mid-ocean ridge subduction also effects the morphology and composition of the overriding plate margin by influencing the tectonic regime experienced by the overriding plate margin and impacting on the volume, composition and timing of arc-volcanism. Investigation of the Wharton Ridge slab window that formed beneath Sundaland between 70 Ma and 43 Ma reveals that although the relative motion of an overriding plate margin is the dominant force effecting tectonic regime on the overriding plate margin, this can be overridden by extension caused by the underlying slab window.

Mid-ocean ridge subduction can also affect the balance of global plate motions. A long-standing controversy in global tectonics concerns the ultimate driving forces that cause periodic plate reorganisations. I find strong evidence supporting the hypothesis that the plates themselves drive instabilities in the plate-mantle system rather than major mantle overturns being the driving mechanism. I find that rapid sub-parallel subduction of the Izanagi mid-ocean ridge and subsequent catastrophic slab break off likely precipitated a global plate reorganisation event that formed the Emperor-Hawaii bend, and the change in relative plate motion between Australia and Antarctica at approximately 50 Ma.

This thesis is based on the following papers:

Paper1:

The Origins of Seafloor Roughness, prepared for submission to Nature

Paper2:

Whittaker, J.M. and Müller, R.D., (2006) Seismic stratigraphy of the Adare Trough area, Antarctica. *Marine Geology*, 230(3-4): 179-197

Paper3:

Whittaker, J., Müller, R.D., Sdrolias, M. and Heine, C., (2007) Sunda-Java trench kinematics, slab window formation and overriding plate deformation since the Cretaceous, *Earth and Planetary Science Letters*. 255: 445-457

Paper4:

Whittaker, J. M., Müller, R.D., Leitchenkov, G., Stagg, H., Sdrolias, M., Gaina, C. and Goncharov, A. (2007) Major Australian-Antarctic Plate Reorganisation at Hawaiian-Emperor Bend Time, *Science*. 318: 83-86

Contents

1	Introduction	1
1.1	Background	1
1.2	Scope of Thesis	1
1.3	Data and Methodology	2
1.4	Overview of Thesis	3
2	Paper 1: Paper prepared for submission to Nature	5
3	Paper 2: Whittaker et al. Marine Geology, 2006	15
4	Paper 3: Whittaker et al. EPSL 2007	35
5	Paper 4: Whittaker et al. Science 2007	49
6	Discussion	55
7	Conclusion	61
8	References	63
A	Paper 1 Supplementary Material	67
B	Paper 4 Supplementary Material	83
C	Co-author contribution forms	99

Chapter 1

Introduction

1.1 Background

Mid-ocean ridges are a critical component of the Earth's geological system where new oceanic crust is created from upwelling magma between diverging tectonic plates. The composition and morphology of the seafloor, which interacts with ocean currents to influence ocean circulation and climate, is critically dependent on processes determining the manner and composition of crustal accretion at mid-ocean ridges. Mid-ocean ridges can be subducted and once subducted the process of crustal accretion ceases as magma is no longer able to solidify onto the edges of the diverging plate margins. The presence of an underlying slab window influences heat flow, tectonic regime, and the volume and type of volcanic activity on the over-riding plate.

Seafloor spreading is a relatively stable geological process, with mid-ocean ridges continuously existing over tens of millions of years. The process of seafloor spreading accretes new oceanic crust to the trailing edges of diverging plate margins from upwelling mantle. A number of different factors combine to determine the morphology and composition of newly formed oceanic crust including the temperature and composition of the underlying mantle e.g. [Klein, 1985], seafloor spreading rates e.g. [Malinverno, 1991; Small and Sandwell, 1989; Smith, 1998], and spreading obliquity e.g. [de Alsteris, et al., 1998], which is the difference between the regional direction of plate motion and the normal to the regional strike of a mid-ocean ridge. The morphology of the seafloor is fundamental to controlling circulation and mixing in the oceans, processes that ultimately effect global climate.

Mid-ocean ridges can be destroyed at sub-

duction zones. Subduction of a mid-ocean ridge occurs when the rate of crustal accretion is slower than the rate at which the subduction zone is consuming oceanic crust. Subduction of a mid-ocean ridge can lead to formation of a slab window beneath the overriding plate [Dickinson and Snyder, 1979; Thorkelson, 1996]. Slab windows develop when magma continues to form between two diverging down-going plates but does not solidify onto the trailing plate edges, which also become hot and may begin to melt [Dickinson and Snyder, 1979]. The presence of an underlying slab window may lead to extension in an over-riding plate due to the presence of an underlying relatively hot and less viscous mantle wedge [Billen and Gurnis, 2001], as well as a change in the chemical composition, volume and range of arc volcanism, with complete cessation of arc volcanism possible [Thorkelson, 1996].

Subduction of a mid-ocean ridge may upset the balance of global plate tectonic motions leading to changes in rates and directions of motions as the ridge push force from the mid-ocean ridge is replaced by the slab-pull force of the mid-ocean ridge consuming subduction zone.

1.2 Scope of Thesis

This thesis investigates mid-ocean ridges at all stages of the mid-ocean ridge life-cycle, from the first formation of a mid-ocean ridge with the onset of seafloor spreading, through mature steady-state seafloor spreading, to the cessation of spreading and mid-ocean ridge subduction. Each study aims to understand not only the plate tectonic motions acting in the evolution of each particular spreading system but also to understand the influence each stud-

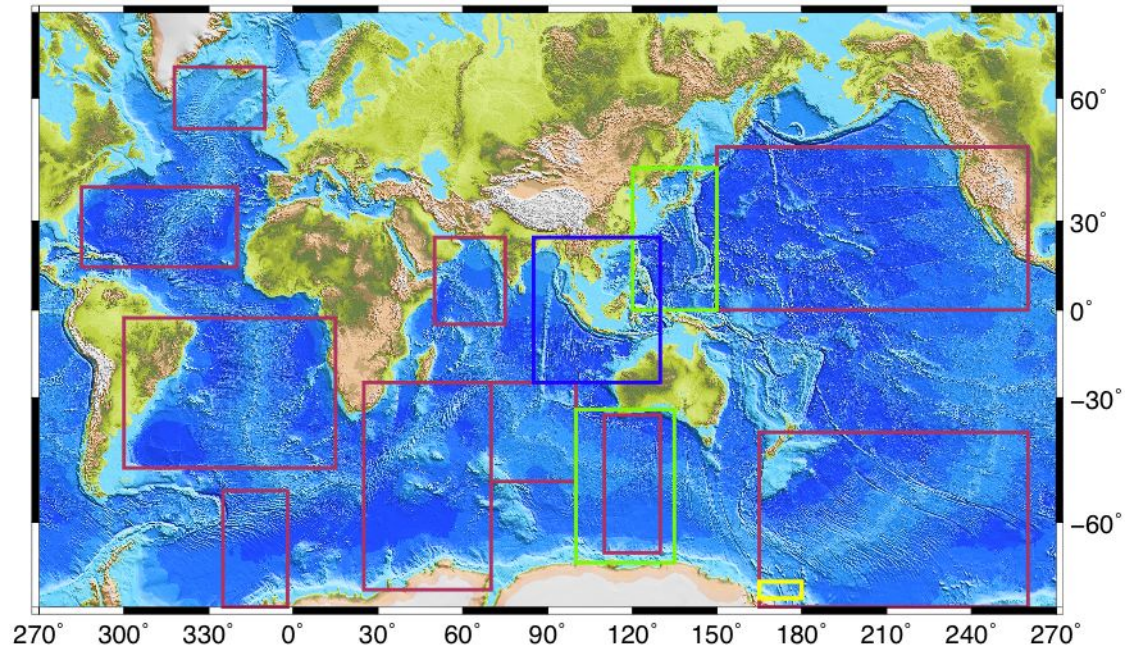


Figure 1.1: Areas studied in each paper shown in yellow (paper 1), maroon (paper 2), blue (paper 3), and green (paper 4)

ied mid-ocean ridge has on the crust it creates or alters and on other processes such as ocean circulation, heat transportation, and resource development.

The role of parameters such as seafloor spreading, spreading obliquity, and mantle conditions in influencing the morphology of newly accreted crust is examined Paper 1. Paper 2 uses seismic stratigraphy to explore how the rough bathymetry of the Adare Trough, a failed Tertiary mid-ocean ridge, interacts with ocean currents. The geological repercussions for the overriding Sundaland margin arising from the subduction of the Wharton mid-ocean ridge and subsequent slab window formation are investigated in paper 3. Paper 4 explores plate tectonic repercussions of subduction of the Izanagi mid-ocean ridge, and also presents a new plate reconstruction for the early slow, oblique opening between Australia and Antarctic.

In particular, I aim to examine the role and influence of mid-ocean ridges on the global geological system through investigating the plate kinematics involved in forming, maintaining and destroying mid-ocean ridges, but also by examining how mid-ocean ridges influence other Earth processes. This includes investigating (1) the influence of spreading rate, sedi-

ment thickness, spreading obliquity and mantle temperature and fertility on the morphology of oceanic crust, (2) how a rough, linear bathymetric feature interacts the oceanic processes to influence the flow of ocean current, (3) the effect of mid-ocean ridge subduction on the topography and geology of an overriding continental margin, and (4) the role of mid-ocean ridge subduction in sparking plate tectonic re-organisations.

1.3 Data and Methodology

Several data types and sources were utilised in this thesis. The specifications of the data, as well as the methodologies used, are detailed in each individual chapter.

All papers use various versions of a palaeo-age grid and associated plate kinematic model originally published by Müller et al. [1997] and updated by new plate kinematic models in Müller et al. [2008] (paper 1), Brown et al. [2006] (Paper 2), Heine et al. [2004] (Paper 3), and Gaina and Müller [2007] (Paper 4). In all cases the plate kinematic models were based in a moving hotspot reference frame from O'Neill et al. [2005].

Paper 1 uses the palaeo-age grid in conjunction with a half-spreading rate [Müller, et

al., 2008] grid to compute spreading obliquity grids, the angle between regional plate motion and the normal to the strike of the associated mid-ocean ridge, for ten spreading systems globally. Paper 1 also uses a 2-minute gravity anomaly grid downward continued onto the seafloor based on Sandwell and Smith [2005] to create a root mean square marine gravity roughness grid using a 100 km wide Gaussian filter with seamounts [Wessel, 2001] and oceanic plateaus masked [Coffin and Eldholm, 1994] and 2-minute grids of sediment thickness [Divins, 2004] and half-spreading rate [Müller, et al., 2008] to create a residual roughness grid where the influence sediment thickness and spreading rate are removed.

Paper 2 uses the palaeo-age grid to reconstruct the Circum-Antarctic palaeo-basement at 5 Ma, 14 Ma, 17 Ma, and 33 Ma using the method outlined in Brown et al. [2006]. Paper 2 also uses three seismic reflection profiles collected on the RV/IB Palmer in 1997 and the analogue 1972 ELT52 seismic profile to tie the profiles to DSDP site 274. The southernmost Adare Trough profile is only presented in Paper 2, while the northern two profiles are also presented in Keller [2004] and Müller et al. [2005]. Paper 2 also uses the Steinberger et al. [2004] mantle convection model, where the change of density anomalies with time is computed by advecting the anomalies backwards in the mantle flow field, to examine the effect of mantle dynamics on seafloor sedimentation.

Paper 3 uses the palaeo-age grid and plate kinematic model to compute shallow slab dip angles at the Sundaland subduction zone, as well as absolute plate motion vectors for the Indian, Australian, Sundaland and Eurasian plates for the period from the present to 80 million years ago. Also in paper 3 the position of a slab window, formed when the Wharton Ridge subducted beneath Sundaland, was calculated from a combination of the age-grid and absolute motion vectors using the method of Thorkelson [1996].

Paper 4 uses the palaeo-agegrid and plate kinematic model to understand the relationship between the subduction of the Izanagi Ridge beneath Northern Asia and a series of plate reorganisations that subsequently occurring through the global plate tectonic system.

Paper 4 also uses new magnetic anomaly identifications made from data collected in the Bruce Rise area and along the Terre Adelie and Wilkes Land margins by Geoscience Australia and the VNII Okeangeologia, Antarctic Branch, as well as magnetic anomalies identification from Tikku and Cande [1999]. For periods where there is an absence of magnetic anomalies gravity anomaly identifications are utilised. These were made using a downward continued gravity anomaly grid based on the method of Sandwell and Smith [2005].

All figures in this thesis were produced using GMT (Generic Mapping Tools) software [Wessel and Smith, 1998].

1.4 Overview of Thesis

This thesis investigates the impacts of mid-ocean ridge evolution and destruction, in order to better understand the role that mid-ocean ridges play in shaping the Earth's plate tectonic system and the landscapes of the ocean basins and basin rims. The main body of this thesis is composed of four papers followed by a discussion of the common themes shared by these papers.

Paper 1: The Origins of Seafloor Roughness

Seafloor roughness varies considerably across the world's ocean basins and is fundamental to controlling circulation and mixing in the oceans. Seafloor spreading rates are well known to influence topographic roughness in the oceans, but high-resolution marine gravity data suggest that other factors, overlooked so far, may be more important. This paper shows that long-term variations in oceanic roughness are strongly related to mantle temperature, mantle fertility, and spreading obliquity. Smooth crust is associated with hot mantle, as well as fast spreading rates, while rough crust is associated with cool and/or depleted mantle, highly oblique spreading ($> 45^\circ$) directions, and slow spreading rates.

Paper 2: Seismic Stratigraphy of the Adare Trough area, Antarctica

The Adare Trough is the extinct third arm of a Tertiary spreading system. Actively spreading from 55-43 Ma to 28-26 Ma, the sediments

and crust of the Adare Trough reveal how mantle-driven dynamic topography, sediment supply and ocean currents combine to shape the morphology of the seafloor. The rough morphology of the Adare Trough has acted as an impediment to Antarctic bottom currents leading to uneven distributions of sediment, which demonstrates how the morphology of the seafloor interacts with oceanic processes. Small-scale volcanism in the Adare Trough is similar to small-scale alkaline volcanism observed throughout the Pacific and is likely related to broad scale patterns of mantle dynamics.

Paper 3: Sunda-Java trench kinematics, slab window formation and overriding plate deformation since the Cretaceous

The kinematics and time-dependence of back-arc extension or compression is one of the most poorly understood aspects of plate tectonics, and has nearly exclusively been studied from snapshots of present-day observations. Here absolute and relative plate motions combined with reconstructions of now subducted ocean floor to analyse subduction kinematics and upper plate strain from geological observations since 80 Ma along the 3200 km long Sunda-Java trench, one of the largest subduction systems on Earth. Combining plate motions and slab geometries enables us to reconstruct a time-dependent slab window beneath Sundaland, formed through Wharton spreading ridge subduction. This paper finds that upper plate advance and retreat is the main influence on upper plate strain, but subduction of large bathymetric ridges, and slab-window effects, also play a significant, and at times dominant, role. Compression in the Sundaland back-arc region can be linked to advance of the upper plate. Extension of the Sundaland backarc region correlates with two patterns of upper plate motion, (a) retreat of the upper plate, and (b) advance of the upper plate combined with more rapid advance of the Sundaland margin due to hinge roll-back. Subduction of large bathymetric ridges causes compression in the upper plate, especially Wharton Ridge subduction underneath Sumatra over the period 150 Ma. These reconstructions unravel the evolving geometry of a

slab window underlying the Java-South Sumatra region, and it is proposed that decreased mantle wedge viscosities associated with this slab-window exacerbated Palaeogene extension in the Java Sea region via active rifting, and enabled Sumatran continental extension to continue at 5035 Ma when upper plate advance would otherwise have led to compression.

Paper 4: Major Australian-Antarctic Plate Reorganization at Hawaiian-Emperor Bend Time

Motion of Pacific tectonic plate underwent a shift approximately 50 million years ago, as evidenced by the bend in the Hawaiian-Emperor chain of seamounts. The mechanism responsible for this sudden change in motion has previously been unclear. This paper shows that evidence for a coeval change in plate movement between Australia and Antarctica gleaned from magnetic and satellite gravity data, indicating that a major plate reorganization occurred between 50 and 53 million years ago. Revised Pacific Ocean-floor reconstructions suggest that rapid subduction of the Izanagi mid-ocean ridge and subsequent Marianas/Tonga-Kermadec subduction initiation may have been the ultimate causes of these events.

Chapter 2

The Origin of Seafloor Roughness

This paper has been prepared for submission to Nature

Seafloor roughness varies considerably across the world's ocean basins and is fundamental to controlling the circulation and mixing of heat in the ocean¹ and dissipating eddy kinetic energy². Seafloor spreading rates are known to influence the morphology of mid-ocean ridges e.g.³ with rougher basement forming below a spreading rate threshold of 30-35 mm/yr^{4,5}. A global analysis of marine gravity-derived roughness of Cretaceous to Cenozoic ridge flanks reveals that, after eliminating spreading rate and sediment thickness related effects, residual roughness anomalies of 5-20 mGal remain over large swaths of ocean floor. Elevated mantle temperatures such as those due to the Iceland hotspot result in smoother than expected seafloor basement, whereas low mantle temperature and/or reduced fertility anomalies such as those associated with the Australian-Antarctic Discordance result in increased basement roughness. High spreading obliquities ($> 45^\circ$) cause rougher than expected basement, but are relatively rare. Superswells, such as the Cretaceous Darwin Rise and the present southwest Pacific superswell⁶, are not associated with residual roughness anomalies. In contrast, Cretaceous Atlantic ocean floor, formed over mantle previously overlain by the Pangaea supercontinent, displays anomalously low roughness, independent of spreading rates. We attribute this to a sub-Pangaean mantle temperature anomaly⁷ that was gradually dissipated through sea floor spreading, leading to thicker crust⁸, reduced brittle fracturing and smoother basement relief. Anomalously rough basement formed during the Cenozoic in regions away from major hotspots in the Atlantic and western Indian oceans is interpreted to re-

flect progressively depleted upper mantle, deficient in plume-fed asthenosphere⁹.

The relationship between spreading rates and marine basement roughness has predominantly been determined through analysis of near-zero aged crust on individual profiles across mid-ocean ridges using short wavelength gravity^{3,4} or bathymetry. This relationship was also found to hold for off-axis oceanic crust at all ages⁵. Short wavelength roughness in gravity anomalies (~ 20 -160 km wavelength) reflects the roughness of oceanic basement topography⁵. Here we use a 2-minute gravity anomaly grid downward continued onto the seafloor based on Sandwell and Smith¹⁰ (Supp. Fig. 9.1) to create a root mean square (RMS) marine gravity roughness grid (Fig 2.1) using a 100 km wide Gaussian filter with seamounts and oceanic plateaus masked (Supp. Fig. 9.2).

Half-spreading rate and sediment cover (Supp. Fig. 9.1) strongly influence basement roughness. These factors are removed to examine the role of other potential factors such as spreading obliquity, and mantle temperature, and mantle fertility on basement roughness. Each kilometre of sediment¹¹ results in a $\sim 14\%$ decrease in gravity roughness (Fig. 2.2a). Global half-spreading rates¹² (a) faster than 35 mm/yr result in low gravity roughness (~ 7 mGal), (b) between 35-15 mm/yr result in increasingly rough and variable gravity roughness, and (c) slower than 15 mm/yr form high-amplitude gravity roughness (~ 15 mGal) (Fig. 2.2b). These results differ from previous findings^{4,5} that suggest gravity roughness continues to increase with decreasing spreading rates < 15 mm/yr.

Our results confirm that the relationship between spreading rate and basement roughness is consistent with the magma lens model of

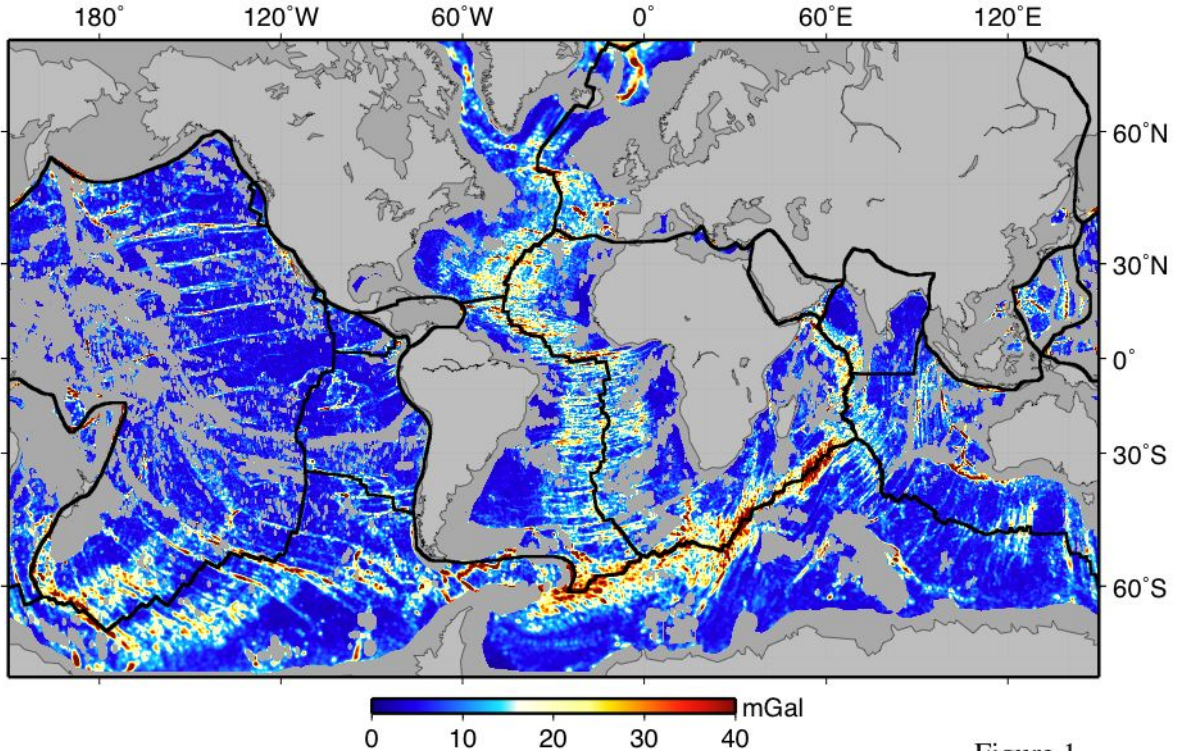


Figure 1

Figure 2.1: RMS downward-continued gravity roughness, calculated using a Gaussian filter with a half-width of 50 km, with plate boundaries shown as heavy black lines, landmasses in light grey, and masked continental shelves, seamounts and large igneous provinces in dark grey.

mid-ocean ridge formation¹³, where decreasing spreading rates lead to increasing lens depth and decreased melt production, with a relatively rapid transition from a lens to no-lens situation. Our global results show that roughness is insensitive to spreading rate at rates >35 mm/yr and <15 mm/yr, likely representing lens and no-lens situations, respectively, with a transitional stage occurring as spreading rates drop from 30-35 to 15 mm/yr. Crust created at rates <15 mm/yr is approximately twice as rough as crust created at rates >35 mm/yr, consistent with thermo-tectonic cyclicity at slow spreading rates^{14,15}.

Residual roughness (Fig. 2.3) is calculated by removing spreading rate and sediment thickness effects (Fig. 2.2) from the RMS-gravity roughness grid (Fig. 2.1) to investigate how spreading obliquity and mantle conditions influence basement roughness. Spreading obliquity is a ubiquitous phenomenon, observed at $\sim 72\%$ of spreading centres¹⁶. Higher angles of spreading obliquity are related to increasing ridge segmentation^{15,17,18} and seismicity¹⁷,

both due to increased brittle fracturing at higher spreading angles¹⁷. Spreading obliquity has also been found to influence ridge morphology by decreasing effective spreading rates proportionally to $\cos(\theta)$ ¹⁹, where θ is the angle of obliquity.

We create regional 2-minute spreading obliquity grids for ten regions (that intentionally exclude triple-junctions, small/temporary spreading centres, back-arc basins and areas with complex spreading histories: Fig. 2.3 and Supp. Fig. 9.5-9.14) by calculating the difference between the regional plate motion direction and the normal to the regional mid-ocean ridge strike in 5 million year stages. For spreading obliquities between 0° and 45° , variation of residual roughness with spreading obliquity fits an inverted cosine curve (Figure 2.3, inset). However, for obliquities $>45^\circ$ residual roughness increases much more rapidly than expected from a cosine relationship, indicating that an additional mechanism, likely brittle fracturing, causes increased roughness at high spreading obliquities.

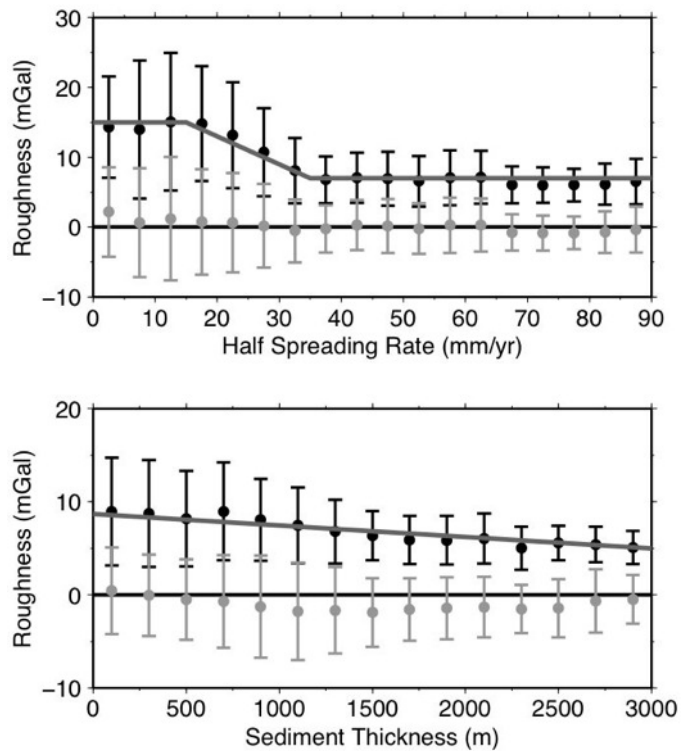


Figure 2.2: Gravity roughness as a function of (a) spreading half-rates and (b) sediment thickness obtained by calculating the median roughness and its median absolute deviation in bins sized 5 mm/yr for half-spreading rates and 200 m for sediment thickness, respectively (black dots). Dark grey lines on each graph shows line of best fit, which is used to remove the effects of spreading rate and sediment thickness from gravity roughness. Light grey dots show variation of residual gravity roughness (see Figure 2.3), with (a) spreading rate and (b) sediment thickness. Error bars show +/- median absolute deviation (MAD).

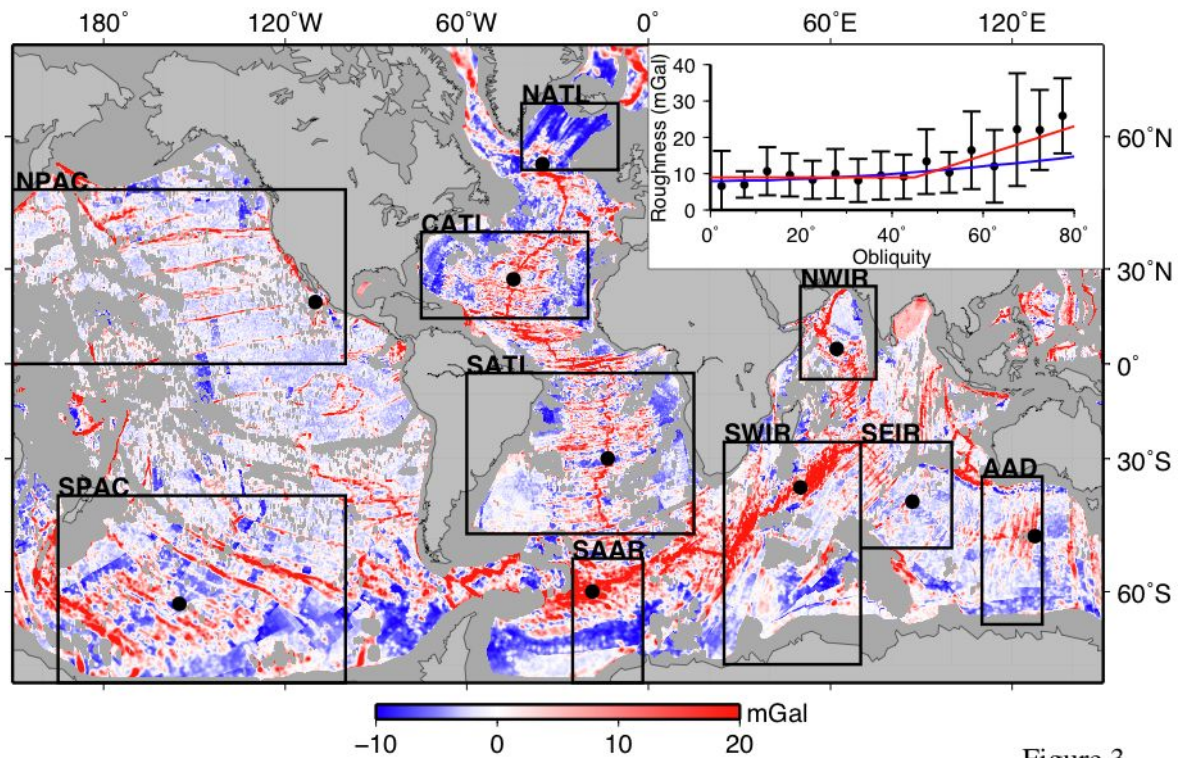


Figure 3

Figure 2.3: Residual roughness, calculated by removing the effects of spreading rate and sediment thickness from the gravity roughness grid using the relationships between spreading half-rate and sediment thickness and roughness shown by the lines of best fit in Figure 2.2. Boxes show locations of individual spreading systems used to investigate the relationship between the angle of spreading obliquity and residual roughness. Black dots show location where spreading direction through time for each region were calculated. Graph in top right corner shows the relationship between roughness and spreading obliquity. Red line shows 2-stage line of best fit. Blue line shows the fit of inverted cosine curve that describes the influence of spreading obliquity on roughness by decreasing effective spreading rates, assuming an average roughness of 8 mGal at 0° .

Analysis of residual roughness is carried out for each selected region (Figure 2.4) based on spreading rate, sediment thickness and RMS-gravity roughness. Only in the North and South Pacific is basement roughness accurately predicted using spreading rate and sediment thickness. With the additional removal of roughness related to spreading obliquity, the roughness of the Southeast Indian Ridge flanks is well predicted, while the misfit for the South American-Antarctic Ridge is reduced. However, spreading rate, sediment thickness and spreading obliquity do not accurately predict basement roughness for the remaining regions that exhibit long-term deviations of 5-20 mGal over periods >40 Myr and in many cases >60 Myr (Fig. 2.4).

We suggest that remaining long-term residual roughness variations, after the removal of roughness caused by spreading rate and sediment cover variations, are largely attributable to the temperature and fertility conditions of the underlying mantle. Spreading rates influence marine basement roughness by affecting the bulk extent of melting beneath mid-ocean ridges. However, melt volumes are also related to crustal thickness, a parameter strongly controlled by mantle temperature²⁰⁻²². Mantle fertility additionally affects the bulk extent of melting^{20,23}, with depleted mantle producing lower melt volumes²⁴ and thus rougher basement. The best location to study the influence of anomalously hot mantle on basement roughness is the Norwegian-Greenland Sea, where the Reykjanes Ridge interacts with the Icelandic hotspot. Basement here should be relatively rough due to slow spreading rates (<20 mm/yr) however, the area is characterised by high heat flow, anomalously thick crust, sparse fracture zones²⁵ and basement that is 3-10 mGal smoother than predicted based on spreading rates and sediment thickness effects. Here it is likely that anomalously high mantle temperatures have maintained excess partial melts, and reduced brittle fracturing in spite of slow spreading rates.

Cretaceous (80-130 Myr) oceanic crust is smoother than expected, expressed by negative residual roughness (-3 to -9 mGal), in the South American-Antarctic Ridge, and Central and South Atlantic regions. These regions all

formed at slow spreading rates (<30 mm/yr) during the initial stages of continental dispersal. Continental aggregation may cause an enlargement of mantle convection wavelengths leading to mantle temperatures up to 100°C hotter than normal beneath supercontinents⁷. This mantle thermal anomaly is dissipated through sea floor spreading following supercontinent break-up. The anomalously hot mantle would lead to thicker crust and reduced brittle fracturing even under slow spreading conditions. Ocean drilling results contain evidence that the Cretaceous mantle may have been ~50°C hotter and oceanic crust 1-2 km thicker than at present⁸. However, it is unlikely that the entire Cretaceous mantle was hotter than at present. Rather, the majority of preserved Cretaceous oceanic crust may have accreted from anomalously hot mantle following Pangaea break-up, resulting in anomalously low basement roughness. Globally, basement roughness of 0-80 Myr old crust increases with slowing spreading rates below 30-35 mm/yr, however spreading rate appears to have no affect on the basement roughness of crust aged 80-130 Myr (Supp. Fig. 9.3). There is no variation of roughness with crustal age if crust formed at all spreading rates is analysed together (Supp. Fig. 9.3). We suggest that most crust aged between 80 and 130 Myr exhibits relatively smooth basement irrespective of spreading rates due to underlying hot supercontinent-derived mantle.

The North Pacific is the only region with substantial volumes of preserved 80-130 Myr old crust that did not form through supercontinent break-up. Here spreading rate and sediment thickness accurately predict basement roughness despite the influence of the Cretaceous North Pacific superswell, which may be expected to lead to anomalously smooth basement due to increased heat flow and partial melting⁶. Presently the South Pacific is underlain by a similar superswell⁶, which also does not lead to smoother (or rougher) than expected basement. Our observations suggest that superswells, while causing widespread, small-scale volcanism and shallowing of the seafloor⁶ do not strongly influence accretionary processes at mid-ocean ridges.

Relatively smooth basement is predicted for

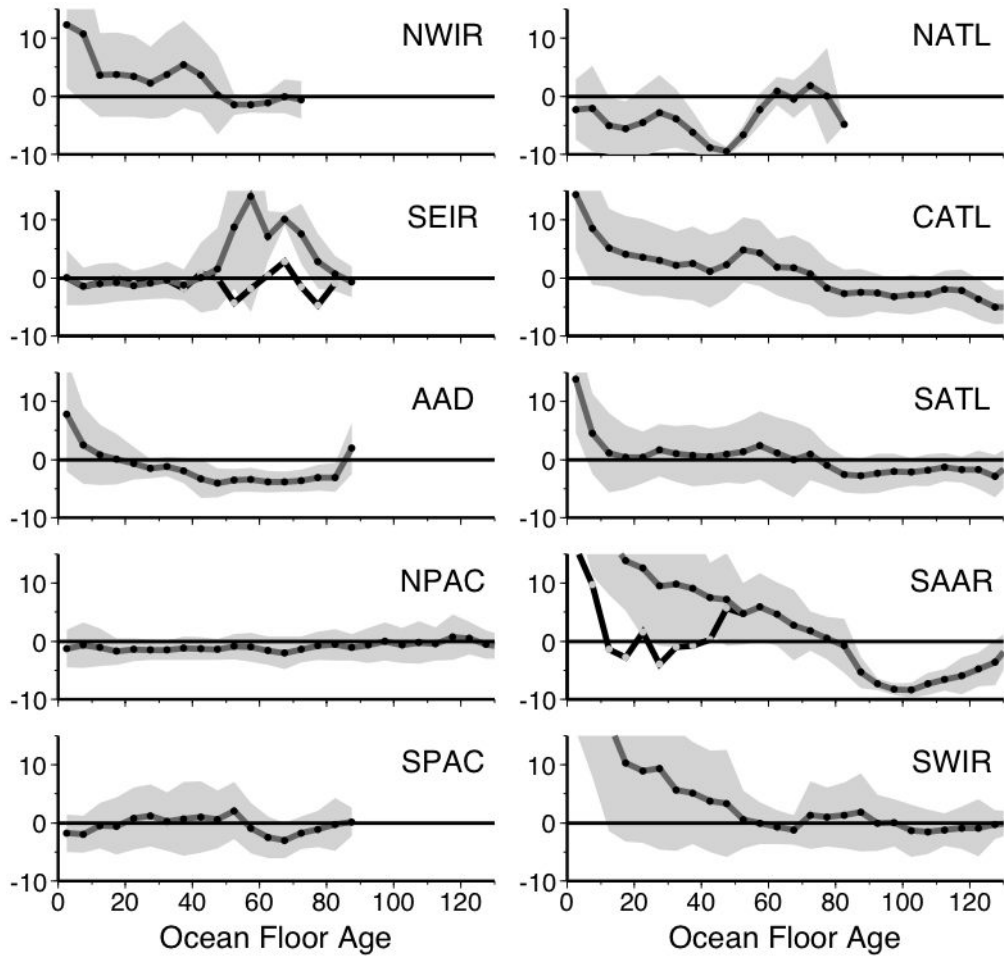


Figure 2.4: Variation of residual roughness in 5 million year stages (grey line with black dots) for regions (a) NWIR, (b) NATL, (c) SEIR, (d) CATL, (e) AAD, (f) SATL, (g) NPAC, (h) SAAR, (i) SPAC, and (j) SWIR. Grey envelope shows the \pm median absolute deviation (MAD). Black line with grey dots shows residual roughness with roughness attributable to spreading obliquity removed using the relationship shown by the red line in Fig. 2.3(inset).

the Australian-Antarctic Discordance (AAD) based on spreading rates of 35-40 mm/yr since ~ 40 Myr ago. However, the AAD exhibits basement up to 8 mGal rougher than predicted (Fig. 2.4e). Crustal thickness in the AAD is 2-4 km thinner than adjacent crust, implying a 150°C decrease in mantle temperature²⁶. Also, the AAD is located at the site of a palaeo-subduction zone, with current lavas likely sourced from depleted magmas derived from subducted oceanic crust²⁷. Both cool mantle temperatures and low mantle fertility result in reduced mid-ocean ridge melt volumes²⁴ and have resulted in rough basement in the AAD despite relatively fast spreading rates over the past 15 Myr²⁸.

Many of the spreading systems analyzed here experienced a shift from smoother to rougher than expected basement at ~ 70 Myr ago (central and southern Atlantic systems) and $\sim 50^\circ$ Myr ago (western Indian systems). This may partly reflect the gradual dissipation of a supercontinent related thermal anomaly, but this alone would not account for a shift to a positive roughness anomaly. Upper mantle depletion is known to reduce melt volumes²⁴. The western Indian and central and southern Atlantic mid-ocean ridges are relatively distal to large mantle plumes, resulting in poor upper mantle replenishment because of their dependence on slow, localised mantle upwellings⁹. An unusual geochemical signature indicates that depleted rather than cold mantle is at least partly responsible for anomalously rough basement at the Southwest Indian Ridge²⁴. There are also isotopic differences between the Indian and Atlantic oceans⁹, which may explain why the central and southern Atlantic exhibit a different pattern of increased basement roughness compared to the western Indian ocean region.

Contrary to previous studies our results demonstrate that mantle temperature/fertility and spreading obliquity can dominate spreading rate effects on oceanic basement roughness. As ocean mixing is strongly influenced by seafloor topography, realistic palaeoceanographic simulations depend on reconstructed ocean basin topography, including palaeo-gateways underlain by now subducted crust. Our model provides a predictive framework for reconstructing more realistic maps of ancient

ocean basins a necessary prerequisite for understanding ocean circulation and mixing through time.

Methods Summary

We high-pass the downward-continued gravity grid using a Gaussian filter of 100km width, then calculate a Gaussian-weighted RMS for these residuals with the same filter width (Fig. 2.1). Short wavelength roughness in gravity anomalies (~ 20 -160 km wavelength) reflects the roughness of oceanic basement topography⁵. By computing a roughness grid based on a filter width of 160 km following Smith⁵ we find that many basement tectonic features are not well resolved (Supp. Fig. 9.4). This reflects that the vast majority of structural features of the seafloor such as abyssal hills, fracture zone troughs and ridges have wavelengths significantly smaller than 160km. We select a 100km filter width in order to better resolve spatial variations in seafloor roughness on relatively small scales (Supp. Fig. 9.4). The spreading rate dependence of roughness is analysed here in 5 Ma intervals. However, at a half-spreading rate of 10 mm/yr only 50 km of oceanic basement is produced over 5 million years. Use of a narrower (100 km) filter reduces binning of crust formed over periods longer than 5 million years. Intraplate seamount trails and large igneous provinces, rough features formed by non-accretionary processes, are masked from the basement roughness grid using a mask based on Wessel's²⁹ seamount catalogue and Coffin and Eldholm's³⁰ outlines of oceanic plateaus. The mapped seamount radii are multiplied by a factor of 2.5 to mask out flexural effects from seamount emplacement. Without this masking the roughness becomes biased by intraplate volcanism unrelated to mid-ocean ridge processes (Supp. Fig. 9.2).

References

- ¹ Polzin, K. L., Toole, J. M., Ledwell, J. R., and Schmitt, R. W., Spatial variability of turbulent mixing in the abyssal ocean. *Science* **276** (5309), 93 (1997).
- ² Gille, S. T., Yale, M. M., and Sandwell,

- D. T., Global correlation of mesoscale ocean variability with seafloor roughness from satellite altimetry. *Geophys. Res. Lett.* **27** (9), 1251 (2000).
- ³ Malinverno, A., Inverse square-root dependence of mid-ocean-ridge flank roughness on spreading rate. *Nature* **352**, 58 (1991).
- ⁴ Small, C. and Sandwell, D. T., An abrupt change in ridge-axis gravity with spreading rate. *Journal of Geophysical Research* **94**, 17383 (1989).
- ⁵ Smith, W. H. F., Seafloor tectonic fabric from satellite altimetry. *Ann. Rev. Earth Planet. Sci.* **26**, 697 (1998).
- ⁶ McNutt, M.K., Superswells. *Rev. Geophys.* **36** (2), 211 (1998).
- ⁷ Coltice, N., Phillips, B.R., Bertrand, H., Ricard, Y., and Rey, P., Global warming of the mantle at the origin of flood basalts over supercontinents. *Geology* **35**, 391 (2007).
- ⁸ Humler, E., Langmuir, C., and Daux, V., Depth versus age: new perspectives from the chemical compositions of ancient crust. *Earth Planet. Sci. Lett.* **173**, 7 (1999).
- ⁹ Meyzen, C.M. et al., Isotopic portrayal of the Earth's upper mantle flow field. *Nature* **447** (1069-1074) (2007).
- ¹⁰ Sandwell, D. T. and Smith, W. H. F., Retracking ERS-1 altimeter waveforms for optimal gravity field recovery. *Geophys. J. Int.* **163** (1), 79 (2005).
- ¹¹ Divins, D.L, (National Geophysical Data Center, 2004).
- ¹² Müller, R.D., Sdrolias, M., Gaina, C., and Roest, W.R., Age, spreading rates and spreading asymmetry of the world's ocean crust. *Geochem. Geophys. Geosyst.* (in review).
- ¹³ Chen, Y. J. and Phipps-Morgan, J., The effects of spreading rate, the magma budget, and the geometry of magma emplacement on the axial heat flux at mid-ocean ridges. *J. Geophys. Res.* **101** (5), 11475 (1996).
- ¹⁴ Mendel, V. et al., Magmato-tectonic cyclicity at the ultra-slow spreading Southwest Indian Ridge: Evidence from variations of axial volcanic ridge morphology and abyssal hills pattern. *Geochem. Geophys. Geosys.* **4**, 9102 (2003).
- ¹⁵ Abelson, M. and Agnon, A., Mechanics of oblique spreading and ridge segmentation. *Earth Planet. Sci. Lett.* **148** (3-4), 405 (1997).
- ¹⁶ Woodcock, N.H., The role of strike-slip fault systems at plate boundaries. *Philos. Trans. R. Soc. London, Ser. A* **317**, 13 (1986).
- ¹⁷ de Alteriis, G., Gilg-Capar, L., and Olivet, J. L., Matching satellite-derived gravity signatures and seismicity patterns along mid-ocean ridges. *Terra Nova* **10** (4), 177 (1998).
- ¹⁸ Mosher, S. and Massell Symons, C., Ridge reorientation mechanisms: Macquarie Ridge Complex, Australia-Pacific plate boundary. *Geology* **36** (2), 119 (2008).
- ¹⁹ Montesi, L.G.J. and Behn, M.D., Mantle flow and melting underneath oblique and ultra-slow mid-ocean ridges. *Geophys. Res. Lett.* **34** (2007).
- ²⁰ Klein, E.M. and Langmuir, C.H., Global correlations of ocean ridge basalt chemistry with axial depth and crustal thickness. *J. Geophys. Res.* **92**, 8089 (1987).
- ²¹ McKenzie, D. and Bickle, M.J., The volume and composition of melt generated by extension of the lithosphere. *J. Petrol.* **29** (3), 625 (1988).
- ²² Asimow, P.D. and Langmuir, C.H., The importance of water to oceanic mantle melting regimes *Nature* **421**, 815 (2003).
- ²³ Langmuir, C.H., Klein, E.M., and Plank, T., in *Mantle Flow and Melt Generation at Mid-Ocean Ridges*, *AGU Geophysical Monograph*, edited by Phipps Morgan, J., Blackman, D.K., and Sinton, J.M. (1992), Vol. 71, pp. 183.
- ²⁴ Meyzen, C.M., Toplis, M.J., Humler, E., Ludden, J.N., and Mevel, C., A discontinuity in mantle composition beneath the southwest Indian ridge. *Nature* **42**, 731 (2003).
- ²⁵ Bown, J. W. and White, R. S., Variation with spreading rate of oceanic crustal thickness and geochemistry. *Earth Planet. Sci. Lett.* **121** (3-4), 435 (1994).
- ²⁶ West, B.P., Sempere, J.C., Pyle, D.G., Phipps Morgan, J., and Christie, D.M., Evidence for variable upper mantle temperature and crustal thickness in and near the Australian-Antarctic Discordance. *Earth Planet. Sci. Lett.* **128** (3-4), 135 (1994).
- ²⁷ Ritzwoller, M. H., Shapiro, N. M., and Leahy, G. M., A resolved mantle anomaly as the cause of the Australian-Antarctic Discordance. *J. Geophys. Res.* **108** (B12), 2559 (2003).

²⁸ Marks, K.M., Stock, J.M., and Quinn, K.J., Evolution of the Australian-Antarctic discordance since Miocene time. *J. Geophys. Res.* **104**, 4697 (1999).

²⁹ Wessel, P., Global distribution of seamounts inferred from gridded Geosat/ERS-1 altimetry. *J. Geophys. Res.* **106**, 19431 (2001).

³⁰ Coffin, Millard F. and Eldholm, Olav, Large Igneous Provinces: Crustal Structure, Dimensions, and External Consequences. *Rev. Geophys.* **32** (1), 1 (1994).

Chapter 3

Sesimic Stratigraphy of the Adare Trough area, Antarctica

Seismic stratigraphy of the Adare Trough area, Antarctica

Joanne M. Whittaker*, R. Dietmar Müller

School of Geosciences, University of Sydney, Australia

Received 8 July 2005; received in revised form 12 May 2006; accepted 17 May 2006

Abstract

The Adare Trough, located 100 km NE of Cape Adare, Antarctica, is the extinct third arm of a Tertiary spreading ridge that separated East from West Antarctica. We use seismic reflection data, tied to DSDP Site 274, to link our seismic stratigraphic interpretation to changes in ocean-bottom currents, Ross Sea ice cover, and regional tectonics through time. Two extended unconformities are observed in the seismic profiles. We suggest that the earliest hiatus (early Oligocene to Mid-Miocene) is related to low sediment supply from the adjacent Ross Shelf, comprised of small, isolated basins. The later hiatus (mid-Miocene to late Miocene) is likely caused by strong bottom currents sourced from the open-marine Ross Sea due to increased Antarctic glaciation induced by mid-Miocene cooling (from Mi-3). Further global cooling during the Pliocene, causing changes in global ocean circulation patterns, correlates with Adare Basin sediments and indicate the continuing but weakened influence of bottom currents. The contourite/turbidite pattern present in the Adare Trough seismic data is consistent with the 3-phase contourite growth system proposed for the Weddell Sea and Antarctic Peninsula. Multibeam bathymetry and seismic reflection profiles show ubiquitous volcanic cones and intrusions throughout the Adare Basin that we interpret to have formed from the Oligocene to the present. Seismic reflection profiles reveal trans-tensional/strike-slip faults that indicate oblique extension dominated Adare Trough tectonics at 32–15 Ma. Observed volcanism patterns and anomalously shallow basement depth in the Adare Trough area are most likely caused by mantle upwelling, an explanation supported by mantle density reconstructions, which show anomalously hot mantle beneath the Adare Trough area forming in the Late Tertiary.

© 2006 Elsevier B.V. All rights reserved.

Keywords: sedimentary; Antarctica; seismic; paleoceanography

1. Introduction

The Adare Trough is located on the Antarctic lower continental slope adjacent to the Western Ross Sea (Fig. 1). Sediments are deposited offshore Antarctica through a variety of depositional processes including pelagic settling, down-slope gravity-flows, and across-slope current flows.

Weddell Sea and Antarctic Peninsula contourite deposits exhibit a three-stage growth pattern (Rebesco et al., 1997; Michels et al., 2001) with high levels of down-slope sediment supply and strong bottom currents required for contourite formation (Rebesco et al., 1997).

Here we examine the sequence stratigraphy from multi-channel seismic data to explore the influence of changing climate and bottom currents on deposition of sediment in the form of contourites and/or turbidites in the Adare Basin. We also compare the sediment deposition patterns observed at the Adare Basin with patterns observed on other sections

* Corresponding author.

E-mail address: jo@geosci.usyd.edu.au (J.M. Whittaker).

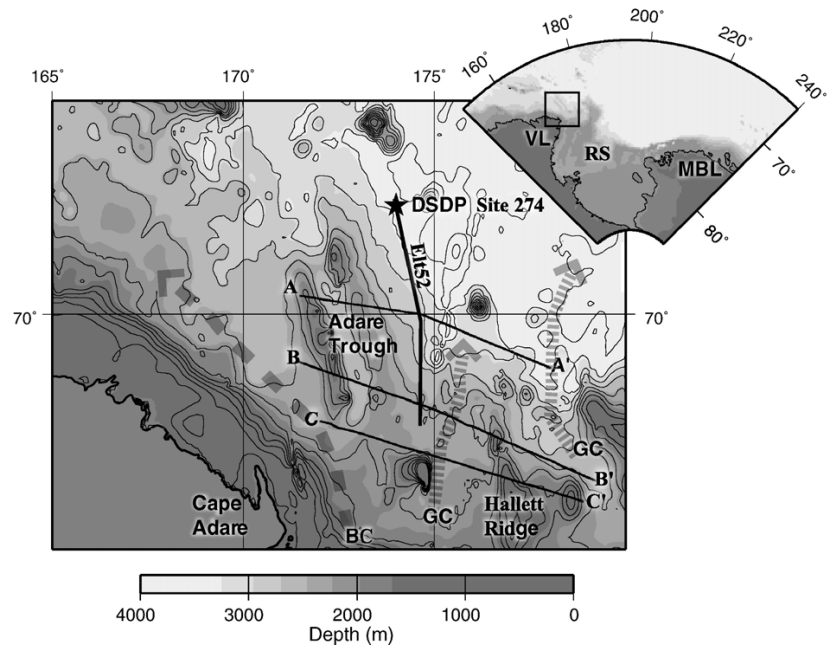


Fig. 1. (Inset) Bathymetry and topography of the Ross Dependency using ETOPO2 (U.S. Department of Commerce, 2001) with study area marked by black box; (main image) Bathymetry and topography of the Adare Basin using ETOPO2 (U.S. Department of Commerce, 2001), with the location of; the Adare Trough, the Adare Trough seismic lines, DSDP Site 274 (star), the Eltanin line used to correlate sedimentary units to seismic units, flow pattern of AABW (long dashed line marked BC for bottom current) from Orsi et al. (1999), and the position of two submarine channels (short dashed lines marked TC for turbidite channel) from Hayes and Davey (1975).

of the Antarctic margin, and assess the structural and igneous history of the area.

2. Regional setting

Antarctica consists of two large-scale tectonic domains separated by the West Antarctic Rift System. East Antarctica is a stable, Precambrian and Palaeozoic craton, while West Antarctica is an orogenic belt comprised of several younger units amalgamated prior to 100 Ma (Dalziel and Elliot, 1982; LeMasurier, 1990). Two main extensional events have affected the West Antarctic Rift

System, across which up to 300 km of displacement may have occurred since 100 Ma (Cooper et al., 1987b; DiVenere et al., 1994). The first, associated with the break up of Gondwana, occurred during the Jurassic or Cretaceous. The second event is associated with rifting between East and West Antarctica and occurred from the Eocene to the late Oligocene (Cande et al., 2000). One or more of these extensional phases was/were responsible for the formation of basins in the Ross Sea, such as the Victoria Land Basin, the Northern Basin, the Central Trough and the Eastern Basin, which trend N–S across the continental shelf (Cooper and Davey, 1985; Cooper et al.,

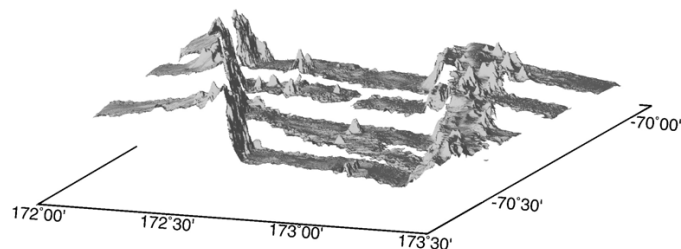


Fig. 2. Bathymetry of the Adare Trough from multi-beam ship track data, showing numerous volcanic cones throughout the Adare Trough with concentration of intrusions at the Adare Trough bounding ridges.

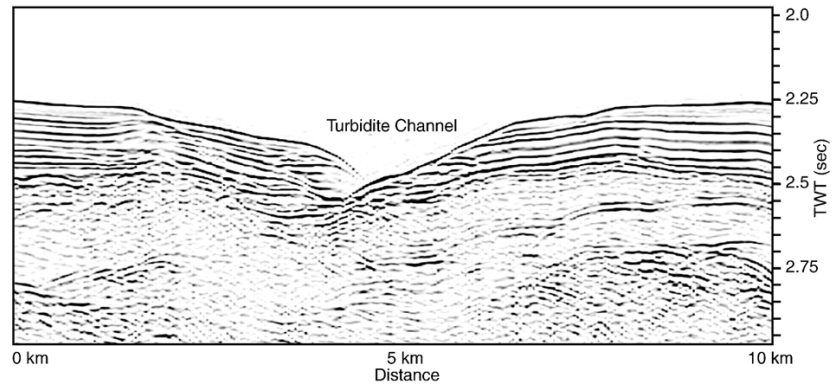


Fig. 3. Selected portion of seismic profile B–B' showing an interpreted turbidite channel, incising through the sediments from the seafloor.

1987b, 1991). Data from fracture and dyke orientations in South Victoria Land suggest a NE–SW trend for Jurassic extension and a NW–SE trend for the Cenozoic extension

(Wilson, 1992, 1995). Cenozoic extension was concentrated along the western margin of the Ross Sea at the Terror Rift (Cooper et al., 1987b) and the Adare Trough

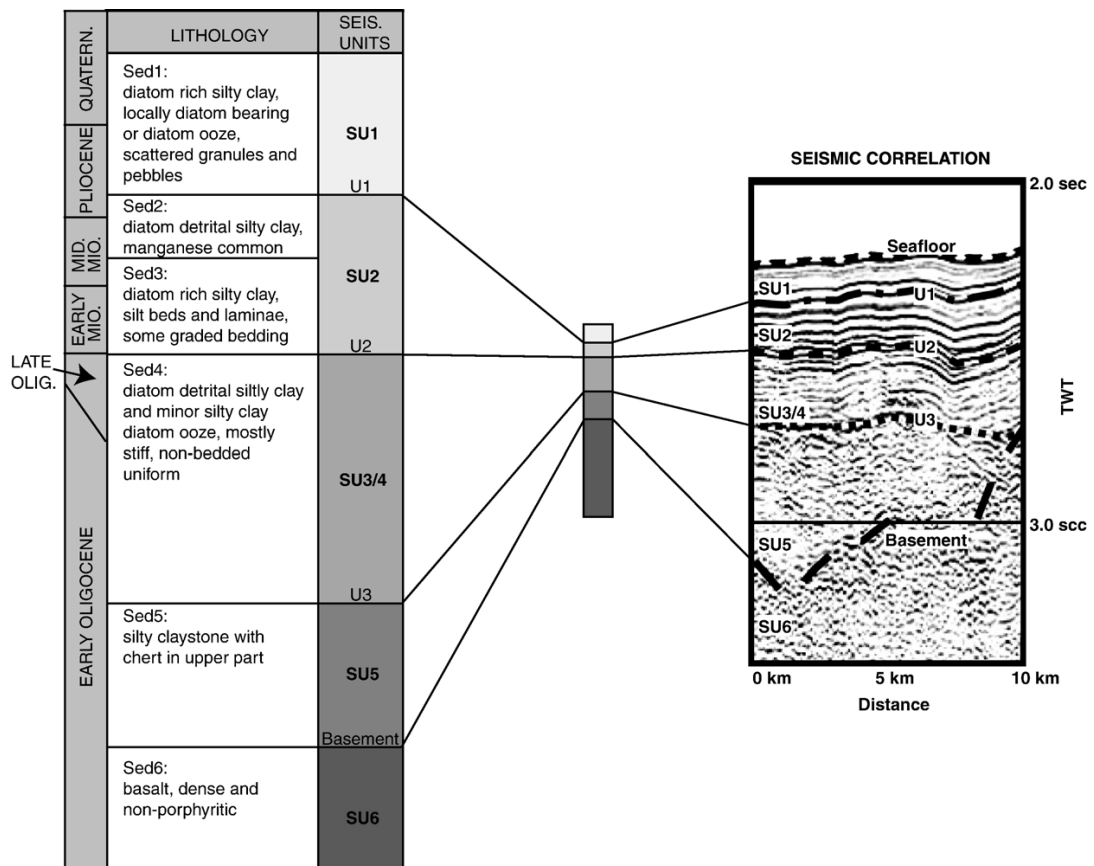


Fig. 4. Correlation between six identified sedimentary units and interpreted seismic units on profile C–C' (after Keller, 2004).

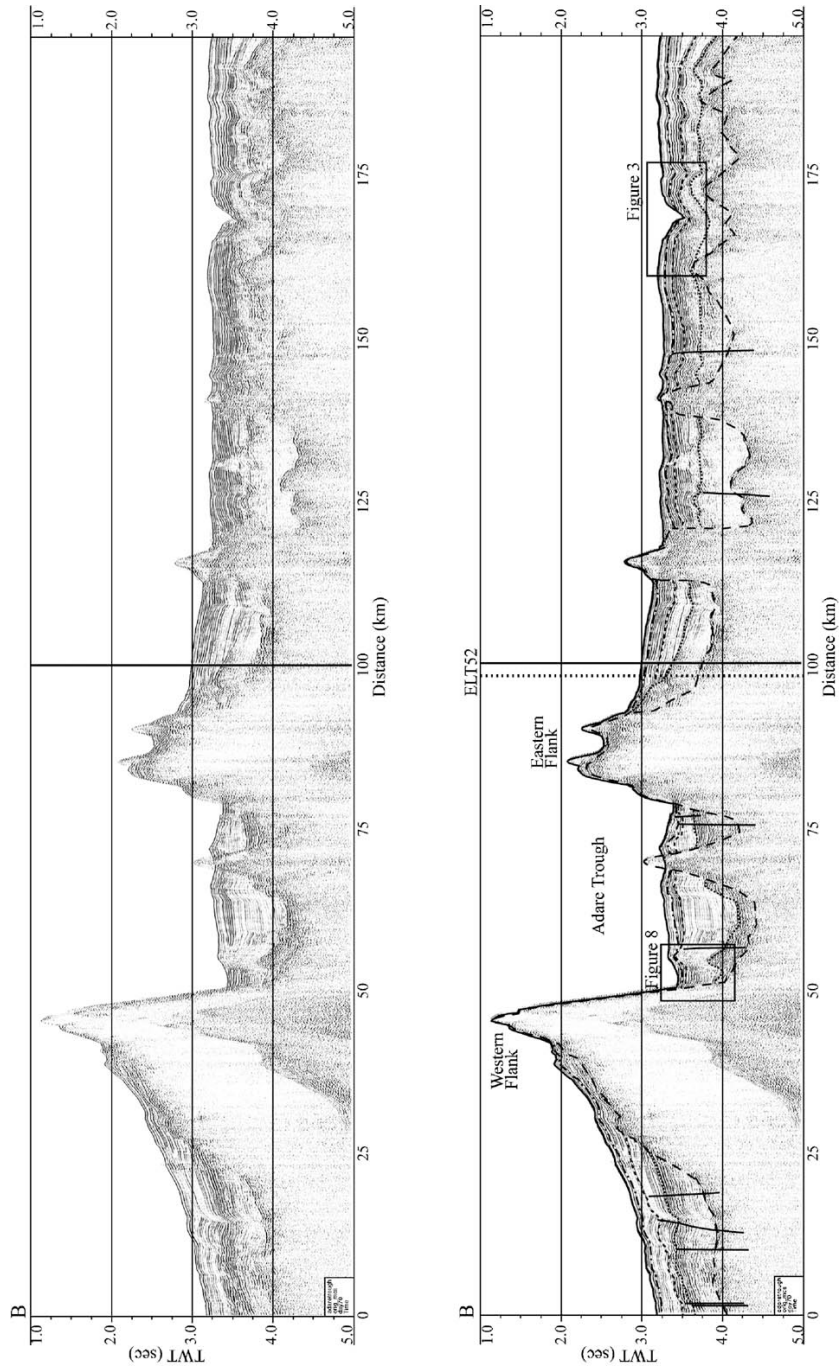


Fig. 5. NBP9702 uninterpreted (top) and interpreted (bottom) migrated 48-channel seismic profile B-B' (see Fig. 1 for location). Interpreted horizons: Solid line—scafloor, Alternating large and small dashes—unconformity 1, Medium dashes—unconformity 2, Large dashes—unconformity 3, Small dashes—unconformity 3, Large dashes—basement (also see Fig. 4). The point of intersection with profile Eltamn 52 is shown by the vertical dashed line marked ELT52.

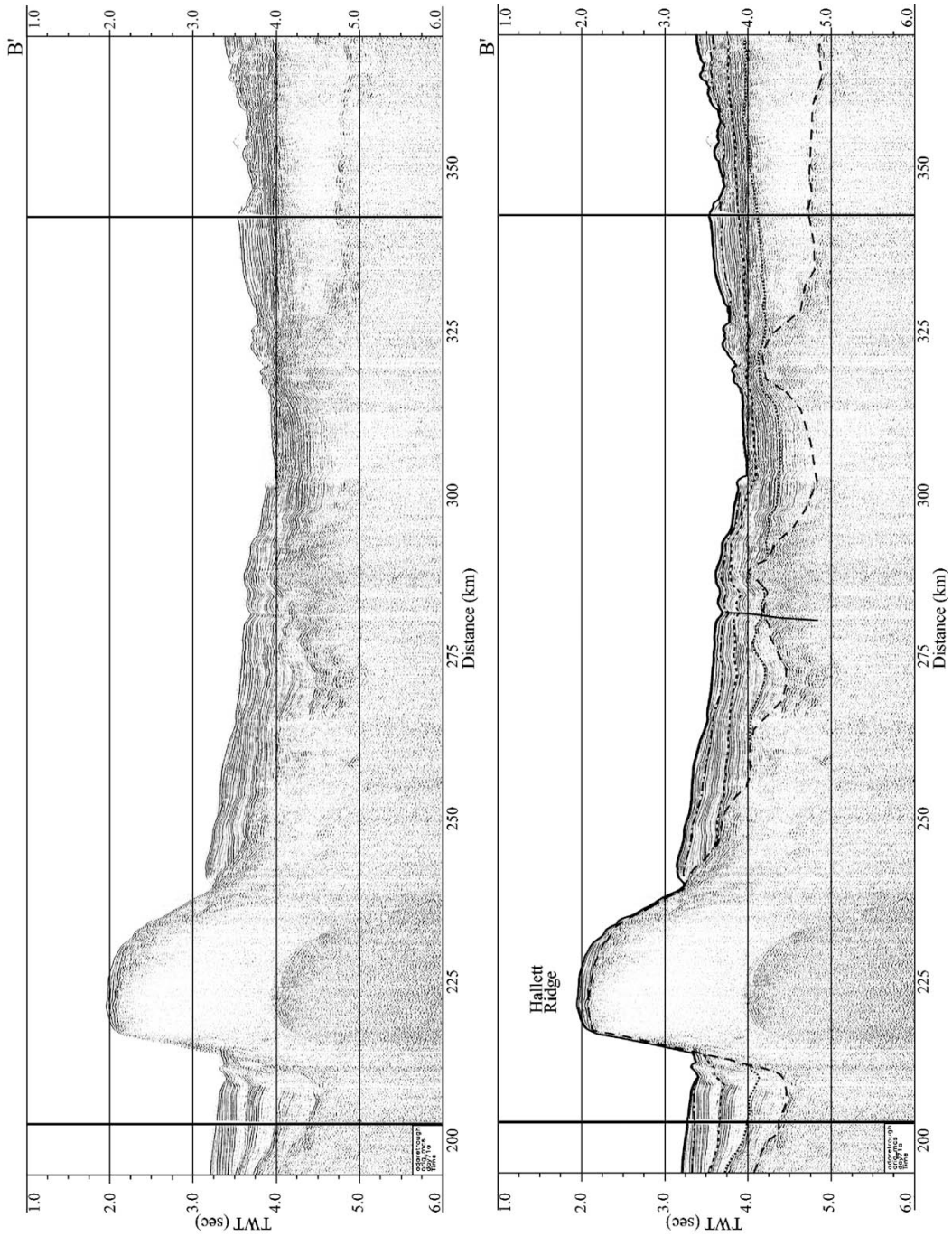


Fig. 5 (continued).

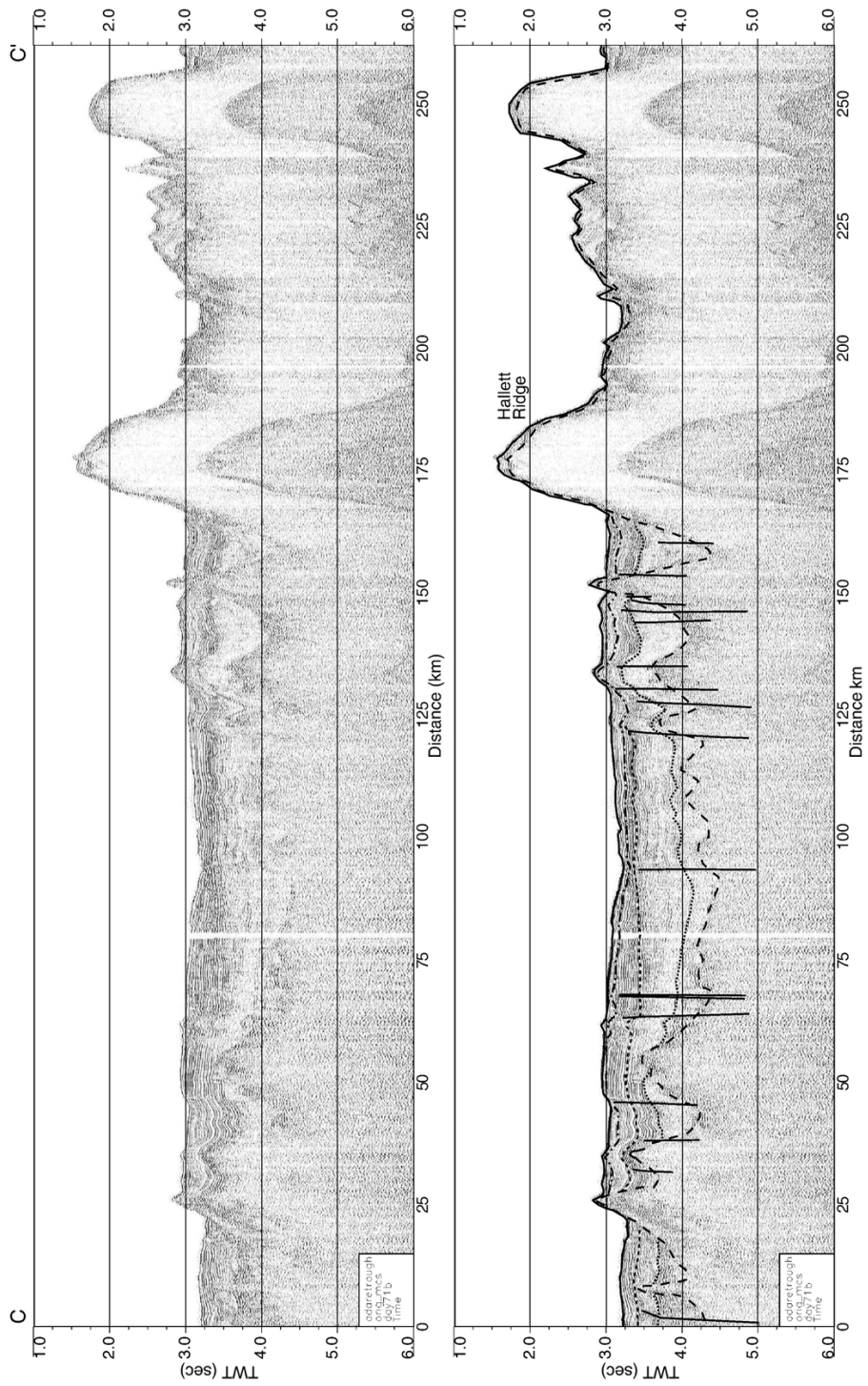


Fig. 6. NBP9702 uninterpreted (top) and interpreted (bottom) migrated 48-channel seismic profile C–C' (see Fig. 1 for location). Interpreted horizons: Solid line—seafloor, Alternating large and small dashes—unconformity 1, Medium dashes—unconformity 2, Small dashes—unconformity 3, Large dashes—basement (also see Fig. 4).

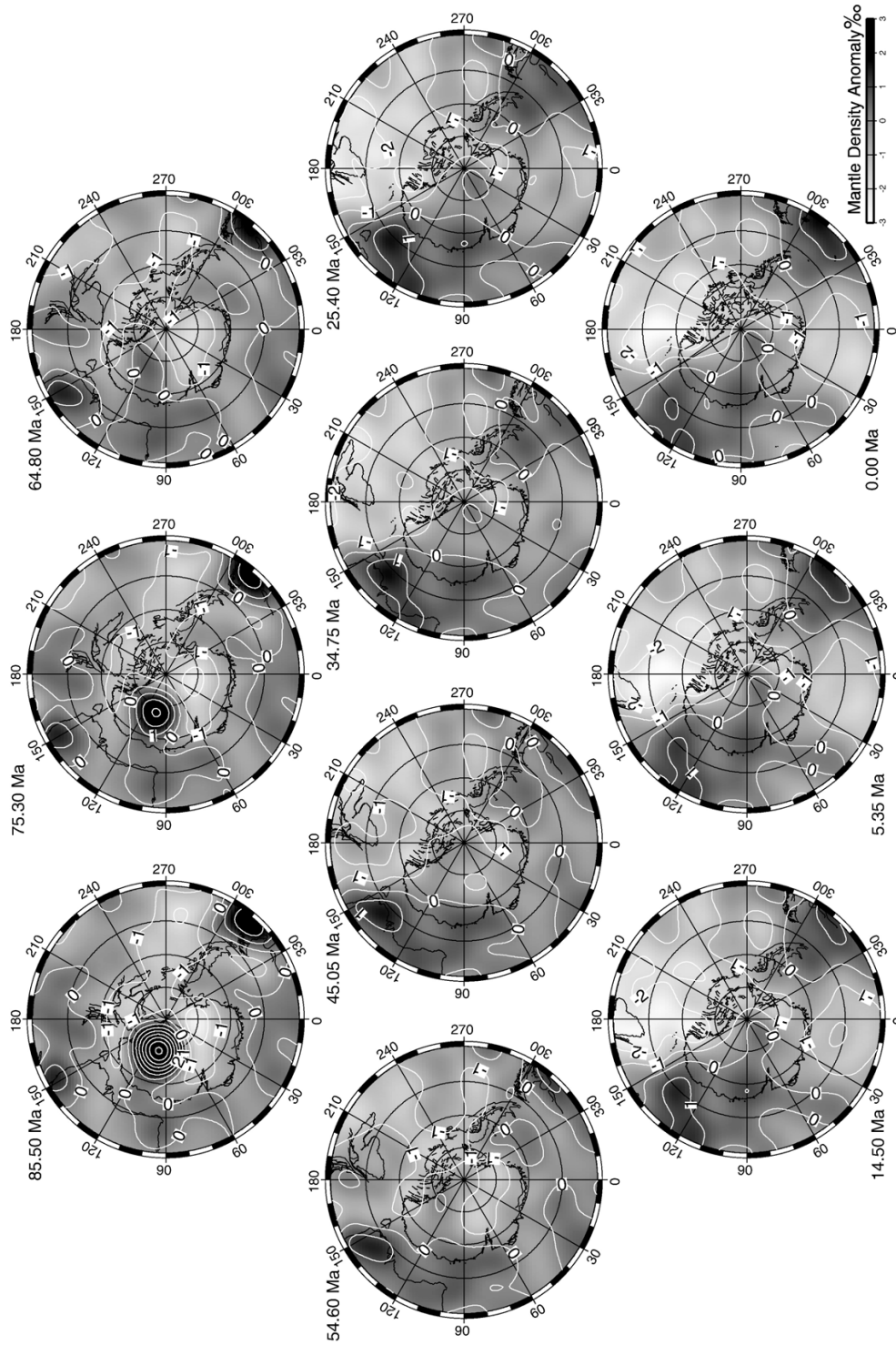
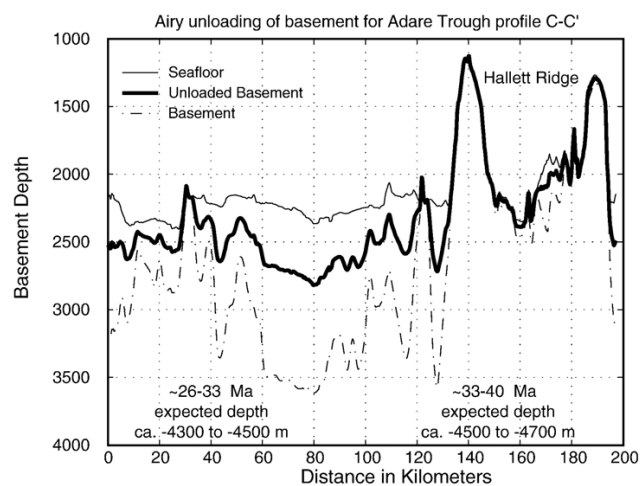
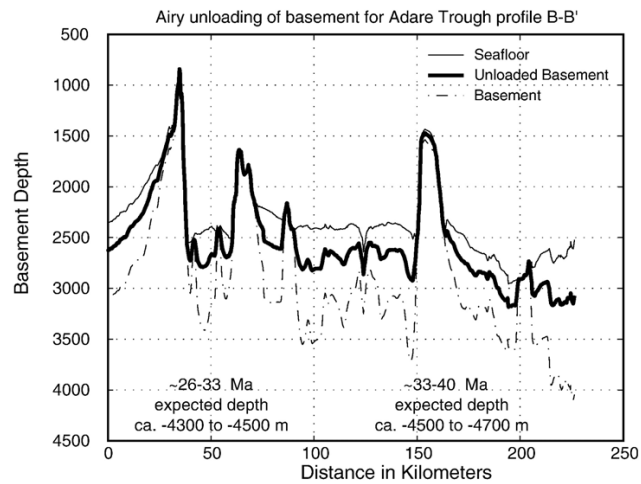
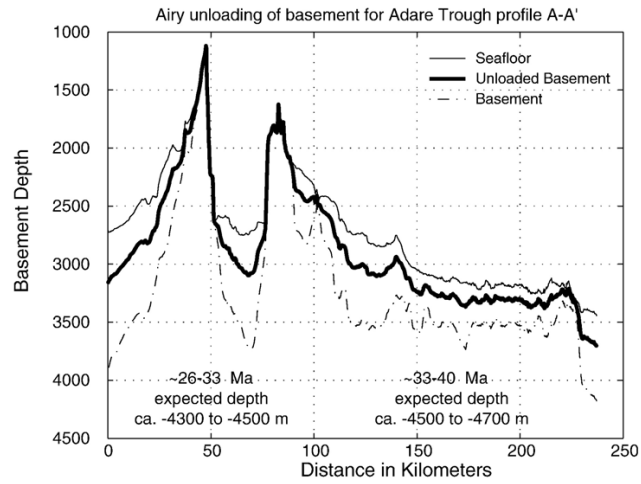


Fig. 7. Reconstructed mantle density anomalies at 500 km depth at 85.50 Ma, 75.30 Ma, 64.80 Ma, 54.60 Ma, 45.05 Ma, 34.75 Ma, 25.40 Ma, 14.50 Ma, 5.35 Ma, and 0.00 Ma, with reconstructed plate locations. Mantle density reconstructions based on the mantle convection model of Steinberger et al. (2004). Note the increase in the mantle density anomaly beneath the Adare Basin region from 54.60 Ma to 0.00 Ma.



(Cande et al., 2000). Most sedimentation in the Ross Sea basins has occurred since the second period of extension (Cooper et al., 1987a; Cape Roberts Science Team, 1998, 1999, 2000).

The NW–SE trending Adare Trough, located within the Adare Basin, is situated roughly 100 km NE of Cape Adare, Antarctica (Fig. 1). The Adare Trough is characterized by a 40 km wide, single, central graben, with high rift flanks (Hayes and Frakes, 1975). The graben has a simple bounding fault to the west (relief 1.5 km), and a more complex fault-stepping bounding pattern to the east (relief 1 km) (Müller et al., 2005). There is scattered volcanism in the eastern half of the Adare Basin and also on the eastern flank of the trough (see Fig. 2).

Magnetic anomalies curve southwards from the Adare Trough towards the Ross Sea, suggesting the Adare Trough is the extinct third arm of an E–W spreading ridge (Cande et al., 2000; Keller, 2004). Cande et al. (2000) found that the Adare Trough was active from 55–43 Ma to 28–26 Ma based on magnetic data. If Adare Trough rifting initiated at 55 Ma it coincided with rapid denudation, and inferred uplift, of Trans-Antarctic Mountains (TAM) (Fitzgerald, 1992; Fitzgerald and Gleadow, 1988) (Fitzgerald, 1994). Extensive alkaline volcanic and igneous activity has occurred in the Western Ross Embayment since approximately 50 Ma (Armienti and Baroni, 1999; Kyle, 1990; LeMasurier, 1990; Tonarini et al., 1997). Greater than average heat flow in the Ross Embayment suggests anomalously hot mantle in this area (Blackman et al., 1987). Seismic tomography reveals slow seismic velocities beneath the Ross Embayment, which also indicates the presence of hot upper mantle material (Danesi and Morelli, 2000, 2001; Ritzwoller et al., 2001).

Contourites are generally accepted to form along bathymetric contours (Heezen et al., 1966), but recent studies around Antarctica have revealed contourites elongated across bathymetric contours (Kuvaas et al., 2005; Michels et al., 2001; Rebesco et al., 1997, 1996, 2002). This orientation, perpendicular to the coastline, is most likely due to a combination of down-slope and across-slope depositional processes (Faugeres et al., 1999). To form, contourites require an adequate sediment supply and bottom currents to deposit and/or rework the sediment. Most sediment is transported to the Antarctic continental edge by glaciers grounding at the continental margin during glacial maximums. Slumping, and down-slope gravity currents then transport sediment to the lower continental slope and abyssal plain. Suspension-settling of ice-rafted

and pelagic/hemipelagic sediment also occurs. These processes have been observed in the Weddell Sea, where expanded ice-sheets transport large amounts of sediment to the shelf edge during glacial maxima enabling turbidity currents to transport sediment onto the continental slope and abyssal plain (Rebesco and Stow, 2001). The continental slope in the Adare Basin region is steep and sinuous (Pistolato et al., 2006) and turbidite channels are a common feature (Hayes and Davey, 1975) (see Figs. 1 and 3).

A number of processes influence bottom current strength on the Ross Sea continental slope. The cyclonic Antarctic Circumpolar Current (ACC) operates in the mid Southern Ocean and carries the Circumpolar Deep Water (CDW), which extends down to 4000 m (Budillon et al., 2000). Offshore the Ross Sea the CDW flows into the sluggish, cyclonic Ross Gyre and reaches the Ross Sea continental shelf (Budillon et al., 2000). Within the Western Ross Sea, High Salinity Shelf Waters (HSSW) form through the action of ice-formation and katabatic winds (Jacobs et al., 1985). Some of the HSSW flows towards the Western Ross Sea shelf break (Budillon et al., 1999) and mixes with CDW to form Antarctic Bottom Waters (AABW). This cold, dense water flows from the shelf break down the continental slope (Foldvik et al., 1985; Orsi et al., 1999; Rubino et al., 2003) and then participates in the cyclonic Ross Sea gyre (Orsi et al., 1999), see Fig. 1 for main pathway of the AABW from the Ross Sea shelf. During the Late Quaternary, AABW flowing from the Ross Sea has been generally sluggish during glacial, depositing clayey material, and strong during interglacials, depositing silty material (Brambati et al., 2002). Another bottom water source is at the Antarctic Slope Front (ASF) where dense water sinks due to low vertical stabilities of the water column (Jacobs, 1991; Whitworth, 1998). Vertical stabilities are influenced by pressure and temperature (Killworth, 1979; McPhee, 2003) and the Ross Sea exhibits a narrow, complex ASF (Jacobs, 2004).

3. Methods

Three seismic profiles across the Adare Trough were collected on the RV/IB Palmer in 1997, oriented roughly E–W (Fig. 1). Migrated and interpreted profiles of the two northern lines, A–A' and B–B', are presented in Keller (2004) and Müller et al. (2005). A tie was made between the Adare Trough seismic lines and DSDP Site 274 using the analogue 1972 ELT52 seismic profile.

Fig. 8. Airy sediment unloading of basement for Adare Trough seismic profiles A–A', B–B', and C–C'. Approximate ages have been assigned to the eastern and western ends of the seismic profiles in order to estimate the expected basement depth based on a half-space cooling model (Parsons and Sclater, 1977) for calculating subsidence of oceanic crust. Expected basement depths differ from sediment unloaded depths by up to ~1900 m.

From 415 m of recovered sediment in DSDP 274, six sedimentary and five seismic units were identified and summarised by Müller et al. (2005). Here the five identified seismic units have been propagated onto Adare Trough seismic profile C–C'. Fig. 4 shows the correlation between the six identified sedimentary units from DSDP 274 and the five seismic units interpreted across profile C–C'. All three Adare Trough seismic profiles were examined with respect to (1) sedimentary features such as contourite and turbidite channels, and (2) faulting and igneous intrusion patterns. Reconstructions of oceanic palaeo-age and palaeo-basement depth for the area around the Adare Trough for 33 Ma, 17 Ma, 14 Ma, 5 Ma and the present were created from digital grids of the Circum-Antarctic region using the method outlined in Brown et al. (2006). These time-slices were selected because they are key time periods, with respect to the depositional history of the Adare Basin, relating to the onset and completion of the two extended unconformities present in the seismic profiles and DSDP Site 274.

For the mantle convection model, the mantle flow field through time was modeled using the spectral method of Hager and O'Connell (1981), based on spherical harmonic expansion of surface plate velocities and internal density heterogeneities at each depth level (Steinberger et al., 2004). Internal density heterogeneities were determined from the global tomographic model by Becker and Boschi (2002), using a conversion factor from relative seismic velocity to relative density variations of 0.25 below 220 km.

Steinberger et al. (2004) computed the change of density anomalies with time by advecting these back-

ward in the mantle flow field. The flow field in turn was computed from mantle density anomalies, and given surface plate velocities. While it is thought that in the upper part of the mantle beneath the lithosphere both seismic velocity and density anomalies are mostly due to temperature anomalies, and therefore should be strongly correlated, this is not necessarily the case at lithospheric depths. There lateral variations in composition may have an effect on both seismic velocity and density variations that is equally or even more important than lateral variations in temperature. Hence simply converting seismic velocity to density anomalies may not be entirely appropriate there. We focus on mantle density (equivalent to temperature) anomalies at 500 km depth, where Steinberger et al.'s (2004) model results are robust.

4. Results

4.1. Seismic stratigraphy

The data quality of profile C–C' and B–B' are similar, with interpretation of all five seismic units possible across both profiles. A detailed interpretation of seismic profile A–A' was not possible due to poor data quality caused by bad weather and equipment complications. Müller et al. (2005) presents seismic stratigraphic interpretations for profile A–A' and the western portion of profile B–B'. Here, we present the entire B–B' profile (Fig. 5) and the C–C' profile (Fig. 6). All seismic units were interpreted across profiles B–B' and C–C'. The basement is clearly identifiable throughout profile C–C' (Fig. 6), and an average overall sediment

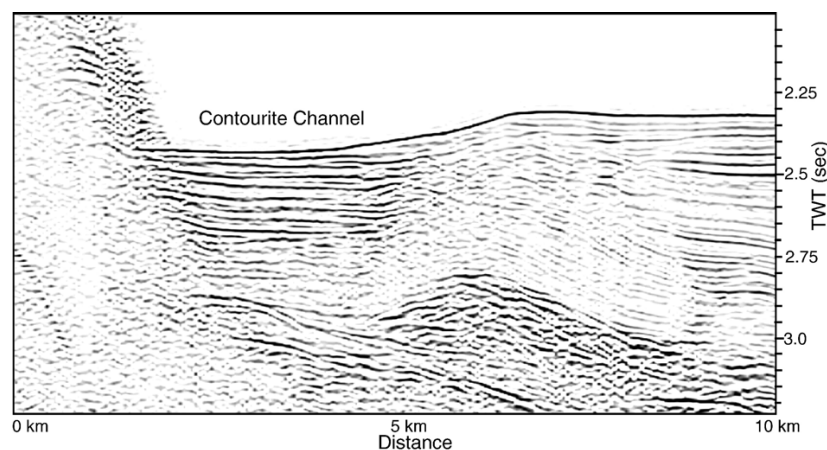


Fig. 9. Selected portion of seismic profile B–B' showing an interpreted contourite channel expressed at the seafloor, adjacent the eastern Adare Trough bounding ridge.

thickness of approximately 1000 ms exhibited by this profile is consistent with previously interpreted profiles A–A' and B–B'. Fig. 4 shows the relationship between mapped seismic units and the corresponding sedimentary units, as well as estimates of sediment ages summarised from Keller et al. (2004), Hayes et al. (1975) and Müller et al. (2005).

The top of seismic unit 6 (SU6) is marked by a distinct subbottom reflector marking the top of the basement structure. Magnetic data (Cande et al., 2000), constrain oceanic basement in this area to be no older than ~ 33 Ma (chron 13o) in the Adare central trough area. Strong reflectors, which separate seismically transparent layers above and below, define the upper contact of SU5. These reflectors are moderately laterally continuous in profile C–C' and the boundary between SU5 and SU3/4 is readily identified at most locations along the profile due to the presence of seismically transparent material above. A regionally consistent unconformity marks the top of seismic unit 3/4 in seismic profile. This unconformable

boundary is highly laterally continuous and readily traceable across profile C–C'. SU3/4 varies in thickness across the profile, increasing from an average thickness of 300 ms along the western section of the profile to an average thickness of 600 ms toward the east. This thickness increase combined with the onlapping relationship between SU3/4 and SU5 (CDP 15420 to 17420) clearly shows there was bathymetric relief prior to deposition of SU3/4. The sediments of SU3/4 filled the bathymetric trough that was present at the early Oligocene suggesting current controlled deposition rather than out-of-suspension deposition dominated. The top of seismic unit 2 is defined by a regionally consistent unconformity. The unconformity that defines the top of SU2 is not continuous across profile C–C', but is highly continuous when present. SU1 is not continuously present across profile C–C'. Reflectors of SU1 onlap onto SU2 at CDP 18300 to 19700, a relationship identified in profile B–B' (Müller et al., 2005). Generally, truncation and onlapping relationships between seismic units observed in profile

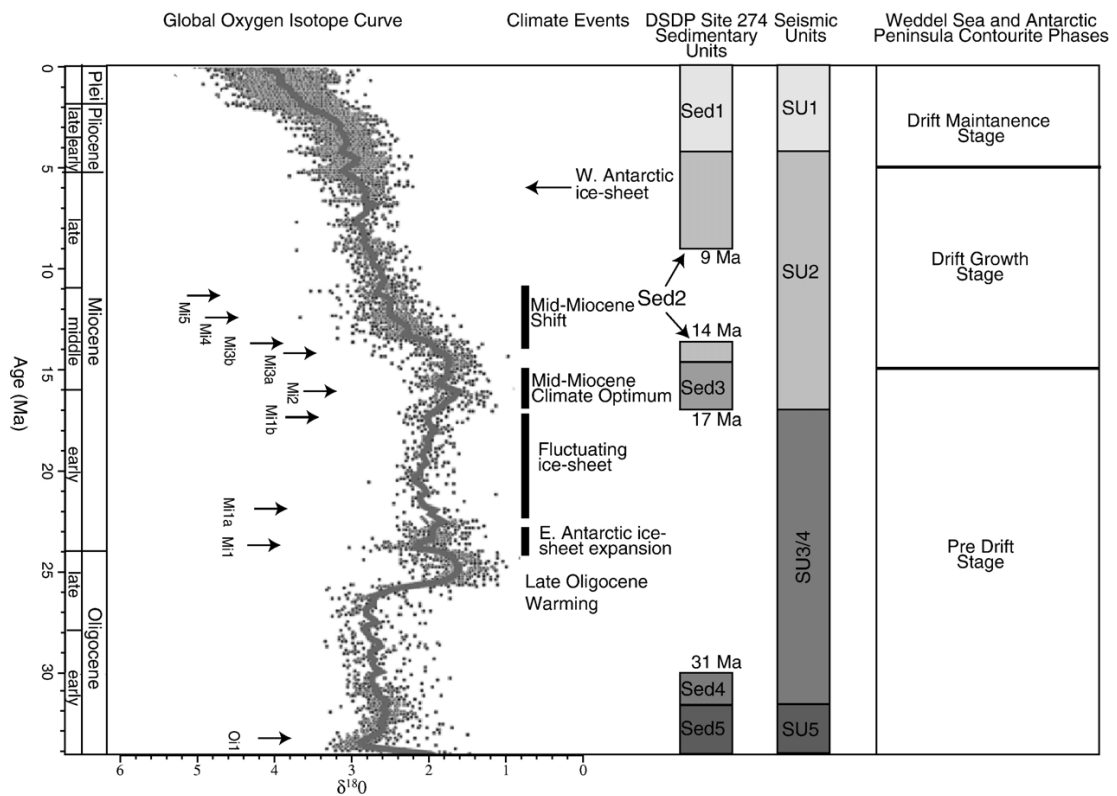


Fig. 10. Correlation of mapped seismic units with sedimentary units identified in DSDP Site 274 (Hayes et al., 1975) and ages from Hayes and Frakes (1975), the global oxygen isotope curve (Zachos et al., 2001), and the stages of contourite building identified from the Weddell Sea, Antarctica (Rebesco et al., 1997). Major climatic phases affecting Antarctica have been labeled, as have various glaciation events identified from the oxygen isotope curve.

C–C' are consistent with those observed for profile B–B' indicating that the seismic units interpreted have a regional extent.

4.2. Faults and intrusions

The bounding normal faults of the Adare Trough central graben are clearly visible in profiles A–A' and B–B', but are not visible in profile C–C'. Smaller faults, strike-slip/transensional in nature, were identified on all three

profiles with only minor offsets observed. No faults with reverse offsets were observed. Areas where sub-horizontal reflections in the seismic profile were disturbed in a vertical, roughly linear pattern were used to identify the location of strike-slip faults. The normal-faulted, central graben of the Adare Trough formed at 26–28 Ma, just after cessation of sea-floor spreading (Cande et al., 2000). Small faults offset the basement and SU5 and are inferred to be associated with Adare Trough rifting during the Oligocene. Generally, faults are more common near the central graben,

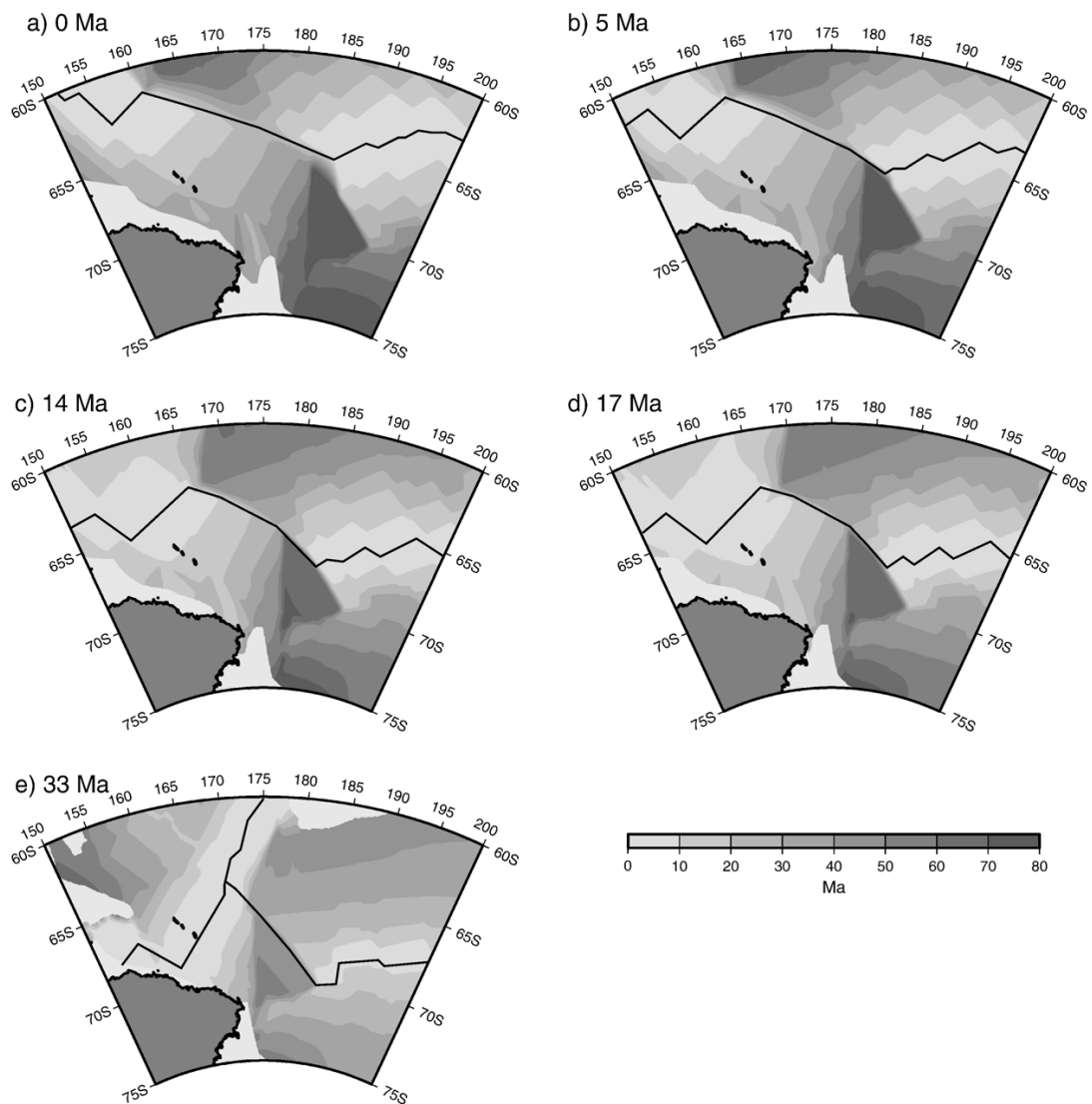


Fig. 11. Reconstructed basement maps showing palaeo-age of oceanic crust for times a) 0 Ma, b) 5 Ma, c) 14 Ma, d) 17 Ma, and e) 33 Ma.

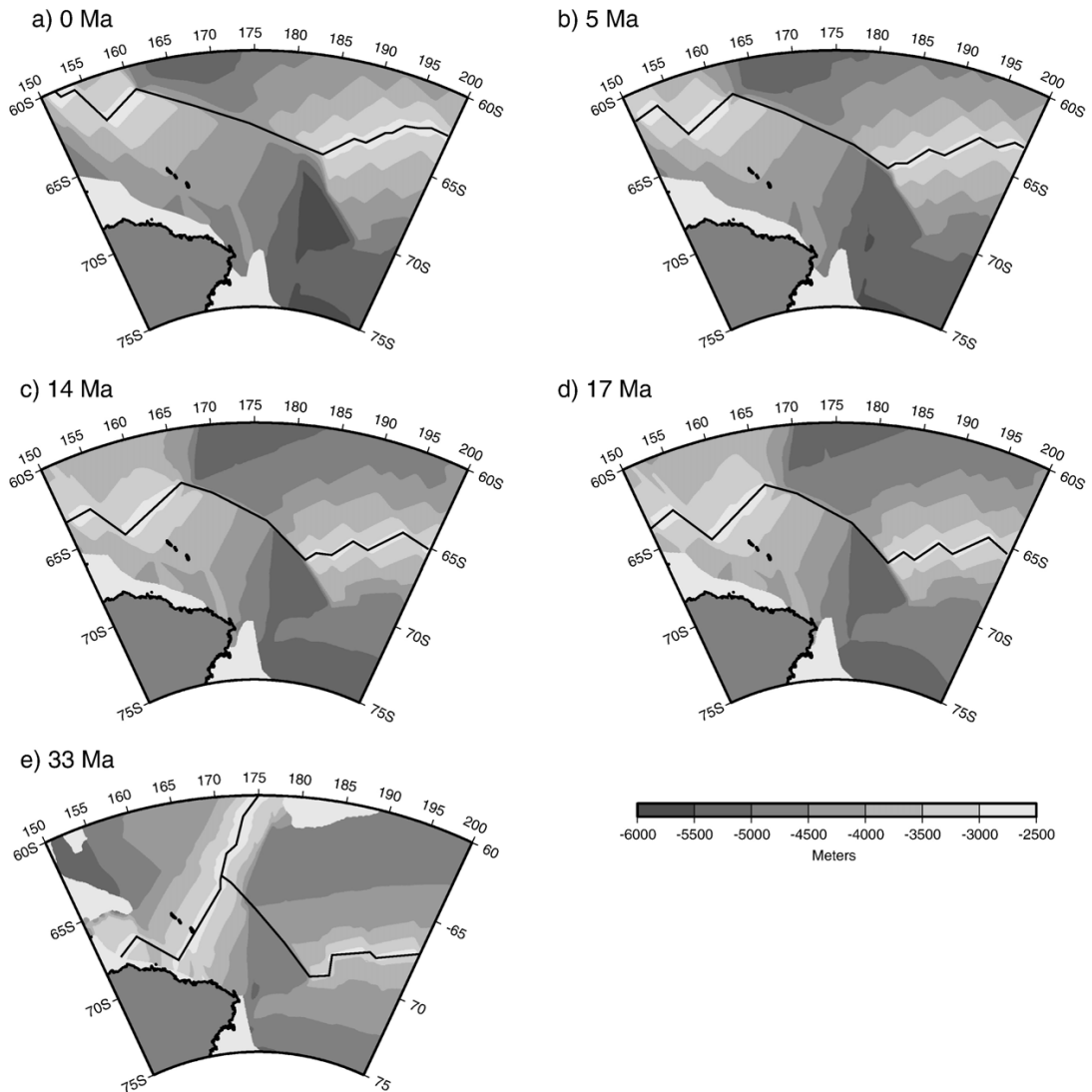


Fig. 12. Maps showing reconstructed palaeo-depth of oceanic basement for times a) 0 Ma, b) 5 Ma, c) 14 Ma, d) 17 Ma, and e) 33 Ma.

toward the western end of all seismic lines. Faults that propagate past SU5 continue to terminate prior to or during SU2, with sediments of SU1 remaining undisturbed.

Scattered intrusions throughout the Adare Trough range from affecting SU3/4 and SU5 only, to others that penetrate the entire stratigraphic column forming seamounts that are clearly recognisable in seismic and bathymetric profile. Similar small scale igneous intrusions found nearby, such as in the Balleny area, show that active Late Tertiary volcanism is widespread (LeMasurier and Thomson, 1990). The number of intrusions penetrating

the seismic units increases consistently from a low number of intrusions penetrating SU5 to a high number penetrating the modern seafloor.

5. Discussion

5.1. Structure and geodynamics

Small strike-slip/transensional faults exist in the Adare Basin seismic lines (e.g. Fig. 6). These faults likely reactivated major NW-trending pre-existing weaknesses,

which in the Adare Trough case are parallel/sub-parallel to the main bounding faults of the trough. The faults predominantly propagate to the middle of SU3/4, or near the top of SU2. The SU2 terminating faults halt below the Miocene–Pliocene unconformity indicating that extensional/transensional forces were active until approximately 5–15 Ma. On the adjacent continental crust, the Western Ross Sea also has a dominant set of right-lateral, strike-slip faults trending NW–SE, with N–S transtensional faults extending between the NW trending faults (Salvini et al., 1997; Salvini and Storti, 1999; Rossetti et al., 2003). Other NW–SE trending faults such as the Bower structure and the Rennick Graben occur in North and South Victoria Land (Davey and Brancolini, 1995; Rossetti et al., 2003).

Reconstructed upper mantle density anomalies (Steinberger et al., 2004) (Fig. 7) beneath the Victoria Land area show a prominent zone of downgoing dense mantle material from ~ 85 to ~ 65 Ma. A westward-dipping subduction zone existed adjacent to western Marie Byrd Land until 108 Ma (Storey et al., 1999) and eastern Marie Byrd Land until 90 Ma (Larter et al., 2002). The modelled upper mantle downwelling likely represents the continued slab subduction from the Marie Byrd Land subduction zone. The modelled downwelling is rounded in shape, rather than an expected linear feature, most probably due to resolution limitations of the mantle density anomaly model.

From 55 Ma to the present (Fig. 7), anomalously less dense mantle material beneath the Victoria Land area progressively intensifies and expands to connect with other regions of less dense mantle material underlying much of the South Pacific and Marie Byrd Land (Fig. 7). Using a 50–100 km/Ma (Steinberger and Antretter, submitted for publication) upwelling rate for upper mantle material there should be a 5–10 million yr delay between modelled upwelling mantle at 500 km depth and any likely surface effects, such as volcanism. Igneous activity in Northern Victoria Land is recorded from ~ 50 Ma and has been practically continuous since 38 Ma (Tonarini et al., 1997; Armienti and Baroni, 1999), while further south the McMurdo volcanic group commenced later, at 25–18 Ma and has continued to the present day with intensification at ~ 10 Ma (Davey and Brancolini, 1995). On the other side of the Ross Sea, Marie Byrd Land has undergone contemporaneous uplift and volcanism from 29–25 Ma to the present (LeMasurier, 2006). Therefore, we suggest that initial onset of igneous activity in Northern Victoria Land at ~ 50 Ma was caused by a large-scale mantle upwelling. Later onset of igneous activity in McMurdo Sound (25–18 Ma to the present) and Marie Byrd Land (29–25 Ma) can

also be attributed to the region mantle density anomaly upwelling.

Large regions of low-volume, alkaline, Cenozoic magmatism are observed not only in Western Antarctica but also in eastern Australia, the New-Zealand-Campbell Plateau area, and much of the intervening oceanic crust. The ‘superswell’ hypothesis (McNutt and Fischer, 1987; Stein and Stein, 1993; Finn et al., 2005) may explain this phenomenon. Finn et al. (2005) propose that Cenozoic detachment and sinking of subducted slabs from the mantle transition zone caused a modest increase in asthenospheric temperature leading to melting of overlying metasomatised lithosphere (Finn et al., 2005). Eruption then occurred in small volcanic fields under compressive regimes, and in large volume fields under extensional regimes. The spatial relationship between igneous activity and faulting in the Adare Basin supports the ‘superswell’ mechanism for volcanism by showing that most observed volcanism could not have been caused by a rift related mechanism. There is a relationship between seamounts the large normal faults of the central Adare Trough graben (Fig. 2). However, there are no normally faulted blocks in the Adare Basin and there is not a spatial correlation between smaller strike-slip/transensional faults, and intrusions (Figs. 2 and 6). So, the bounding faults of the Adare Trough provide a zone of weakness enabling intrusion of igneous material but intrusions in the region are not consistently related to faulting, indicating that adiabatic decompression, caused by rifting, was not the main mechanism behind emplacement of igneous material.

In Fig. 8 we compare the observed, and sediment unloaded, basement depths for seismic lines A–A', B–B', and C–C'. Ages estimates have been assigned to the eastern and western ends of the seismic profiles based on Cande et al. (2000) in order to compare the observed unloaded basement depth with the expected basement depth for oceanic crust based on a half-space cooling model (Parsons and Sclater, 1977). Fig. 8 shows that unloaded Adare Basin basement is substantially shallower than expected for 25–40 million yrs old oceanic crust. The unloaded basement depth of the Adare Trough graben in profile A–A' is ~ 1400 m shallower than expected basement depth, in profile B–B' it is ~ 1600 m shallower, and in profile C–C' it is ~ 1900 m shallower. Similarly, the unloaded basement depth of the Adare Trough flanks, excluding the bounding ridges, in profile A–A' is ~ 1300 m shallower than expected basement depth, in profile B–B' it is ~ 1600 m shallower, and in profile C–C' (excluding the Hallett Ridge) it is ~ 1900 m shallower. These data reveal unloaded basement of the Adare Trough graben and flanks shallows from north to south with

respect to expected basement depth. The shallowness of the bounding ridges can be explained by flexural uplift caused by mechanical unloading of the lithosphere at the bounding faults (Müller et al., 2005).

The anomalous elevation of the Adare Trough graben and flanks may be caused by anomalously thick crust and/or dynamic topography caused by mantle upwelling. As discussed above, the Adare Basin region has likely been located above anomalously hot mantle since ~ 55 Ma, which supports a mantle upwelling mechanism for shallow Adare Basin basement depths. Directly beneath the Adare Trough, on profiles A–A' and B–B', is an unexpectedly large modelled oceanic crustal thickness maximum of 9–10.5 km (Müller et al., 2005). However, modelled oceanic crustal thickness beneath the flanks of these lines is not anomalously thick (Müller et al., 2005) again supporting mantle upwelling as the cause for shallow basement depths of the Adare Trough flanks.

5.2. Patterns of sedimentation and possible causes

Mid-Oligocene East Antarctic glacial expansion caused a drop in sea level (Haq et al., 1988) and the onset of the ACC through initiation of a modern ocean structure with constant Southern Ocean westerly winds (Hay et al., 2005). The mid-Oligocene onset of widespread Australasian submarine erosion, resulting in the Australasian Marshall Paraconformity, is widely assumed to represent erosion by the ACC (McGonigal and Di Stefano, 2002). Our SU3/4 unconformity, dated as Early Oligocene–late Early Miocene from DSDP Site 274 (Hayes et al., 1975), see Fig. 4, corresponds temporally with the Marshall Paraconformity. However, similar mid-Oligocene unconformities are not observed at other Antarctic continental slope locations such as DSDP Sites 268 and 269 (Hayes and Frakes, 1975), the Weddell Sea (Michels et al., 2001) or Antarctic Peninsula (Rebesco et al., 1997). In fact, the period 36–15 Ma is identified as a “Pre-Drift” stage for the Weddell Sea and Antarctic Peninsula where turbidite deposits dominated and strong bottom currents are yet to initiate (Rebesco et al., 1997). Further, DSDP Site 268, located on the continental rise offshore Wilkes Land, Antarctica, exhibits turbidite dominated sediments overlain by contour current dominated sediments (Piper and Brisco, 1975). Also, the Antarctic continental slope lies far to the south of the present-day location of the ACC and so is unlikely to have been influenced by the onset of the ACC at the mid-Oligocene.

We propose that our regional SU3/4 hiatus is more likely due to a low sediment supply reaching the Southern Ocean from the Western Ross Sea. Brancolini et al. (1995)

described seismic unit RSS-1 (Oligocene to late Early Miocene; Davey et al., 2000) as being deposited in marine Western Ross Shelf subsiding basins that were isolated/restricted from the Southern Ocean. Isolated basins in the Ross Sea would have severely restricted sediment supply from the Antarctic continent to the Adare Basin region, causing the SU3/4 unconformity.

Sedimentation in the Adare Basin region resumed at ~ 17 Ma (SU2) and continued to ~ 14 Ma, see Fig. 10. Sed3 (~ 17 to ~ 15 Ma) exhibits turbidite deposited graded bedding (Hayes et al., 1975) and a higher sedimentation rate than Sed2 (Frakes, 1975), which are both suggestive of relatively weak bottom currents. Deposition of Sed3 occurred during the Mid-Miocene climate optimum (McGowran, 1979) the warmest interval of the Neogene. These warm conditions led to erosion of the TransAntarctic Mountains by temperate glaciers (Barrett, 1999). Also, the Ross Sea palaeo-environment at ~ 17 Ma changed from isolated basins to open marine conditions (Brancolini et al., 1995). High sediment availability from temperate glacier erosion of the TransAntarctic Mountains and open marine conditions in the Ross Sea would have been favourable to increased sediment supply to the Adare Basin leading to the deposition of Sed3.

A distinct change in depositional style occurs from Sed3 to Sed2. Sed2 is affected by contour channels (e.g. Fig. 9), there is severe sediment winnowing (Frakes, 1975), and the unit is split by a seismically transparent, unconformity, lasting from the Mid-Miocene to the Pliocene (Hayes et al., 1975). Fig. 10 shows the correlation between initial deposition of Sed2 and onset of Mid-Miocene cooling (Shackleton and Kennett, 1975; Miller et al., 1991). The present-day structure of the ocean, with well defined ocean fronts, is a consequence of the location of the westerly winds and consistent high-pressure systems at the poles related to the presence of ice cover (Hay et al., 2005). Globally warmer conditions would lead to seasonal alternations of high and low pressure systems and a general absence/weakening of polar fronts (Hay et al., 2005). The cooling caused intensification of gyral circulation and increased the strength of oceanographic fronts (Thunell and Belyea, 1982; Kennett et al., 1985). A consequence of increased sea-ice cover and a stronger Antarctic Slope Front, due to glacial expansion, was increased production of AABW from the mid-Miocene. These strong bottom currents continued, leading to the winnowed sediment and hiatus observed in Sed2, until the Pliocene (see Fig. 10). Increased bottom current intensity is inferred for much of the Antarctic margin for the period ~ 15 to ~ 5 Ma. For example, a “Drift-growth Stage” (~ 15 to ~ 5 Ma) characterised by strong bottom currents is identified in

Weddell Sea and Antarctic Peninsula deposits (Rebesco et al., 1997; Michels et al., 2001).

SU1 exhibits contour channels (Fig. 9) indicating the influence of bottom currents. However, sedimentation rates implied for this seismic unit from correlation with DSDP Site 274 are higher than for Sed2 and winnowing is not apparent (Frakes, 1975). This suggests that bottom currents were weakened from the Pliocene to the present although the timing of the boundary between SU2 and SU1 through correlation with Site 274 is debatable (Barker, 1995). Seismic evidence from the Weddell Sea and Antarctic Peninsula, supports weaker bottom currents since ~ 5 Ma (Rebesco et al., 1997; Michels et al., 2001). Some Antarctic warming (e.g. Poore and Sloan, 1996; Lear et al., 2003; Billups and Schrag, 2003) occurred at ~ 5 Ma, possibly leading to decreased production of AABW. Initiation of Northern Hemisphere icesheets at ~ 3 Ma caused a change in global deep-water circulation patterns (Ishman, 1996), which may also have affected AABW production. Either, or both, of these climatic changes may have reduced bottom current strength in the Adare Basin area.

Keller (2004) noted that sediment cover on the western side of the Adare Trough (approx. 100 km from the central graben) is much thicker than on the eastern side. Hayes and Frakes (1975) first suggested that local bathymetric features may have directed and intensified bottom currents in this area and Orsi et al. (1999) found that AABW moved from the Ross Shelf past the western side of the Adare Trough (Fig. 1). This bottom water flow is likely to have carried and deposited much of the thicker sediment observed west of the Adare Trough. However, the AABW flow pattern may have been different in the past, largely depending on bathymetric configurations. Mid-ocean ridges and transform faults can form significant barriers to bottom current flow (Bice et al., 1998). Figs. 11 and 12 show that although there has been substantial change in the orientation of mid-ocean ridges offshore Cape Adare there is no modelled mid-ocean ridge impediment to bottom current flow between the Ross Shelf and the Adare Basin. However, it is possible that transform faults, related to the mid-ocean ridge, may have impeded AABW flow.

6. Conclusions

Sediments deposited in the Adare Basin since ~ 38 Ma have been strongly influenced by environmental factors. Progressive global cooling since the Eocene has changed global circulation patterns, leading to the onset of ACC during the mid-Oligocene and AABW during the mid-

Miocene. The Oligocene onset of the ACC does not appear to have played a large role in causing the Oligocene/Miocene hiatus observed across the Adare Basin, with no comparable hiatuses observed elsewhere on the Antarctic margin. We suggest that this hiatus was caused by low sediment availability to the Adare Basin due to the presence of small, isolated basins in the adjacent Ross Sea with limited connection to the Southern Ocean. During the mid-Miocene there was a change to more open marine conditions in the Ross Sea as well as increased global cooling leading to increased Antarctic glaciation. We suggest that increased AABW production in the Western Ross Sea at this time led to strong bottom currents flowing from the Ross Sea down the continental slope leading to winnowed sediments and the late Miocene hiatus in the Adare Basin. Further cooling during the Pliocene, causing changes in global ocean circulation patterns, correlates with continuing but weakened bottom currents affecting the Adare Basin. The sediment deposition patterns observed in the Adare Basin agree with sediment deposition patterns observed at other Antarctic margin locations e.g. the Antarctic Peninsula and the Weddell Sea, supporting regional environmentally driven sediment deposition mechanisms.

Small-scale volcanism and unusually shallow basement depths are found throughout the Adare Trough area. Mantle density reconstructions showing anomalously hot mantle beneath the Adare Trough area support mechanism for both the observed volcanism and shallow basement depths.

References

- Armienti, P., Baroni, C., 1999. Cenozoic climate change in Antarctica recorded by volcanic activity and landscape evolution. *Geology* 27 (7), 617–620.
- Barker, P.F., 1995. The proximal marine sediment record of Antarctic climate since the Late Miocene. Antarctic Research Series. *Geology and Seismic Stratigraphy of the Antarctic Margin*, vol. 68, pp. 25–57.
- Barrett, P., 1999. Antarctic climate history over the last 100 million years. *Terra Antarctica* 3, 53–72.
- Becker, T., Boschi, L., 2002. A comparison of tomographic and geodynamic mantle models. *Geochem. Geophys. Geosyst.* 3 (1), doi:10.1029/2001GC000168.
- Bice, K.L., Barron, E.J., Peterson, W.H., 1998. Reconstruction of realistic early Eocene paleobathymetry and ocean GCM sensitivity to specified basin configuration. In: Crowley, T.J., Burke, K. (Eds.), *Tectonic Boundary Conditions for Climate Reconstructions*. Oxford University Press, Oxford, pp. 227–247.
- Billups, K., Schrag, D.P., 2003. Application of benthic foraminiferal Mg/Ca ratios to questions of Cenozoic climate change. *Earth Planet. Sci. Lett.* 209, 181–195.
- Blackman, D.K., Herzen, R.P.V., Lawver, L.A., 1987. Heat flow and Tectonics in the Western Ross Sea, Antarctica, *The Antarctic*

- Continental Margin: Geology and Geophysics of the Western Ross Sea, Houston, Texas.
- Brambati, A., Melis, R., Quaià, T., Salvi, G., 2002. Late Quaternary climatic changes in the Ross Sea area, Antarctica. In: Gamble, J.A., Skinner, D.N.B., Henrys, S. (Eds.), *Antarctica at the Close of the Millennium*. Royal Society New Zealand, Wellington, pp. 359–364.
- Brancolini, G., Cooper, A.K., Coren, F., 1995. Seismic facies and glacial history in the Western Ross Sea (Antarctica). *Antarct. Res. Ser.* 68, 209–233.
- Brown, B., Gaina, C., Müller, R.D., 2006. Circum-Antarctic palaeobathymetry: illustrated examples from Cenozoic to recent times. *Palaeogeogr. Palaeoclimatol. Palaeoecol.* 231, 158–168.
- Budillon, G., Tucci, S., Artegiani, A., Spezie, G., 1999. Water masses and suspended matter characteristics of the western Ross Sea. In: Faranda, F.M., Guglielmo, L., Ianora, A. (Eds.), *Ross Sea Ecology*. Springer, Berlin, pp. 63–81.
- Budillon, G., Fusco, G., Spezie, G., 2000. A study of surface heat fluxes in the Ross Sea (Antarctica). *Antarct. Sci.* 12 (2), 243–254.
- Cande, S.C., Stock, J.M., Müller, R.D., Ishihara, T., 2000. Cenozoic motion between East and West Antarctica. *Nature* 404 (6774), 145–150.
- Cape Roberts Science Team, 1998. Studies from the Cape Roberts Project, Ross Sea, Antarctica—initial report on CRP-1. In: Ricci, C.A. (Ed.), *Terra Antarctica. Museo Nazionale dell'Antartide*, Siena, pp. 1–187.
- Cape Roberts Science Team, 1999. Studies from the Cape Roberts Project, Ross Sea, Antarctica—initial report on CRP-2/2A. In: Ricci, C.A. (Ed.), *Terra Antarctica. Museo Nazionale dell'Antartide*, Siena, pp. 1–173.
- Cape Roberts Science Team, 2000. Studies from the Cape Roberts Project, Ross Sea, Antarctica—initial report on CRP-3. In: Ricci, C.A. (Ed.), *Terra Antarctica. Museo Nazionale dell'Antartide*, Siena, pp. 1–209.
- Cooper, A.K., Davey, F.J., 1985. Episodic rifting of Phanerozoic rocks in the Victoria Land Basin, Western Ross Sea, Antarctica. *Science* 229, 1085–1087.
- Cooper, A.K., Davey, F.J., Behrendt, J.C., 1987a. Seismic stratigraphy and structure of the Victoria Land Basin, western Ross Sea, Antarctica. In: Cooper, A.K., Davey, F.J. (Eds.), *The Antarctic Continental Margin: Geology and Geophysics of the Western Ross Sea*. Circum-Pacific Council for Energy and Mineral Resources Earth Science Series. Circum-Pacific Council for Energy and Mineral Resources, Houston, pp. 17–26.
- Cooper, A.K., Davey, F.J., Cochrane, G.R., 1987b. Structure of extensionally rifted crust beneath the western Ross Sea and Iselin Bank, Antarctica, from sonobuoy seismic data. The Antarctic continental margin; geology and geophysics of the western Ross Sea. Circum-Pacific Council for Energy and Mineral Resources, Earth Science Series, vol. 5B, pp. 93–118.
- Cooper, A.K., Davey, F.J., Hinz, K., 1991. Crustal extension and origin of sedimentary basins beneath the Ross Sea and Ross Ice Shelf, Antarctica. In: Thomson, Crame, Thomson (Eds.), *Geological Evolution of Antarctica*. Cambridge University Press, pp. 285–292.
- Dalziel, I.W.D., Elliot, D.H., 1982. West Antarctica: Problem child of Gondwanaland. *Tectonics* 1, 3–19.
- Danesi, S., Morelli, A., 2000. Group velocity of Rayleigh waves in the Antarctic region. In: Badal, J. (Ed.), *Developments in Imaging and Seismic Tomography of the Lithosphere–Asthenosphere System*. Elsevier, Amsterdam, pp. 55–66.
- Danesi, S., Morelli, A., 2001. Structure of the upper mantle under the Antarctic plate from surface wave tomography. *Geophys. Res. Lett.* 28, 4395–4398.
- Davey, F.J., Brancolini, G., 1995. The late Mesozoic and Cenozoic structural setting of the Ross Sea region. *Antarct. Res. Ser.* 68, 167–182.
- Davey, F.J., et al., 2000. A revised correlation of the seismic stratigraphy at the Cape Roberts drill sites with the seismic stratigraphy of the Victoria Land Basin, Antarctica. *Terra Antarctica* 7, 215–220.
- DiVenere, V., Kent, D.V., Dalziel, I.W.D., 1994. Mid-Cretaceous paleomagnetic results from Marie Byrd Land, West Antarctica: A test of post-100 Ma relative motion between East and West Antarctica. *J. Geophys. Res.* 99, 15115–15139.
- Faugeres, J.C., Stow, D.A.V., Imbert, P., Viana, A., 1999. Seismic features diagnostic of contourite drifts. *Mar. Geol.* 162 (1), 1–38.
- Finn, C.A., Müller, R.D., Panter, K.S., 2005. A Cenozoic diffuse alkaline magmatic province (DAMP) in the southwest Pacific without rift or plume origin. *Geochem. Geophys. Geosyst.* 6 (1), 1–26.
- Fitzgerald, P.G., 1992. The Transantarctic Mountains of southern Victoria Land: The application of apatite fission track analysis to a rift shoulder uplift. *Tectonics* 11, 634–662.
- Fitzgerald, P.G., 1994. Uplift of the transantarctic mountains: constraints from fission track thermochronology. In: van der Wateren Frederik, M., Verbers, A.L.L.M., Tessensohn, F. (Eds.), *Landscape Evolution in the Ross Sea Area, Antarctica*. Rijks Geologische Dienst, Haarlem, pp. 41–45.
- Fitzgerald, P.G., Gleadow, A.J.W., 1988. Fission-track geochronology, tectonics and structure of the Transantarctic Mountains in northern Victoria Land, Antarctica. *Chemical Geology (Isotope Geoscience Section)* 73, 169–198.
- Foldvik, A., Gammelsrod, T., Torresen, T., 1985. Circulation and water masses on the southern Weddell Sea shelf. *Antarct. Res. Ser.* 43, 5–20.
- Frakes, L.A., 1975. Paleoclimatic significance of some sedimentary components at Site 274. *Initial Reports of the Deep Sea Drilling Project*. U.S. Government Printing Office, Washington, pp. 785–787.
- Hager, B.H., O'Connell, R.J., 1981. A simple global model of plate dynamics and mantle convection. *J. Geophys. Res.* 86, 4843–4867.
- Haq, B.U., Hardenbol, J., Vail, P.R., 1988. Mesozoic and Cenozoic Chronostratigraphy and Cycles of Sea-level Change. *Society of Economic Paleontologists and Mineralogists*, pp. 72–108.
- Hay, W., Flögel, S., Söding, E., 2005. Is the initiation of glaciation on Antarctica related to a change in the structure of the ocean? *Glob. Planet. Change* 45, 23–33.
- Hayes, D.E., Davey, F.J., 1975. A Geophysical Study of the Ross Sea, Antarctica, Initial Reports of the Deep Sea Drilling Project. U.S. Government Printing Office, Washington.
- Hayes, D.E., Frakes, L.A., 1975. General synthesis deep sea drilling project, Leg 28. *Initial Reports of the Deep Sea Drilling Project*, vol. 28, pp. 919–942.
- Hayes, D.E., et al., 1975. Site 274. *Initial Reports of the Deep Sea Drilling Project*. U.S. Government Printing Office, Washington, pp. 369–433.
- Heezen, B.C., Hollister, C.D., Ruddiman, W.F., 1966. Shaping the continental rise by deep geostrophic contour currents. *Science* 152, 502–508.
- Ishman, S.E., 1996. A benthic foraminiferal record of middle to late Pliocene (3.15–2.85 Ma) deep water change in the North Atlantic Marine Micropaleontology, 27: 165–180.
- Jacobs, S.S., 1991. On the nature and significance of the Antarctic Slope Front. *Mar. Chem.* 35, 9–24.
- Jacobs, S.S., 2004. Bottom water production and its links with the thermohaline circulation. *Antarct. Sci.* 16 (4), 427–437.
- Jacobs, S.S., Fairbanks, R.G., Horibe, Y., 1985. Origin and evolution of water masses near the Antarctic continental margin: evidence from $H_2^{18}O/H_2^{16}O$ ratios in seawater. *Antarct. Res. Ser.* 43, 59–85.

- Keller, W.R., 2004. Cenozoic Plate Tectonic Reconstructions and Plate Boundary Processes in the Southwest Pacific. California Institute of Technology, Pasadena, California.
- Kennett, J.P., Keller, G., Stinivasan, M.S., 1985. Miocene Planktonic Foraminiferal Biogeography and Paleooceanographic Development of the Indo-Pacific Region. *The Miocene Ocean*. *Geol. Soc. of Amer. Memoir*, vol. 163, pp. 197–236.
- Killworth, P.D., 1979. On “chimney” formations in the ocean. *J. Phys. Oceanogr.* 9, 531–554.
- Kuvaas, B., et al., 2005. Interplay of turbidite and contourite deposition along the Cosmonaut Sea/Enderby Land margin, East Antarctica. *Mar. Geol.* 217, 143–159.
- Kyle, P.R., 1990. McMurdo volcanic group, western ross embayment: introduction. *Antarct. Res. Ser.* 48, 19–25.
- Larter, R.D., Cunningham, A.P., Barker, P.F., Gohl, K., Nitsche, F.O., 2002. Tectonic evolution of the Pacific margin of Antarctica 1. Late Cretaceous tectonic reconstructions. *J. Geophys. Res.-Solid Earth* 107 (B12), 2345–2345.
- Lear, C.H., Rosenthal, Y., Wright, J.D., 2003. The closing of a seaway: ocean water masses and global climate change. *Earth Planet. Sci. Lett.* 210, 425–436.
- LeMasurier, W.E., 1990. Late cenozoic volcanism on the antarctic plate: an overview. In: LeMasurier, W.E., Thomson, J.W. (Eds.), *Volcanoes of the Antarctic Plate and Southern Oceans*. Antarctic Research Series. American Geophysical Union, Washington, DC, pp. 1–18.
- LeMasurier, W.E., 2006. What supports the Marie Byrd Land Dome? An evaluation of potential uplift mechanisms in a continental rift system. In: Fütterer, D.K., Damaske, D., Kleinschmidt, G., Miller, H., Tessensohn, F. (Eds.), *Antarctica Contributions to Global Earth Sciences*. Springer, pp. 299–302.
- LeMasurier, W.E., Thomson, J.W. (Eds.), 1990. *Volcanoes of the Antarctic Plate and Southern Ocean*. Antarctic Research Series, vol. 48. American Geophysical Union, Washington, DC.
- McGonigal, K., Di Stefano, A., 2002. Calcareous nannofossil biostratigraphy of the Eocene–Oligocene transition, ODP Sites 1123 and 1124. *Proceedings of the Ocean Drilling Program, Scientific Results*, vol. 181, pp. 1–22.
- McGowran, B., 1979. The tertiary of Australia: foraminiferal overview. *Mar. Micropaleontol.* 4, 235–264.
- McNutt, M.K., Fischer, K.M., 1987. The south pacific superswell. In: Keating, B., Batiza, R. (Eds.), *Seamounts, Islands, and Atolls*. American Geophysical Union, Washington, DC, pp. 25–34.
- McPhee, M.G., 2003. Is thermobaricity a major factor in Southern Ocean ventilation? *Antarct. Sci.* 15, 153–160.
- Michels, K.H., Rogenhagen, J., Kuhn, G., 2001. Recognition of contour-current influence in mixed contourite–turbidite sequences of the Western Weddell Sea, Antarctica. *Mar. Geophys. Res.* 22, 465–485.
- Miller, K.E., Wright, J.D., Fairbanks, R.G., 1991. Unlocking the ice house: Oligocene–Miocene oxygen isotopes, eustasy and margin erosion. *J. Geophys. Res.* 96, 6829–6848.
- Müller, R.D., Cande, S.C., Stock Joann, M., Keller, B., 2005. Crustal structure and rift flank uplift of the Adare Trough, Antarctica. *Geochem. Geophys. Geosyst.*
- Orsi, A.H., Johnson, G.C., Bullister, J.L., 1999. Circulation, mixing and production of Antarctic bottom water. *Prog. Oceanogr.* 43, 55–109.
- Parsons, B., Sclater, J.G., 1977. An analysis of the variation of ocean floor bathymetry and heat flow with age. *J. Geophys. Res.* 82 (5), 803–827.
- Piper, D.J.W., Brisco, C.D., 1975. Deep-water continental margin sedimentation, DSDP Leg 28, Antarctica. *Initial Reports of the Deep Sea Drilling Project*, vol. 28, pp. 727–755.
- Pistolato, M., et al., 2006. Grain size, mineralogy and geochemistry in Late Quaternary sediments from the Western Ross Sea outer slope as proxies for climate changes. In: Fütterer, D.K., Damaske, D., Kleinschmidt, G., Miller, H., Tessensohn, F. (Eds.), *Antarctica Contributions to Global Earth Sciences*. Springer, pp. 423–432.
- Poore, R.Z., Sloan, L.C., 1996. Introduction climates and climate variability of the Pliocene. *Mar. Micropaleontol.* 27 (1), 1–2.
- Rebesco, M., Stow, D., 2001. Seismic expression of contourites and related deposits: a preface. *Mar. Geophys. Res.* 22, 303–308.
- Rebesco, M., Larter, R.D., Camerlenghi, A., Barker, P.F., 1996. Giant sediment drifts on the continental rise west of the Antarctic Peninsula. *Earth Planet. Sci. Lett.* 191, 241–255.
- Rebesco, M., Larter, R.D., Barker, P.F., Camerlenghi, A., Vanneste, L.E., 1997. The history of sedimentation on the Continental Rise West of the Antarctic Peninsula. *Antarct. Res. Ser.* 71, 29–49.
- Rebesco, M., et al., 2002. Sediment drifts and deep-sea channel systems, Antarctic Peninsula Pacific Margin. In: Stow, D.A.V., Pudsey, C.J., Howe, J.A., Faugeres, J.C., Viana, A. (Eds.), *Deep-Water Contourite Systems: Modern Drifts and Ancient Series, Seismic and Sedimentary Characteristics*. *Geol. Soc., London*, pp. 353–371.
- Ritzwoller, M.H., Shapiro, N.M., Levshin, A.L., Leahy, G.M., 2001. Crustal and upper mantle structure beneath Antarctica and surrounding oceans. *J. Geophys. Res., B Solid Earth Planets* 106 (12), 30,645–630,670.
- Rossetti, F., Lisker, F., Storti, F., Laufer, A.L., 2003. Tectonic and denudational history of the Rennick Graben (North Victoria Land): Implications for the evolution of rifting between East and West Antarctica. *Tectonics* 22 (2), 1016–1016.
- Rubino, A., Budillon, G., Pierini, S., Spezie, G., 2003. A model for the spreading and sinking of the Deep Ice Shelf Water in the Ross Sea. *Antarct. Sci.* 15, 25–30.
- Salvini, F., Storti, F., 1999. Cenozoic tectonic lineaments of the Terra Nova Bay region, Ross Embayment, Antarctica. *Glob. Planet. Change* 23 (1–4), 129–144.
- Salvini, F., et al., 1997. Cenozoic geodynamics of the Ross Sea region, Antarctica: crustal extension, intraplate strike-slip faulting, and tectonic inheritance. *J. Geophys. Res.* 102 (B11), 24669–24696.
- Shackleton, N.J., Kennett, J.P., 1975. Paleotemperature History of the Cenozoic and the Initiation of Antarctic Glaciation: Oxygen and Carbon Isotope Analysis in D.S.D.P. Sites 277, 279, and 281. In: Kennett, J.P., Houtte, R.E., et al. (Eds.), *Initial Reports of the Deep Sea Drilling Program*. U.S. Government Printing Office, Washington, DC.
- Stein, C.A., Stein, S., 1993. Constraints on Pacific midplate swells from global depth–age and heat flow–age models. In: Pringle, M.S., Sager, W.W., Sliter, W.V., Stein, S. (Eds.), *The Mesozoic Pacific: Geology, Tectonics, and Volcanism*. *Geophysical Monograph*. American Geophysical Union, Washington, DC, pp. 53–76.
- Steinberger, B., Antretter, M., submitted for publication. Conduit diameter and buoyant rising speed of mantle plumes—implications for the motion of hotspots and shape of plume conduits. *Geochem. Geophys. Geosyst.*
- Steinberger, B., Sutherland, R., O’Connell, R.J., 2004. Prediction of Emperor-Hawaii seamount locations from a revised model of global plate motion and mantle flow. *Nature* 430, 167–173.
- Storey, B.C., et al., 1999. Mantle plumes and Antarctica–New Zealand rifting: evidence from mid-Cretaceous mafic dykes. *J. Geol. Soc.* 156 (Part 4), 659–671.
- Thunell, R., Belyea, P., 1982. Neogene planktonic foraminiferal biogeography of the Atlantic Ocean. *Micropaleontology* 28, 381–398.
- Tonarini, S., Rocchi, S., Armienti, P., Innocenti, F., 1997. Constraints on timing of Ross sea rifting inferred from Cainozoic intrusions from

- northern Victoria Land, Antarctica. In: Ricci, C.A. (Ed.), *The Antarctic Region: Geological Evolution and Processes*. Terra Antarctica Publ, pp. 511–521.
- U.S. Department of Commerce, N.O.A.A., National Geophysical Data Center, 2001. 2-minute Gridded Global Relief Data (ETOPO2), <http://www.ngdc.noaa.gov/mgg/fliers/01mgg04.html>.
- Whitworth III, T., 1998. Water masses and mixing near the Antarctic Slope Front. *Antarct. Res. Ser.* 75, 1–27.
- Wilson, T.J., 1992. Mesozoic and Cenozoic kinematic evolution of the Transantarctic Mountains. In: Yoshida, Y., Kaminuma, K., Shiraishi, K. (Eds.), *Recent Progress in Antarctic Earth Science*. Terra Scientific Publishing, Tokyo, pp. 303–314.
- Wilson, T.J., 1995. Cenozoic transtension along the Transantarctic Mountains–West Antarctic Rift boundary, southern Victoria Land, Antarctica. *Tectonics* 14 (2), 531–545.
- Zachos, J., Pagani, M., Sloan, L., Thomas, E., Billups, K., 2001. Trends, rhythms, and aberrations in global climate 65 Ma to present. *Science* 292 (Apr 27), 686–693.

Chapter 4

Sunda-Java trench kinematics, slab window formation and overriding plate deformation since the Cretaceous

Sunda-Java trench kinematics, slab window formation and overriding plate deformation since the Cretaceous

J.M. Whittaker*, R.D. Müller, M. Sdrolias, C. Heine

EarthByte Group, School of Geosciences, University of Sydney, Sydney, Australia

Received 20 June 2006; received in revised form 12 December 2006; accepted 13 December 2006

Available online 19 January 2007

Editor: R.D. van der Hilst

Abstract

The kinematics and time-dependence of back-arc extension or compression is one of the most poorly understood aspects of plate tectonics, and has nearly exclusively been studied from snapshots of present-day observations. Here we combine absolute and relative plate motions with reconstructions of now subducted ocean floor to analyse subduction kinematics and upper plate strain from geological observations since 80 Ma along the 3200 km long Sunda-Java trench, one of the largest subduction systems on Earth. Combining plate motions and slab geometries enables us to reconstruct a time-dependent slab window beneath Sundaland, formed through Wharton spreading ridge subduction. We find that upper plate advance and retreat is the main influence on upper plate strain, but subduction of large bathymetric ridges, and slab-window effects, also play a significant, and at times dominant, role. Compression in the Sundaland back-arc region can be linked to advance of the upper plate. Extension of the Sundaland back-arc region correlates with two patterns of upper plate motion, (a) retreat of the upper plate, and (b) advance of the upper plate combined with more rapid advance of the Sundaland margin due to hinge rollback. Subduction of large bathymetric ridges causes compression in the upper plate, especially Wharton Ridge subduction underneath Sumatra over the period 15–0 Ma. Our reconstructions unravel the evolving geometry of a slab window underlying the Java–South Sumatra region, and we propose that decreased mantle wedge viscosities associated with this slab-window exacerbated Palaeogene extension in the Java Sea region via active rifting, and enabled Sumatran continental extension to continue at 50–35 Ma when upper plate advance would otherwise have led to compression.

© 2007 Published by Elsevier B.V.

Keywords: Sundaland; subduction; kinematics; slab window

1. Introduction

Numerous models have been proposed to account for the time-dependence of extension and back-arc basin formation in a subduction setting, including: (1) the

extrusion model, where back-arc formation is related to lateral absolute upper plate motion [1–3] (2) the sea-anchor model, where back-arc formation is related to the force generated by the down-going slab resisting lateral motion [2], (3) magmatic models, where back-arc formation is related to mantle flow in the wedge overlying the slab [4–6], and (4) the slab pull model, where back-arc formation is related to subduction hinge rollback caused by negative buoyancy of the subducting slab [7–9]. The “sea-anchor” model and the “extrusion”

* Corresponding author.

E-mail address: j.whittaker@geosci.usyd.edu.au (J.M. Whittaker).

model are the more likely models for back-arc formation according to analysis of recent mantle flow data from the Mariana subduction system [10]. Strain in the “back-arc” region of an upper plate in a subduction setting can range from strongly compressional to seafloor spreading. In order to examine relationships between various plate kinematics parameters and a range of upper plate strain regimes, we focus on the Sunda-Java subduction zone through the Cenozoic. Excluding Andaman Sea back-arc spreading from ~ 13 Ma to the present [11], the Sundaland margin has experienced compression, non-rift related subsidence, or crustal extension during the Cenozoic [12].

In both the “sea-anchor” model and the “extrusion” model a major parameter that influences upper plate strain is upper plate motion. Upper plate motions have long been associated with upper plate strain [1], with extensional back-arcs correlating with retreating upper plates, and compressional back-arcs correlating with advancing upper plates e.g. [2,13–15]. We have compared reconstructed absolute and trench-normal upper plate motions with strain regimes known to occur in the Sundaland margin to 60 Ma.

Recently, Lallemand and Heuret [13] observed a correlation between present-day shallow slab dip angles (0–125 km) and upper plate strain, with compressive and extensional regimes correlating to low and high shallow slab dips, respectively. Sdrolias and Müller [14] found that a combination of factors, including shallow slab dip (0–100 km), influences the initiation of back-arc spreading and that once initiated, back-arc spreading continues regardless of upper plate motion. Sdrolias and Müller [14], also observed a correlation between age of present-day, non-perturbed subducting lithosphere and shallow slab dip angle (0–100 km), where older subducting lithosphere correlates with steeper shallow slab dip angles and vice versa. We have utilised this relationship to reconstruct shallow slab dips for the Sunda-Java trench back to 80 Ma, using palaeo-age grids. We then compare the reconstructed shallow slab dips with mapped strain regimes through time along the Sundaland margin.

Complicating kinematics at the Sunda-Java trench has been the subduction of the active Wharton Ridge from ca. 70 Ma [16], to 43 Ma [17], and the remainder of the then extinct Wharton Ridge representing a bathymetric ridge from 43 Ma to the present. During subduction of an active ridge, a slab window may form under the upper plate [18,19]. A slab window develops when down-going plates continue diverging but trailing plate edges cease to grow and may even become hot and begin to melt [19]. The slab window widens as this process continues. Slab windows

occurring beneath the west coast of North America (e.g. [20–24]), Central America (e.g. [25]) and South America (e.g. [26,27]) have been well studied compared to the Indonesian subduction zone. The palaeo-positions of slab window are normally estimated using geological data from the overriding plate, such as changes in volcanism and tectonic events such as regional uplift. For the Sunda-Java trench we have used time-dependent plate motion vectors combined with reconstructed palaeo-age grids to compute the size and position of the slab window beneath the southern Sundaland margin.

2. Methods

In our study, we split the Sundaland margin into three regions; the Andaman Sea, Sumatra, and Java (see Fig. 1). For each region, we identified and summarized different periods of upper plate strain from Morley [28], Bishop [29], Hall [30], Letouzey et al. [12], Eguchi et al. [31], and Curray et al. [11] (see Fig. 3) and categorised each period based on the method of Jarrard [15].

We calculated shallow slab dip angles at each point along the Sundaland trench for 5 million year time stages from the present to 80 Ma, utilising the relationship $y=0.1961x+12.232$, where x is age of subducting lithosphere at the trench, and y is the shallow slab dip angle [14]. We obtained the age of the down-going lithosphere at the trench from revised versions of oceanic palaeo-age grids from Heine et al. [16]. From the calculated shallow slab dip angles, average shallow slab dip angles were computed for each region at all time stages. Averaging the slab dip angles minimizes any distortions in slab dip angle due to proximity to the edge of the subducting plate, which can be around 10° steeper close to slab edges [13].

For each stage we calculated absolute plate motion vectors for four plates; the Sundaland plate (80–0 Ma), the Sumatra-Java plate (or Sundaland margin) (80–0 Ma), the Indian plate (80–45 Ma), and the Australian plate (80–0 Ma) (see Fig. 1). Vectors were calculated at points every 500 km along the Sundaland trench, which was digitised for the present day then fixed to the Sumatra-Java plate for rotation back through time. Our plate reconstructions used the Heine et al. [16] and Gaina and Müller [32] plate kinematic models in a moving hotspot reference frame from O’Neill et al. [33]. Absolute plate motion vectors were used to calculate trench-normal vectors for each plate, which are useful for examining the overall compressional/extensional forces acting on the continental margin.

We reconstructed the position of the slab window beneath Sundaland, using the method of Thorkelson

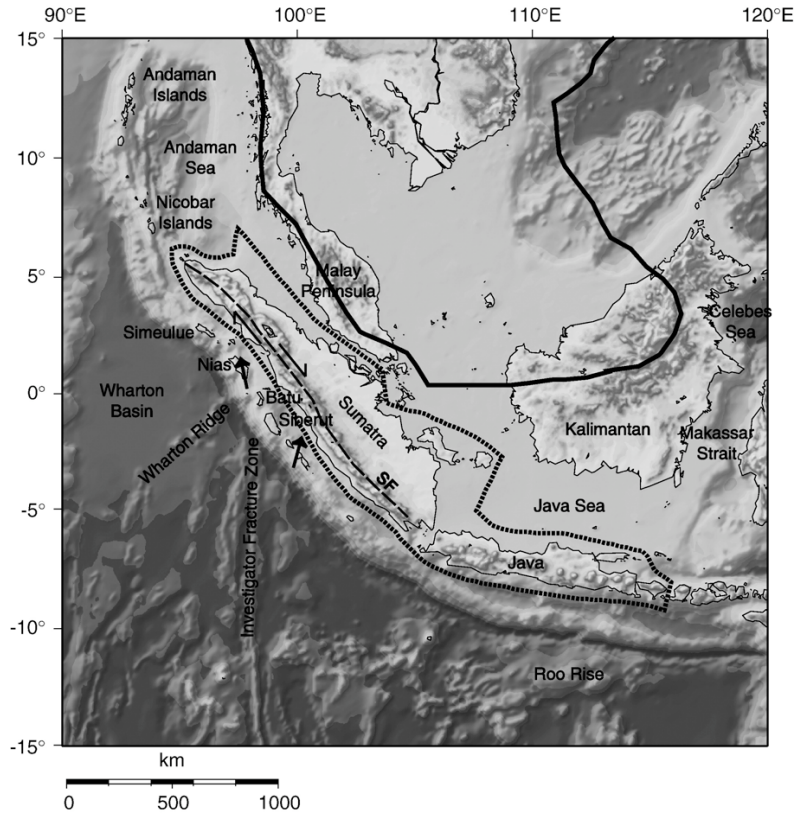


Fig. 1. Topographic and bathymetric map of SE Asia, SF — Sumatra Fault, boundaries of the Sundaland margin (dashed) and the Sundaland core (solid), small arrows depict motion of Sumatran fore-arc northwest and southeast of Batu Island from Prawirodirdjo et al. [48].

[18] which calculates the slab-window position using ridge-transform geometry and convergence vectors. Our absolute plate motion vectors were used to calculate convergence vectors, which were used in conjunction with the reconstructed location of the Wharton Ridge through time from the palaeo-age grids to establish the shape and size of the slab window. Vectors used to calculate the shape of the slab window are presented in velocity–space diagrams in Fig. 2 for time slices where there was an active triple junction at the Sundaland margin. Generally, the geometry of a slab window is affected by relative plate motions, pre-subduction ridge-transform fault geometry, subduction angles, thermal erosion, deformation caused by spherical shell stress and lateral and down-dip changes in the angle of slab dip [18]. In our approach, we have assumed, a horizontal subducted slab, no thermal erosion of the diverging plate edges, and no deformation from spherical shell stress. Due to these assumptions we have calculated a

minimum slab window, as adding the effects of a dipping slab and thermal erosion of plate edges would likely lead to a larger extent for the slab window. We have also limited the lateral extent of the slab window to 1000 km perpendicular to the trench because at this point the slab can be assumed to have reached the 660 km mantle discontinuity and the slab window would no longer have a discernable affect on the overriding plate.

3. Plate kinematics and overriding plate deformation

3.1. Plate motions

Fig. 2 illustrates that from 80 Ma to the cessation of Wharton Ridge spreading (~43 Ma [17]), the Australian Plate moved at a much slower rate than the Indian Plate (Fig. 2(i–vii)). Initial plate and margin geometry and kinematics of the India–Eurasia collision remains

controversial [34], but it is generally accepted that an India–Eurasia related collision slowed northward Indian Plate motion from 60–55 Ma (e.g. [34–36]). Fig. 2(i–viii) shows the Indian Plate moving rapidly from 80 Ma until absolute plate motions dropped from an average of 120 mm/yr at 60–65 Ma to 81 mm/yr by 45–50 and 26 mm/yr by 40–45 Ma. Indian plate motion increases from the low at 40–45 Ma to an average of 69 mm/yr at 30–35 Ma decreasing to 63 mm/yr at 15–20 Ma.

An advancing upper plate is expected to cause compression in the upper plate margin. Our reconstructions show two different types of advancing upper plate motion. The first type, where both the upper margin and upper core advance at the same rate, we call ‘uniform upper plate motion’. Uniform upper plate motion occurs for Java from 15 Ma to the present (Fig. 3(viii–x)), which corresponds with compression that is known to have affected Java from ~15 Ma to the present day. This type of upper plate advance also occurs at all points along the Sunda–Java trench from 80 Ma to ~60 Ma, so it is possible that the entire Sunda–Java margin was affected by compression during the period 80–60 Ma. However, the presence of an underlying slab window due to the subduction of the then active Wharton Ridge from 70 Ma may have had an effect on the southeastern portion of the margin.

The second, where reconstructions show the upper margin advancing more rapidly than the upper core, we call ‘differential upper plate motion’. Differential upper plate motion occurs for the Andaman Sea at 30–15 Ma (Fig. 3(i–iii)), Sumatra, strongly at 30–15 Ma (Fig. 3(iv–vii)), southern Sumatra, weakly at 50–30 Ma (Fig. 3(vi–vii)), and Java at 45–15 Ma (Fig. 3(viii–x)). The upper margin is known to have experienced extension during all of these periods, which is expected to occur on the upper plate as the margin draws away from the core. Subduction hinge rollback, where the retreating hinge draws the margin away from the core, is the most likely explanation for this pattern of upper plate behaviour. Subduction hinge-roll has previously been suggested as the major mechanism causing Malay–Thai basin extension at 30–15 Ma [28]. Non-rift

related subsidence, observed in Java and Sumatra from 15–20 Ma can be explained as the period of change over from extension to compression.

The increase in rate of advance of the Sundaland core at 30–20 Ma at almost all reconstructed locations shown in Fig. 2 is likely to be a product of extrusion caused by India–Eurasia collision. Southeasterly extrusion of Sundaland from 40 Ma caused by the India–Eurasia collision are supported by mantle tomography images showing a change in present-day slab structure at 700 and 1100 km depth [37,38]. ‘Hard’ collision between India and Eurasia is thought to have caused the slow-down in northward Indian motion at 30–20 Ma [39–41]. Morley [28] shows that more southerly blocks of Southeast Asia were “squeezed out faster than their more northerly neighbours”. This pattern fits increased rates of upper plate advance observed at ~50 Ma and 30–20 Ma (Fig. 3), which subside following the initial extrusion related increase.

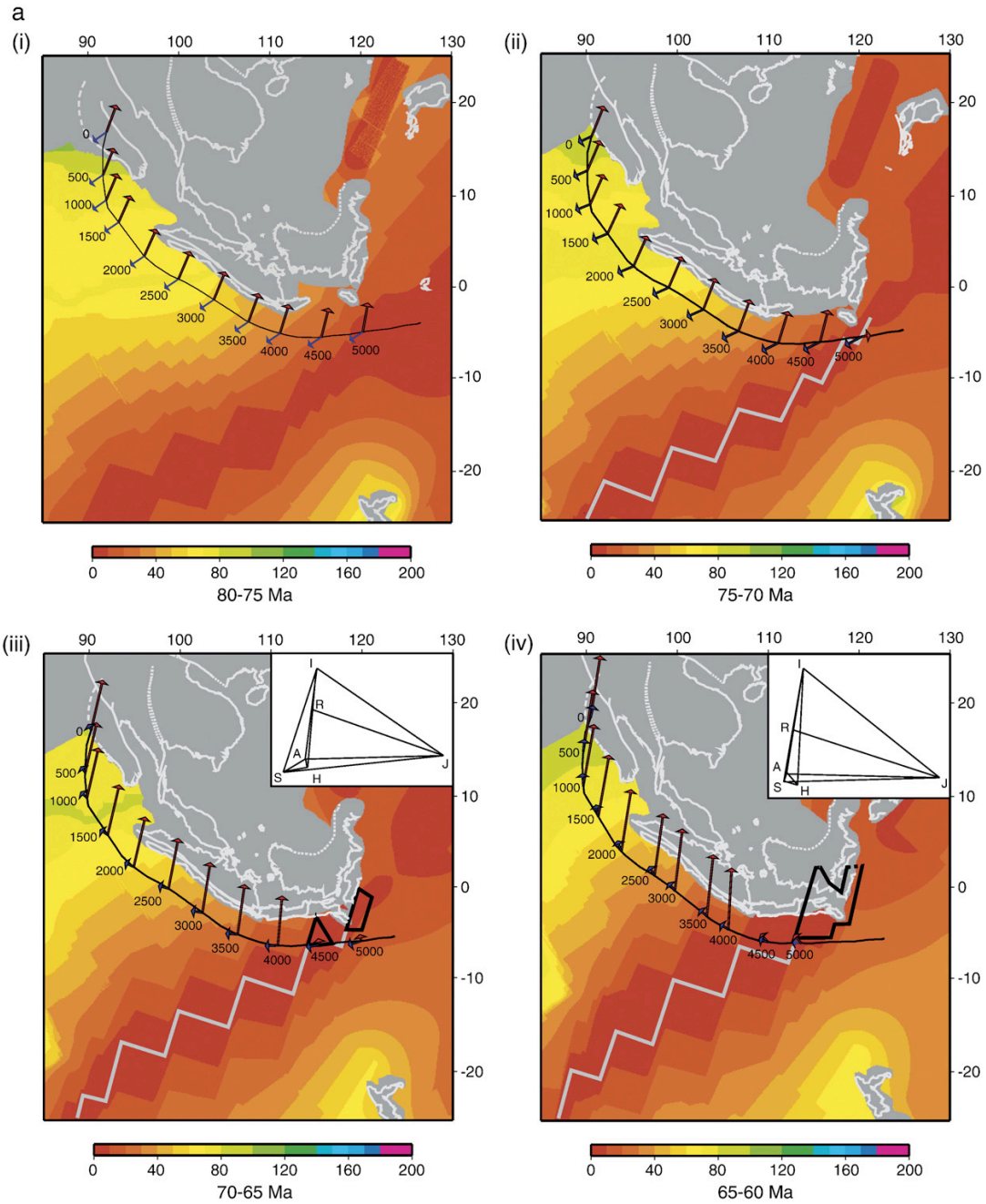
Our reconstructions (Fig. 3(i–iii)) show retreat of the Andaman Sea upper plate at 15–0 Ma. This correlates with Andaman Sea back-arc spreading that has occurred from ~13 Ma [11]. This correlation has previously been observed by Sdrolias and Müller [14], who also found that once initiated back-arc spreading is not affected by motion of the upper plate and noted that it is believed that spreading in this location is controlled by India–Eurasia related extrusion tectonics.

Figs. 2(v–vi) and 3 show a reversal in Sundaland core motion, from retreating at 55 Ma to advancing by ~47 Ma. This change in motion is a consequence of extrusion tectonics caused by the India collision. Upper plate retreat occurs at all points along the Sunda–Java trench except the northern Andaman Sea at 60–50 Ma (Fig. 3). In the Java region this corresponds with a known period of extension. Retreating upper plates have long been associated with extension in back-arc areas [2,13–15]. To initiate, back-arc spreading requires not only a retreating upper plate but age of down-going lithosphere at the trench >55 Myr, and a shallow slab

Fig. 2. Reconstructed absolute plate motions of the overlying Sundaland plate, and the down-going Indo–Australian plate from 80 Ma to the present. Arrows represent stage (5 Myr) motions of the Sundaland margin (blue arrows), and Indian (Australian) plate (red arrows), and correspond to; (i) 80–75 Ma (ii) 75–70 Ma (iii) 70–65 Ma (iv) 65–60 Ma (v) 60–55 Ma (vi) 55–50 Ma (vii) 50–45 Ma (viii) 45–40 Ma (ix) 40–35 Ma (x) 35–30 Ma (xi) 30–25 Ma (xii) 25–20 Ma (xiii) 20–15 Ma (xiv) 15–10 Ma (xv) 10–5 Ma, and (xvi) 5–0 Ma. Tectonic regimes shown by compressional (black centred ‘beachball’), extensional (white centred ‘beachball’) and subsidence (denoted by ‘sub.’) symbols (symbols are not oriented, symbolic only) for the Java, south Sumatra and Andaman Sea regions where information was available from the literature [12,29–31]. The location of the mid-ocean ridge and velocity–space diagrams (upper right of each figure) are shown for time slices when there was an active triple junction at the Sundaland Trench, and hence a growing slab window. In the velocity–space diagrams; I — Indian Plate; R — Ridge; S — Sundaland Plate; A — Australian Plate; H — hotspot; J — previous ridge–trench intersection location. The reconstructed positions of the slab window due to the subduction of the Wharton Ridge (active until 43 Ma) are shown by thick black lines, dashed sections where slab window cut off at distance 1000 km from the trench. Thin black line represents our Sunda–Java trench location.

dip $> 30^\circ$ [14]. Fig. 2(v–vi) shows that from 60–50 Ma, the age of subducting lithosphere at the trench was < 55 Myr at all points on the trench southeast of point 1500, which is insufficient to initiate back-arc spreading

at this time. Therefore, we predict that crustal extension affected the southeastern Sundaland back-arc east of point 1500 for the period 60–50 Ma. For the southern Andaman Sea section of the trench (points 1000–1500)



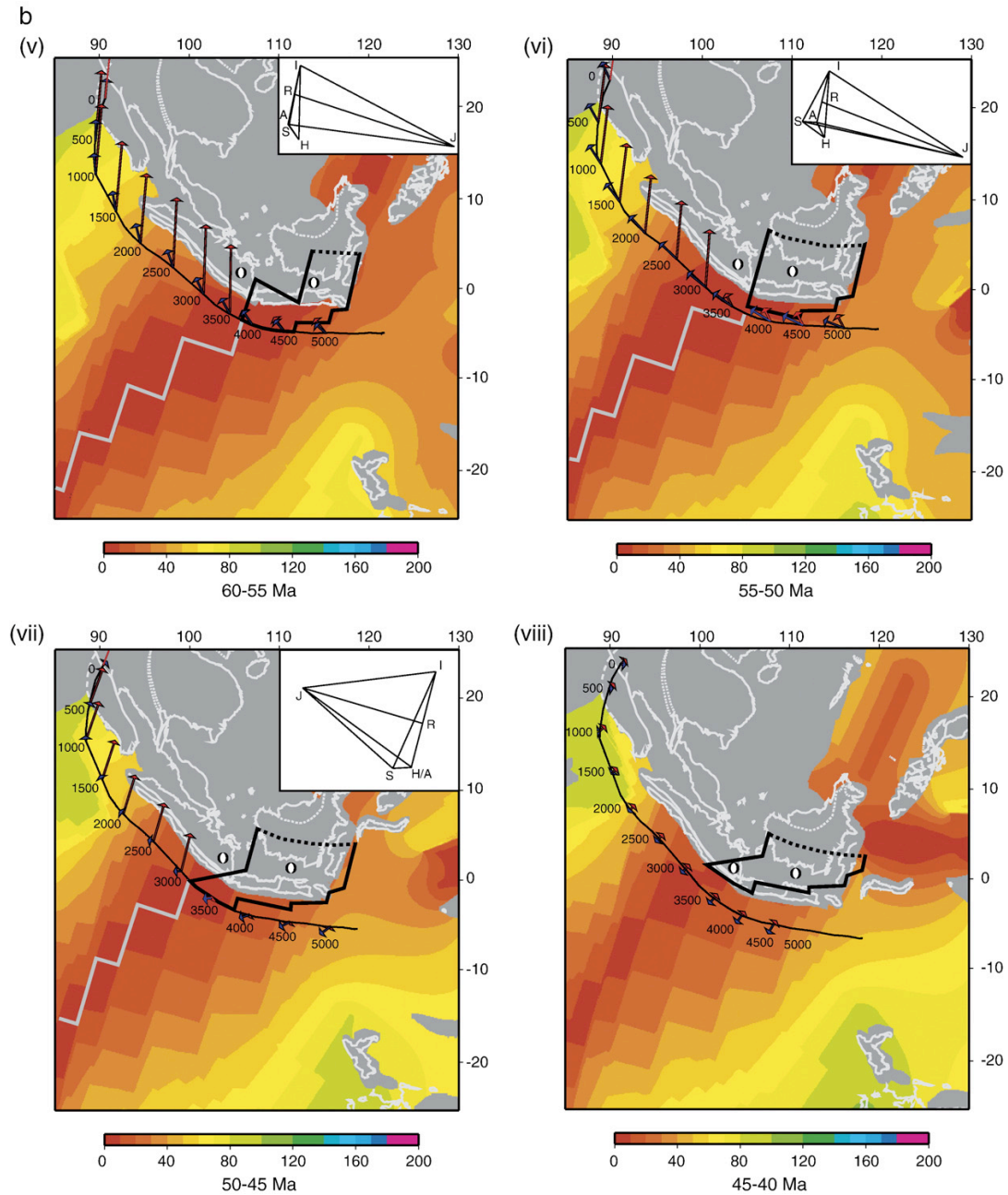


Fig. 2 (continued).

Fig. 2(v–vi)) the age of subducting lithosphere at the trench was >55 Myr, and Fig. 3(ii–iii) shows upper plate retreat. However, our reconstructed slab dip for the Andaman Sea for 60–50 Ma is $\sim 22^\circ$, suggesting that

conditions were not conducive to back-arc spreading initiation in the Andaman region at this time.

Central and northern Sumatran upper plate retreat suggests that the Sumatra back-arc should have

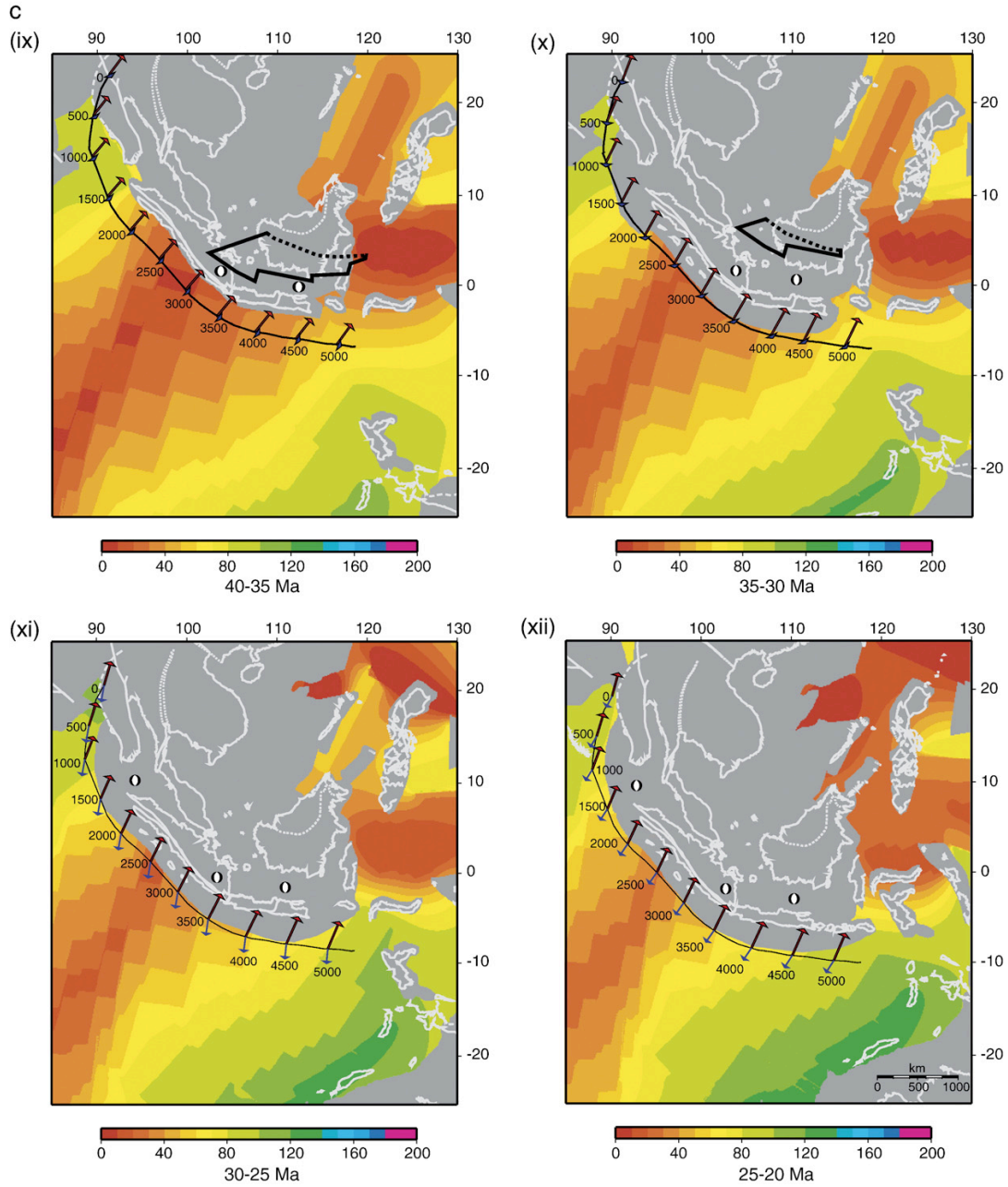


Fig. 2 (continued).

experienced extension from 15 Ma to the present (Fig. 3 (iv–vii)). However, compression is known to have affected this area during this period. It is likely that the

presence of the subducting Wharton Ridge and Investigator Fracture Zone (IFZ) are responsible for this deviation from the expected upper plate regime.

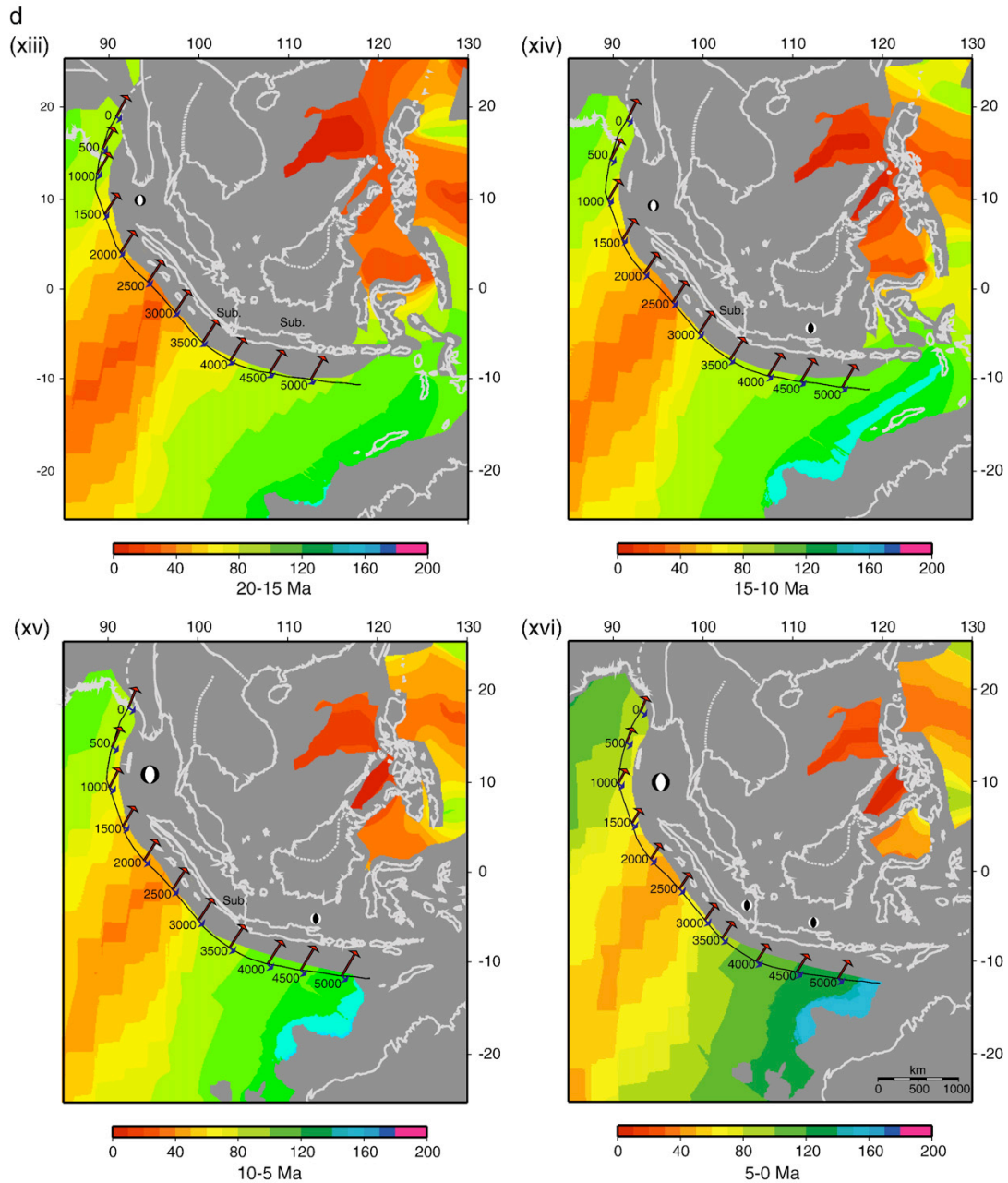


Fig. 2 (continued).

3.2. Bathymetric ridge subduction

The Wharton Ridge first subducts beneath eastern Java [16], at 70 Ma, which likely caused the Sundaland margin

to rotate clockwise about a rotation pole close to the area at this time. Presently, the Wharton Ridge and Investigator Fracture Zone IFZ subduct beneath northern–central Sumatra (Fig. 1). The subduction of bathymetric features

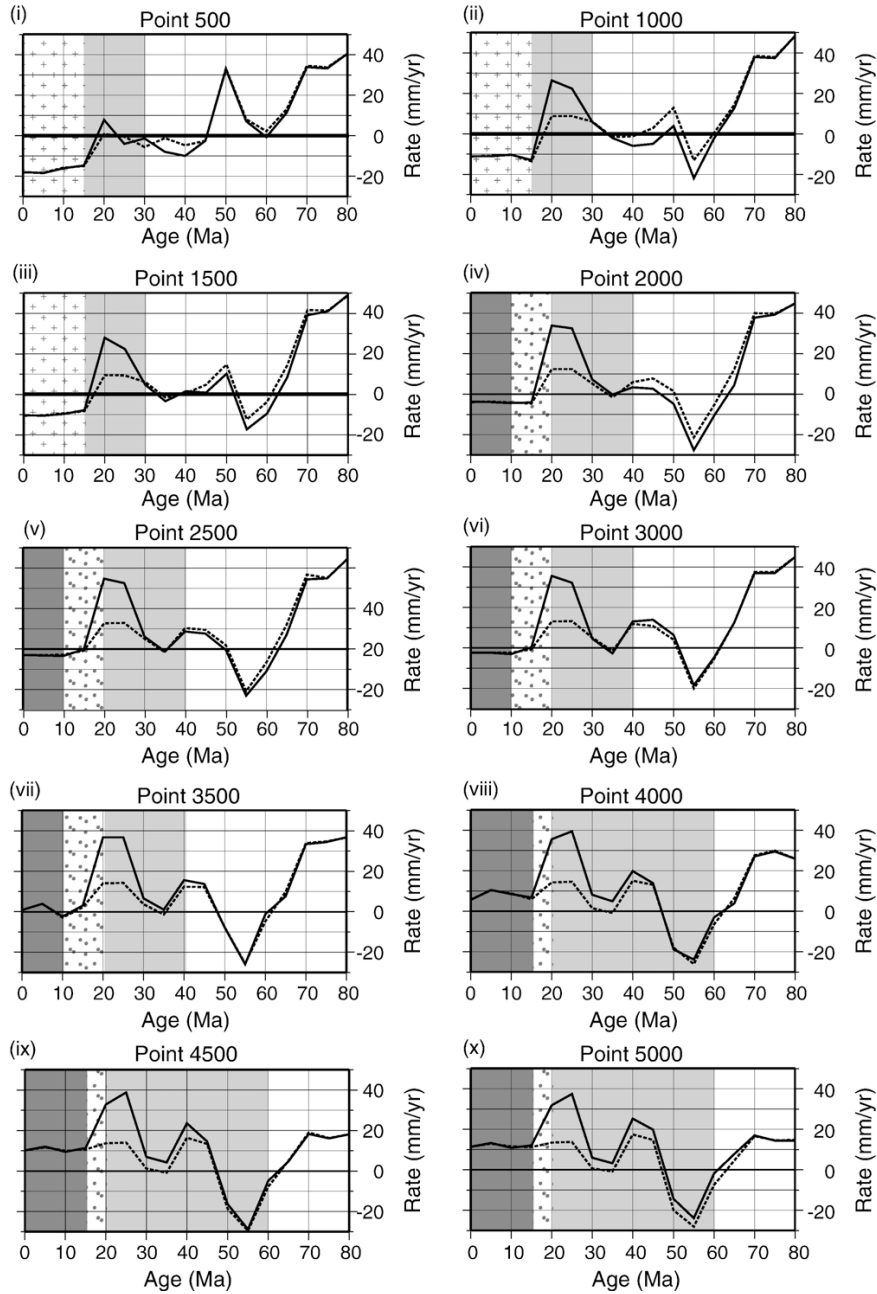


Fig. 3. Trench-normal component of the reconstructed absolute plate velocity plotted for the Sundaland core and margin for the period 0–80 Ma at points every 500 km along the Sunda-Java trench (see Fig. 2). Positive values indicate advance (oceanward motion) and negative values indicate retreat (landward motion) of the upper plates. Background shading represents known tectonic regimes for the Sundaland back-arc summarised from Morley [28], Bishop [29], Hall [30], Letouzey et al. [12], Eguchi et al. [31], and Curray et al. [11], where (1) compression is represented by crosses, (2) subsidence is represented by dots, (3) extension is represented by light shading, and (4) spreading is represented by dark shading.

is widely accepted to cause broadly distributed deformation in the fore-arc [42,43]. Geodetic strain and rotation rates show that the northern Sumatran region currently endures a highly compressive regime [44]. Rates of seismic deformation are at a maximum offshore Sumatra near Nias Island (5.2 ± 0.65 mm/yr) and progressively decrease northward (1.12 ± 0.13 mm/yr) [45]. Due to oblique subduction and extension to the north, Sumatra, and the Sumatran fore-arc, are divided into a series of NW–SE striking slices that move towards the northwest, separated by right-lateral faults [46]. Most displacement on these faults occurs in northwest Sumatra and dissipates towards the southeast [47]. Geodetic observations from GPS data [48] reveal an interesting change in Sumatran fore-arc motion centred around Batu Island (Fig. 1). Southeast of Batu Island, the Sumatra fore-arc moves northeast, roughly parallel with the motion of the Indian plate, while northwest of Batu Island the Sumatran fore-arc moves to the northwest [48]. This change in fore-arc motion has been ascribed to decoupling between the northern fore-arc and mantle wedge due to increased pore pressures in the fore-arc thrust fault due to subduction of thick Nicobar fan sediments [48].

The Wharton Ridge subducts beneath Nias Island where seismic deformation is highest and the IFZ subducts directly beneath Batu Island where the Sumatran fore-arc begins to move in a northwest direction. Thus, subduction of the Wharton Ridge and IFZ is another mechanism causing the high seismic deformation rates, change in fore-arc motion, and concentration of strike-slip motion that occurs in northern Sumatra. Fig. 3(iv–vii) shows that rate of Sumatran upper plate retreat at 15–0 Ma is not rapid (0–5 mm/yr), so it is likely that extension experienced by the Sumatra back-arc from this mechanism is relatively small. It is possible that present-day compression from subduction of the Wharton Ridge and Investigator Fracture Zone dominates over extension resulting from the retreating upper plate. It is likely that this domination of compressive strain related to bathymetric ridge subduction has dominated over upper plate motion related extension since 15 Ma.

Subduction of the Wharton Ridge initiated at ~70 Ma ([16], (see Fig. 2(ii))) and has migrated ~2400 km (30 km/Ma) along the Sunda-Java trench to its present-day location. During the period 50–15 Ma, the upper plate adjacent to the location of Wharton Ridge subduction is both observed and predicted (using upper plate motions) to have experienced extension. Plate motions were generally stronger at this time compared with those affecting Sumatra over the past 15 Myr and so dominated over the compressional effects of the subducting Wharton Ridge.

The Roo Rise (Fig. 1) is presently being subducting adjacent to Java. Subduction of this major bathymetric feature is currently causing deforming the Javanese fore-arc [49]. Roo Rise subduction is likely to be contributing to Javanese compression in addition to compression caused by upper plate advance since ~15 Ma. Onset of Roo Rise subduction is unknown so the period over which it has influenced Javanese upper plate strain is unknown.

3.3. Slab window

A slab window may form between the diverging plates of a subducting active mid-ocean ridge. Due to the hotter mantle wedge temperatures expected in conjunction with a slab window, the viscosity may be decreased in the mantle wedge and a low viscosity mantle wedge can lead to horizontal extension in normal subduction zones [18,24,50,51]. Our reconstructions show that a slab window was underlying southern/central Sumatra at 45–35 Ma (Fig. 2). Our reconstructions show a minimum slab-window extent as the effects of slab dip and thermal erosion of plate edges are excluded, both of which result in increasing the lateral extent of the slab window. Fig. 2(v–vii) shows the western edge of the slab window in a stationary position at the southern tip of Sumatra from 60–45 Ma. It is likely that thermal erosion of the Indian plate edge over this 15 million year period would have progressively shifted the slab-window edge across southern Sumatra earlier than 45–40 Ma shown in Fig. 2(vii–viii). Plate motion reconstructions from 50 Ma (Fig. 3) show an advancing upper plate in Sumatra suggesting that a compressive regime should have existed, however extension is observed from geological evidence. The underlying slab window may have enabled extension to continue from ~50 Ma until the onset of subduction hinge rollback at 35 Ma.

An underlying slab window can also lead to cessation of arc volcanism [18], while the progression of a slab edge across a region can change chemical signatures, increase volume and extend the range of volcanism [18]. Plutonism occurred in Indonesia from 60 Ma but was restricted to Sumatra (and further inland from the trench) and ceased at around 50 Ma [30,52]. In general, this Palaeogene volcanic activity was much more prominent in south and central Sumatra than northern Sumatra [30] and it has previously been noted that this pattern of volcanism may be related to subduction of the Wharton Ridge [16]. It is possible that this underlying slab window was responsible for the burst of volcanic activity in south and central Sumatra from 60 to 50 Ma as thermal erosion

caused progression of the Indian plate edge across southern Sumatra. Cessation of volcanism at ~ 50 Ma suggests that the slab window was established beneath southern Sumatra causing volcanic activity to halt. Subduction related plutonism, focussed along the Sumatran Fault Zone from the Mid-Miocene [52], re-established in Sumatra at around 30 Ma, when that the slab window was no longer positioned beneath this region.

The slab window underlies Java at 70–40 Ma (Fig. 2 (iii–viii)). At 60–45 Ma extension occurred across southern Kalimantan and the Java Sea, as well as some spreading in the Makassar Straits [12,53,54]. Extension caused by the presence of the underlying slab window may have exacerbated Javanese back-arc extension, already induced by a retreating upper plate, enabling spreading to occur in the Makassar Strait. It is also possible that the underlying slab window was responsible for inhibited Javanese volcanism prior to ~ 42 Ma [55].

3.4. Shallow slab dip angle

Fig. 4 shows our reconstructed shallow slab dips (SSD) plotted against upper plate strain obtained from the literature for the Indonesian margin. Computed SSD in the ‘slightly extensional’ category, that fall outside the present-day relationship of Lallemand and Heuret [13], represent subduction of young (<23 Ma) lithosphere. Mid-ocean ridge subduction was excluded from the studies of Lallemand and Heuret [13] and Sdrolias and Müller [14]. Fig. 4 shows that, if these values are excluded, our reconstructed regional SSD fall within the pattern observed for the present day by Lallemand and Heuret [13].

Observed SSD (0–125 km) for the Andaman, Sumatra and Java regions are 24.6° , 23.9° , and 22.7° , respectively [56], while our calculated SSD are 29° , 25.5° , and 36° ,

respectively. The deviation between observed and calculated clearly shows that the age of subducting lithosphere alone cannot be used to reconstruct shallow slab dips, and that further parameters need to be incorporated into the calculations, such as horizontal and vertical mantle flow, and down-going plate motions. Therefore, due to errors in the estimation of SSD from the age of subducting lithosphere, as well as the broad nature of the relationship between upper plate strain and SSD it is not possible to use the age of subducting lithosphere to predict palaeo-upper plate strain regimes.

4. Conclusions

Upper plate strain expected for Sundaland back-arc regions from reconstructed trench-normal plate motions of the Sundaland core and margin correlate well with known upper plate strain regimes. The three types of upper plate motion to affect the Sundaland margin since 80 Ma are:

- (1) A consistently advancing upper plate corresponds to compression in the overriding back-arc, caused by the collision between the down-going Indian plate and the advancing Sundaland plate,
- (2) An advancing upper plate, where the Sundaland margin advances more rapidly than the Sundaland core, correlates with extension in the upper plate e.g. southern Andaman Sea, Sumatra and Java at 30–15 Ma, 35–15, and 45–15 Ma, respectively. The only mechanism for the margin to advance faster than the core is pulling by subduction hinge rollback,
- (3) Uniform upper plate retreat correlates with extension in the upper plate in two cases, Javanese crustal extension 60–50 Ma, and spreading in the Andaman Sea 15–0 Ma.

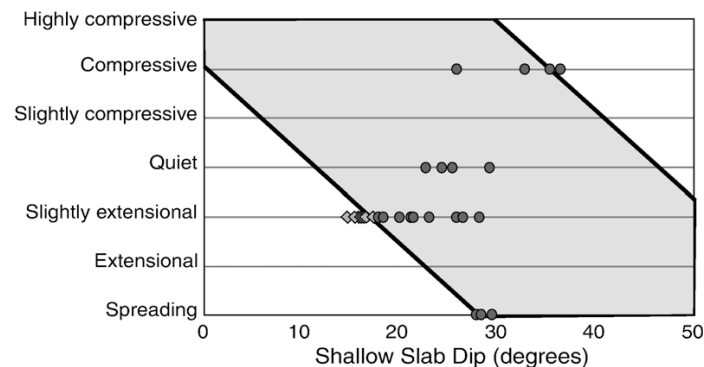


Fig. 4. This figure shows our shallow slab dip angles plotted against back-arc tectonic regime [11,12,28–31]. The black lines indicate the envelope of the present-day relationship for worldwide subduction zones from Lallemand et al. [13]. Light grey diamonds represent shallow slab dips for which the age of subducting lithosphere is <23 Ma. Dark grey circles are all other data points.

Periods where predicted upper plate strain from upper plate motions does not match observed upper plate strain can be explained by forces arising from the slab window and subduction of large bathymetric ridges. In present-day Java, compression is enhanced by subduction of the Roo Rise, while in Sumatra, 15–0 Ma, compression from Wharton Ridge and IFZ subduction overrides induced extension forces from upper plate retreat. The underlying slab window, formed through subduction of the Wharton Ridge, may have exacerbated extension in the Java Sea and south Kalimantan region and possible seafloor spreading in the Makassar Strait at ~60–45 Ma. The slab window may also have enabled extension to continue in Sumatra from ~50 Ma until the onset of subduction hinge rollback at 35 Ma when a uniformly advancing upper plate could have otherwise led to a compressive regime. The progression of the slab window across Java and southern Sumatra also appears to have some correlation with Indonesian volcanic activity with the presence of the underlying slab window corresponding with an absence of Javanese volcanism until ~42 Ma [55], and the progressing edge of the slab window corresponding with an episode of volcanism from 60–50 Ma in southern Sumatra.

The relationship between our reconstructed shallow slab dips and known Sundaland upper plate strain regimes falls within the envelope of observed slab dips for the present day. However, due to the errors associated with calculating shallow slab dips from age of subducting lithosphere, and the broad nature of the relationship between present-day dips and upper plate strain, our reconstructed shallow slab dips are not useful for predicting palaeo-upper plate strain regimes.

References

- [1] C.G. Chase, Extension behind island arcs and motions relative to hot spots, *J. Geophys. Res.* 83 (1978) 5380–5387.
- [2] C.H. Scholz, J. Campos, On the mechanism of seismic decoupling and back arc spreading at subduction zones, *J. Geophys. Res.* 100 (1995) 22,103–22,122.
- [3] E. Mandovani, D. Albarello, D. Babbucci, C. Tamburelli, M. Viti, Genetic mechanism of back-arc opening: insights from the Mediterranean deformation pattern, in: E. Boschi, E. Ekstrom, A. Morelli (Eds.), *Problems in Geophysics for the New Millennium*, Editrice Compositori, Bologna, 2000, pp. 611–643.
- [4] M.V. Rodkin, A.G. Rodnikov, Origin and structure of back-arc basins: new data and model discussion, *Phys. Earth Planet. Inter.* 93 (1996) 123–131.
- [5] D.E. Karig, Origin and development of marginal basins in the western pacific, *J. Geophys. Res.* 76 (1971) 2542.
- [6] N.H. Sleep, M.N. Toksoz, Evolution of marginal seas, *Nature* 233 (1971) 548–550.
- [7] W.M. Elsasser, Seafloor spreading as thermal convection, *J. Geophys. Res.* 76 (1971) 1101–1112.
- [8] P. Molnar, T. Atwater, Interarc spreading and Cordilleran tectonics as alternatives related to the age of subducted oceanic lithosphere, *Earth Planet. Sci. Lett.* 41 (1978) 330–340.
- [9] J.F. Dewey, Episodicity, sequence, and style at convergent plate boundaries, in: D.W. Strangway (Ed.), *The Continental Crust and Its Mineral Deposits Special Paper*, vol. 20, The Geological Association of Canada, Toronto, 1980, pp. 553–573.
- [10] T. Volti, A. Gorbato, H. Shiobara, H. Sugioka, K. Mochizuki, Y. Kaneda, Shear-wave splitting in the Mariana trough—a relation between back-arc spreading and mantle flow? *Earth Planet. Sci. Lett.* 244 (2006) 566–575.
- [11] J.R. Curran, D.G. Moore, L.A. Lawver, F.J. Emmel, R.W. Raitt, M. Henry, R. Kieckhefer, Tectonics of the Andaman Sea and Burma, *Geological and Geophysical Investigations Of Continental Margins*, vol. 29, AAPG Memoir, 1978, pp. 189–198.
- [12] J. Letouzey, P. Werner, A. Marty, Fault reactivation and structural inversion. Backarc and intraplate compressive deformations. Example of the eastern Sunda shelf (Indonesia), *Tectonophysics* 183 (1990) 341–362.
- [13] S. Lallemand, A. Heuret, On the relationships between slab dip, back-arc stress, upper plate absolute motion, and crustal nature in subduction zones, *Geochem., Geophys., Geosyst.* 6 (2005), doi:10.1029/2005GC000917.
- [14] M. Sdrolias, R.D. Müller, The controls on back-arc basin formation, *Geochem., Geophys., Geosyst.* 7 (2006) Q04016, doi:10.1029/2005GC001090.
- [15] R.D. Jarrard, Relations among subduction parameters, *Rev. Geophys.* 24 (1986) 217–284.
- [16] C. Heine, R.D. Müller, C. Gaina, Reconstructing the lost Eastern Tethys Ocean Basin: constraints for the convergence history of the SE Asian margin and marine gateways, in: P. Clift, D. Hayes, W. Kuhnt, P. Wang (Eds.), *Continent-Ocean Interactions in Southeast Asia*, *Geophys. Monogr. Ser.*, vol. 1149, American Geophysical Union, Washington, 2004.
- [17] K.S. Krishna, D. Gopala Rao, M.V. Ramana, V. Subrahmanyam, K. Sarma, A.I. Pilipenko, V.S. Shcherbakov, I.V. Radhakrishna Murthy, Tectonic model for the evolution of oceanic crust in the northeastern Indian Ocean from the Late Cretaceous to the early Tertiary, *J. Geophys. Res.* 100 (1995) 20011–20024.
- [18] D.J. Thorkelson, Subduction of diverging plates and the principles of slab window formation, *Tectonophysics* 255 (1996) 47–63.
- [19] W.R. Dickinson, W.S. Snyder, Geometry of subducted slabs related to San Andreas transform, *J. Geol.* 87 (1979) 609–627.
- [20] T. Atwater, J. Severinghaus, Relative plate motions in Northeast Pacific, 85 Ma to present, as recorded by magnetic lineation patterns, in: Anonymous (Ed.), *28th International Geological Congress. International Geological Congress, Abstracts—Congres Geologique Internationale, Resumes*, vol. 28; 1, International Geological Congress, 1989, pp. 60–61, [location varies], International.
- [21] R.G. Bohannon, T. Parsons, Tectonic implications of post-30 Ma Pacific and north American relative plate motions, *Geol. Soc. Amer. Bull.* 107 (1995) 937–959.
- [22] D.J. Thorkelson, R.P. Taylor, Cordilleran slab windows, *Geology* 17 (1989) 833–836.
- [23] J.K. Madsen, D.J. Thorkelson, R.M. Friedman, D.D. Marshall, Cenozoic to recent plate configurations in the Pacific basin: ridge subduction and slab window magmatism in western North America, *Geosphere* 2 (2006) 11–34.
- [24] V.B. Sisson, A.R. Poole, N.R. Harris, H.C. Burner, T.L. Pavlis, P. Copeland, R.A. Donelick, W.C. McLelland, Geochemical and

- geochronologic constraints for genesis of a tonalite–trondhjemite suite and associated mafic intrusive rocks in the eastern Chugach Mountains, Alaska; a record of ridge-transform subduction, *Spec. Pap. — Geol. Soc. Am.* 371 (2003) 293–326.
- [25] S.T. Johnston, D.J. Thorkelson, Cocos–Nazca slab window beneath Central America, *Earth Planet. Sci. Lett.* 146 (1997) 465–474.
- [26] V. Ramos, Seismic ridge subduction and topography: foreland deformation in the Patagonian Andes, *Tectonophysics* 399 (2005) 73–86.
- [27] C. Guivel, Y. Lagabrielle, J. Bourgois, H. Martin, N. Arnaud, S. Fourcade, J. Cotten, R. Maury, Very shallow melting of oceanic crust during spreading ridge subduction: origin of near-trench Quaternary volcanism at the Chile Triple Junction, *J. Geophys. Res.* 108 (2003), doi:10.1029/2002JB002119.
- [28] C.K. Morley, Combined escape tectonics and subduction roll-back arc extension: a model for the evolution of Tertiary rift basins in Thailand, Malaysia and Laos, *J. Geol. Soc. (Lond.)* 158 (2001) 461–474.
- [29] M.G. Bishop, South Sumatra Basin Province, Indonesia: the Lahat/Talang Akar–Cenozoic total petroleum system, Open-File Report 99–50 S, U. S. Department of the Interior U.S. Geological Survey, 2000.
- [30] R. Hall, Cenozoic geological and plate tectonic evolution of Southeast Asia and the SW Pacific: computer-based reconstructions, models and animations, *J. Asian Earth Sci.* 20 (2002) 353–431.
- [31] T. Eguchi, S. Uyeda, T. Maki, Seismotectonics and tectonic history of the Andaman Sea, *Tectonophysics* 57 (1979) 35–51.
- [32] C. Gaina, R.D. Müller, Cenozoic tectonic and depth/age evolution of the Indonesian gateway and associated back-arc basins, *Earth-Sci. Rev.* (submitted for publication).
- [33] C. O’Neill, R.D. Müller, B. Steinberger, On the uncertainties in hotspot reconstructions, and the significance of moving hotspot reference frames, *Geochem., Geophys., Geosyst.* 6 (2005) 002005, doi:10.1029/2004GC000784.
- [34] A.V. Abrajvitch, J.R. Ali, J.C. Aitchison, A.M. Badengzhu, Davis, J. Liu, S.V. Ziabrev, Neotethys and the India–Asia collision: insights from a palaeomagnetic study of the Dazhuqu ophiolite, southern Tibet, *Earth Planet. Sci. Lett.* 233 (2005) 87–102.
- [35] T.-Y. Lee, L.A. Lawver, Cenozoic plate reconstruction of Southeast Asia, *Tectonophysics* 251 (1995) 85–138.
- [36] G.D. Acton, Apparent polar wander of India since the Cretaceous with implications for regional tectonics and true polar wander, in: T. Radhakrishna, J.D.A. Piper (Eds.), *Indian Subcontinent and Gondwana: A Palaeomagnetic and Rock Magnetic Perspective* 44, *Mem. Geol. Soc. India*, 1999, pp. 129–175.
- [37] S. Widiyantoro, R. van der Hilst, Structure and evolution of lithospheric slab beneath the Sunda Arc, Indonesia, *Science* 271 (1996) 1566–1570.
- [38] A. Replumaz, H. Karason, R.D.v.d. Hilst, J. Besse, P. Tapponnier, 4-D evolution of SE Asia’s mantle from geological reconstructions and seismic tomography, *Earth Planet. Sci. Lett.* 221 (2004) 103–115.
- [39] R.G. Gordon, C. Demets, J.Y. Royer, Evidence for long-term diffuse deformation of the lithosphere of the equatorial Indian Ocean, *Nature* 395 (1998) 370–374.
- [40] P. Patriat, J. Achache, India–Eurasia collision chronology has implications for crustal shortening and driving mechanisms of plates, *Nature* 311 (1984) 615–621.
- [41] P. Patriat, J. Segoufin, Reconstruction of the Central Indian Ocean, *Tectonophysics* 155 (1988) 211–234.
- [42] T.W. Gardner, D. Verdonck, N. Pinter, R.L. Slingerland, K.P. Furlong, T.F. Bullard, S.G. Wells, Quaternary uplift astride the aseismic Cocos Ridge, pacific coast of Costa Rica, *Geol. Soc. Amer. Bull.* 104 (1992) 219–232.
- [43] W.-Y. Chung, H. Kanamori, A mechanical model for plate deformation associated with aseismic ridge subduction in the New Hebrides arc, *Tectonophysics* 50 (1978) 29–40.
- [44] G.W. Michel, Y. Yue Qui, Z. Sheng Yuan, C. Reigber, M. Becker, E. Reinhard, W. Simons, B. Ambrosius, C. Vigny, N. Chamot-Rooke, X. Le Pichon, P. Morgan, S. Matheussen, Crustal motion and block behaviour in SE-Asia from GPS measurements, *Earth Planet. Sci. Lett.* 187 (2001) 239–244.
- [45] M.R. Krishna, T.D. Sanu, Shallow seismicity, stress distribution and crustal deformation pattern in the Andaman–West Sunda arc and Andaman Sea, northeastern Indian Ocean, *J. Seismol.* 6 (2002) 25–41.
- [46] M. Diament, H. Harjono, K. Karta, C. Deplus, D. Dahrin, M.T. Zen, M. Gerard, O. Lassal, A. Martin, J. Malod, The Mentawai fault zone off Sumatra: a new key for the geodynamics of Western Indonesia, *Geology* 20 (1992) 259–262.
- [47] R. McCaffrey, Slip partitioning at convergent plate boundaries of SE Asia, in: R. Hall, D. Blundell (Eds.), *Geological Society Special Publication, Tectonic Evolution of Southeast Asia*, vol. 106, 1996, pp. 3–18.
- [48] L. Prawirodirdjo, Y. Bock, R. McCaffrey, J.F. Genrich, E. Calais, C. Stevens, S.S.O. Puntodewo, C. Subarya, J. Rais, P. Zwick, Fauzi, geodetic observations of interseismic strain segmentation at the Sumatra zone, *Geophys. Res. Lett.* 24 (1997) 2601–2604.
- [49] H. Kopp, E.R. Flueh, C.J. Petersen, W. Weinrebe, A. Wittwer, Meramex Scientists, The java margin revisited: evidence for subduction erosion off java, *Earth Planet. Sci. Lett.* 242 (1–2) (2006) 130–142.
- [50] M.I. Billen, M. Gurnis, A low viscosity wedge in subduction zones, *Earth Planet. Sci. Lett.* 193 (2001) 227–236.
- [51] D.J. Thorkelson, K. Breitsprecher, Partial melting of slab window margins: genesis of adakitic and non-adakitic magmas, *Lithos* 79 (2005) 25–41.
- [52] W.J. McCourt, M.J. Crow, E.J. Cobbing, T. Amin, Mesozoic and Cenozoic plutonic evolution of SE Asia: evidence from Sumatra, Indonesia, in: R. Hall, D. Blundell (Eds.), *Tectonic Evolution of Southeast Asia*, *Geol. Soc. Spec. Publ.*, vol. 106, Geological Society of London, 1996, pp. 321–335.
- [53] R. Hall, Reconstructing Cenozoic SE Asia, in: R. Hall, D.J. Blundell (Eds.), *Tectonic Evolution Of Southeast Asia*, Geological Society Special Publications, The Geological Society London, London, 1996, pp. 153–184.
- [54] M. Fuller, J.R. Ali, S.J. Moss, G.M. Frost, B. Richter, A. Mahfi, Paleomagnetism of Borneo, *J. Asian Earth Sci.* 17 (1999) 3–24.
- [55] H. Smyth, R. Hall, J. Hamilton, P. Kinny, East Java: Cenozoic basins, volcanoes and ancient basement, Indonesian Petroleum Association Thirtieth Annual Convention and Exhibition, 2005.
- [56] C. Cruciani, E. Carminati, C. Doglioni, Slab dip vs. lithospheric age: no direct function, *Earth Planet. Sci. Lett.* 238 (2005) 298–310.

Chapter 5

Major Australian-Antarctic Plate Reorganisation at Emperor-Hawaii Bend Time

Major Australian-Antarctic Plate Reorganization at Hawaiian-Emperor Bend Time

J. M. Whittaker,^{1*} R. D. Müller,¹ G. Leitchenkov,² H. Stagg,³ M. Sdrolias,¹ C. Gaina,⁴ A. Goncharov³

A marked bend in the Hawaiian-Emperor seamount chain supposedly resulted from a recent major reorganization of the plate-mantle system there 50 million years ago. Although alternative mantle-driven and plate-shifting hypotheses have been proposed, no contemporaneous circum-Pacific plate events have been identified. We report reconstructions for Australia and Antarctica that reveal a major plate reorganization between 50 and 53 million years ago. Revised Pacific Ocean sea-floor reconstructions suggest that subduction of the Pacific-Izanagi spreading ridge and subsequent Marianas/Tonga-Kermadec subduction initiation may have been the ultimate causes of these events. Thus, these plate reconstructions solve long-standing continental fit problems and improve constraints on the motion between East and West Antarctica and global plate circuit closure.

A long-standing controversy in global tectonics concerns the ultimate driving forces that episodically cause major plate tectonic reorganizations. Proponents of “top-down” mechanisms [e.g., (1, 2)] argue that plates them-

selves drive instabilities of the plate-mantle system, whereas others [e.g., (3)] have argued that major mantle overturns drive plate tectonic punctuations. The most prominent manifestation of this controversy is the Hawaiian-Emperor sea-

mount chain bend (HEB) (4). Whereas there is ample evidence from hotspot trails (5), paleomagnetism (4), geodynamic models (6), and intraplate volcanism (7) to support a mantle flow mechanism, there has been a lack of evidence for a plate reorganization at the original age of 43 million years ago (Ma) (8) proposed for the HEB (9). However, Wessel *et al.* (10) recognized that the recent redating of bend initiation to ~50 Ma (11) correlates the HEB with major tectonic events from around the Pacific, such as South Pacific triple-junction reorganization at magnetic anomaly chron 22-21 (49.7 to 47.9 Ma) (12), Farallon-Pacific fracture zone bends at magnetic anomaly chron 24-21 (53.3 to 47.9 Ma) (13), and the direction change and proposed halt of Pacific-Kula plate spreading at magnetic anomaly chron 24-20/19 (53.3 to 43.8/41.5 Ma) (14).

The southeast Indian Ocean is a region where a plate event contemporaneous with a major Pacific plate reorganization might be expected, but a historical paucity of magnetic anomaly data close to the Australian and Antarctic margins, combined with slow initial spreading rates, has resulted in poorly constrained plate fits before 50 Ma (15). Published reconstructions that assume a north-south spreading direction between Australia and Antarctica result in large overlaps between the South Tasman Rise and Cape Adare (15), and offsets in matching Australia-Antarctic geological terranes (16). Magnetic anomaly identifications, related to India-Antarctica spreading at 126 to 130 Ma (17), have been identified north of the Bruce Rise, Antarctica (Fig. 1), which results in the tectonically problematic juxtaposition of India-Antarctica-related magnetic anomalies between Australia and Antarctica when the Naturaliste Plateau is reconstructed to the north of the Bruce Rise (15). These problems indicate that Australia has been placed too far west with respect to a fixed Antarctica and that it is incorrect that the Perth and Vincennes fracture zones are conjugates (15). Two Australian-Antarctic fracture zone fabrics can be clearly identified from gravity anomaly data (Fig. 1): a northwest-southeast fabric on ocean floor older than chron 34 (83 Ma) and a north-south fabric on ocean crust younger than chron 21 (47.9 Ma). The model by Tikku and Cande (15) implies that the change in spreading direction resulting in these different fabrics occurred before chron 34 (83 Ma). Instead, we test the hypothesis that the Perth Fracture Zone is conjugate to a fracture zone, here named the Perth South Fracture Zone (Fig. 1), resulting in reconstruction of the Bruce Rise to the west of the Naturaliste Plateau. For our revised model, we investigate whether gravity

¹EarthByte Group, School of Geosciences, University of Sydney, Sydney 2006, Australia. ²VNIIOkeangeologia (Antarctic Branch), St. Petersburg 190121, Russia. ³Geoscience Australia, Canberra 2601, Australia. ⁴Center for Geodynamics, Norwegian Geological Survey, Trondheim 7491, Norway.

*To whom correspondence should be addressed: E-mail: j.whittaker@geosci.usyd.edu.au

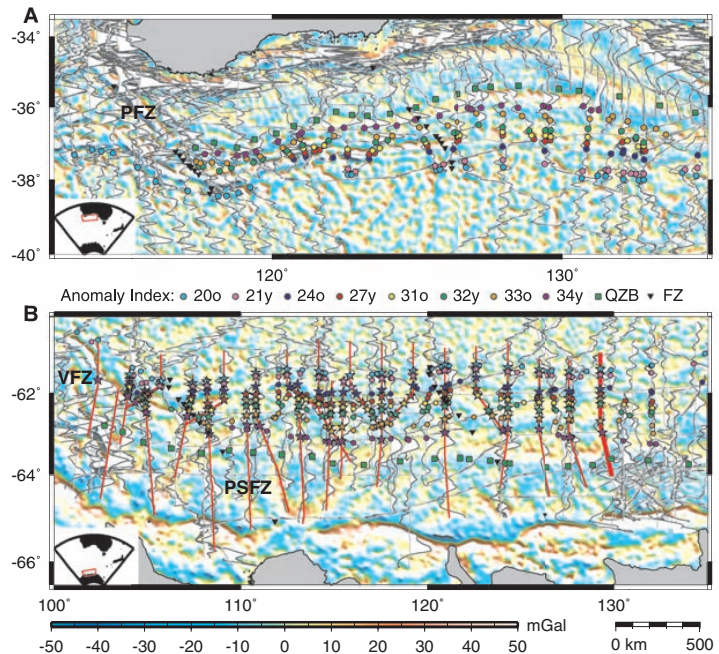
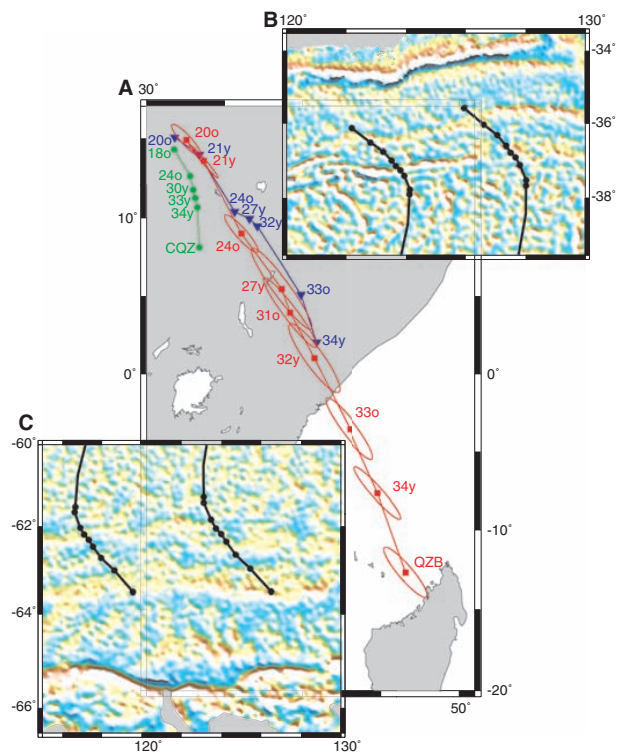


Fig. 1. Low-pass filtered (downward continued to the sea floor) 2-min gravity anomaly grid (18, 28) for (A) Southern Australia and (B) East Antarctica (inset shows locations). Overlaid are ship tracks (gray lines), magnetic anomaly wiggles (black lines filled with white), gravity anomaly picks [squares, QZB (Quiet Zone Boundary)], fracture zone picks (inverted triangles, FZ), and magnetic anomaly picks [stars, this study; circles, Tikku and Cande (15)] used in this paper. Red lines in (B) are Geoscience Australia and Russian shiptracks (see main text), and bold red is shiptrack GA-22825 (fig. S1). PFZ, Perth Fracture Zone; PSFZ, Perth South Fracture Zone; and VFZ, Vincennes Fracture Zone.

Fig. 2. (A) Poles about which Australia is restored to Antarctica based on calculated angles of rotation (finite poles of rotation) with 95% confidence interval ellipses. Red squares and red error ellipses represent our new rotation poles, inverted triangles are Tikku and Cande's (15) rotation poles, and green circles are Royer and Rollet's (29) rotation poles. (B) South Australian margin and (C) East Antarctic margin, downward continued gravity anomaly with fit of tectonic flow-lines resulting from our new model. Tectonic flow-lines are constructed for stage rotations between magnetic chrons shown in Fig. 1.



anomalies (18) permit a change in spreading direction at a younger time, resulting in a longer period of oblique relative motion than previously assumed.

New magnetic anomaly identifications made with recently acquired high-quality magnetic data in the Bruce Rise area (90° to 115°E) and along the Terre Adelie and Wilkes Land margins (115° to 132°E) were integrated with earlier identifications (15) (Fig. 1 and table S2). The motion of a

tectonic plate can be described by a rotation angle about a virtual axis that passes through the center of the Earth and intersects its surface (finite pole of rotation). We used the combined fracture zone and magnetic anomaly identifications (Fig. 1) to define a new set of plate boundaries and compute well-constrained finite rotations and 95% uncertainty intervals (Fig. 2 and tables S3 and S4) that describe our new plate motion history for Australia and East Antarctica.

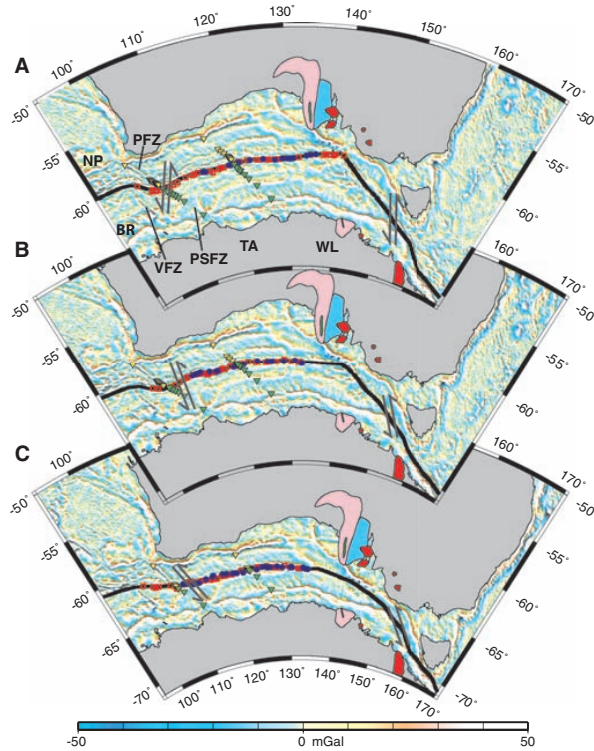
Our new plate reconstructions resolve long-standing continental and geological terrane fit problems with Australia, relative to Antarctica, positioned ~500 km east of previous reconstructions at 83 Ma (Fig. 3), and provide improved constraints on the motion between East and West Antarctica and global plate circuit closure.

When combined with geological evidence for relative plate motion changes around the Pacific, our reconstructions provide strong evidence for a major plate reorganization, which we argue was initiated by the subduction of the Izanagi-Pacific (I-P) ridge—a “top-down” mechanism. Circum-Pacific fracture zone bends document relative plate motion changes precipitated by the I-P ridge subduction, whereas the prominent HEB formed through a combination of altered Pacific plate motion and the well-documented deceleration of Pacific mantle (4, 6).

We present a new plate reconstruction for the western Pacific (Fig. 4) based on matching isochrons and a set of simple assumptions (table S5). In our plate model, mid-ocean ridge subduction beneath southern Japan occurs at 60 to 55 Ma, 20 million years later than proposed for Kula-Pacific (19) or Farallon-Izanagi (20) ridge subduction. The difference arises because I-P spreading ceases in previous models after 110 Ma, whereas our model incorporates continued spreading until the I-P ridge subducts beneath eastern Asia at 60 to 55 Ma. Cessation of spreading at the I-P ridge between 110 and 80 Ma is unlikely because the Izanagi plate was undergoing rapid motion, driven by net slab-pull force, from the north-northwest (21), immediately before the proposed spreading cessation.

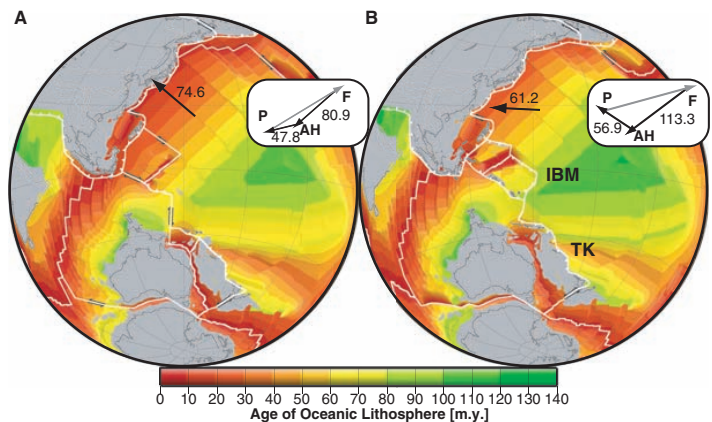
Metamorphism of the Ryoke Belt in southern Japan has previously been attributed to Kula-Pacific ridge subduction at 85 Ma (19), but the high-temperature/low-pressure Ryoke Belt cannot be uniquely linked to a ridge subduction event (22). Unreasonably high spreading rates of 35 to 40 cm/year during the Cretaceous Normal Superchron between the Pacific and Izanagi plates would be necessary to subduct the I-P ridge at 85 Ma, which is more than double the fastest current spreading rate globally [~15 cm/

Fig. 3. Australia-Antarctica reconstructions based on our rotations at three stage boundaries: (A) 47.9 Ma, chron 21; (B) 61 Ma, chron 27; and (C) 83 Ma, chron 34. All magnetic chron ages are based on the time scale of Cande and Kent (30). Underlying image shows downward continued gravity anomalies. At 83 Ma, the Naturaliste Plateau (NP) is located to the east of the Bruce Rise (BR), there is no overlap between southeast Australia and Antarctica, and the Australian/Antarctic geological provinces align. Dark gray arrows show direction of motion of Australia and Antarctica for stages chron 21 to chron 18, chron 27 to chron 21, and chron 34 to chron 27 in (A), (B), and (C), respectively. Magnetic anomaly identifications for Australia and Antarctica for each reconstruction time are shown as red circles and black squares, respectively.



Inverted triangles are fracture zone identifications for each chron older than the time of reconstruction. Geological provinces are as follows: pink, Neoproterozoic basin (~2.5 billion years ago (Ga)); green, Paleoproterozoic basin (~1.69 Ga); light blue, metasediments (~2 Ga); and red, plutonic belt (~500 Ma) (16, 31, 32). WL, Wilkesland; TA, Terra Adelie; PFZ, Perth Fracture Zone; PSFZ, Perth South Fracture Zone; and VFZ, Vincennes Fracture Zone.

Fig. 4. Reconstructed oceanic crustal age grids at two time slices (A) 55 Ma and (B) 45 Ma. Black arrows (in mm/year) show western Pacific (30°N, 150°E) plate motion over the stages 60 to 50 Ma and 50 to 40 Ma, respectively. (Inset) Vectors (in mm/year) (same 10-Ma stages) show motion of the eastern Pacific (30°N, 240°E) (P) and Farallon (F) plates relative to fixed African hotspots (AH) over the period 60 to 50 Ma and 50 to 40 Ma. Eastern and western Pacific directions and changes in plate motion are substantially different. Geographical location of poles (latitude, longitude) about which rotations (angle) describing Pacific plate motion relative to an African hotspot reference frame are 55.0°N, -118.4°W, -7.90° and 59.4°N, -19.3°W, -5.52° at 60 to 50 Ma and 50 to 40 Ma, respectively. The resultant relative plate motions between the Pacific and Farallon plates show that our model explains the shape of the Pacific-Farallon fracture zone bend as well as the HEB. TK, Tonga-Kermadec subduction zone; IBM, Izu-Bonin-Marianas subduction zone. m.y., millions of years.



year between the Pacific and Nazca plates (23)]. We propose that subparallel subduction of the I-P mid-ocean ridge beneath Japan at 60 to 55 Ma resulted in nearly simultaneous slab break-off along the length of the Japanese trench (~2700 km). Geological observations from southern Japan support subduction of the I-P ridge and subsequent slab break-off at 60 to 55 Ma. Evidence includes cessation of a major accretion phase in the Late Cretaceous (24), emplacement of the Okitsu Melange due to subduction of hot, buoyant material at 55 Ma (24), and cross-cutting fault fabrics that indicate a counterclockwise rotation in relative plate motions between Eurasia and the I-P plate, which are also consistent with paleothermal and paleopressure data, between 55 and 34 Ma (25).

Rapid subduction of the I-P ridge, over a vast distance, triggered a chain reaction of tectonic plate reorganizations. With complete subduction of the I-P ridge at 55 Ma, forces acting on the Pacific changed from ridge-push to slab-pull, which changed Pacific absolute plate motions from northwest to west (Fig. 4). The change in Pacific plate motion caused cessation of Tasman Sea spreading at ~52 Ma (26). Increased slab pull north of Australia, due to a westerly progression of the subducting Wharton Basin mid-ocean ridge (Fig. 4), changed Australian absolute plate motion from northwest to north. A combination of Australian and Pacific plate motion changes between 53 and 50 Ma initiated both the Tonga-Kermadec (2) subduction system and the Izu-Bonin-Marianas subduction systems, which initiated likely before 50 Ma, due to convergence across a fracture zone caused by the Pacific plate motion change (27). We suggest that the observed slowdown of sub-Pacific mantle flow at 47 Ma (4) was due to progressive impediment of lateral sub-Pacific mantle flow by the descending

slabs of the Izu-Bonin-Marianas and Tonga-Kermadec subduction zones.

The observed opposite bend geometries of the Emperor-Hawaii seamount chain and the Pacific-Farallon fracture zones can be explained with combined absolute (relative to a fixed reference frame) and relative plate motions. Clockwise rotation of eastern Pacific absolute plate motion, combined with stable Farallon plate motion (Fig. 4), results in a clockwise bend in Pacific-Farallon fracture zones at 53 to 49 Ma (16). In the western Pacific, a counterclockwise change in absolute plate motion, from northwest to west due to Izanagi Ridge subduction (Fig. 4), combined with a sub-Pacific mantle flow slowdown, results in the HEB. This conceptual model is testable via three-dimensional fully dynamic mantle flow simulations.

References and Notes

1. D. L. Anderson, *Science* **293**, 2016 (2001).
2. M. Gurnis, C. Hall, L. Lavier, *Geochem. Geophys. Geosyst.* **5**, Q07001 (2004).
3. S. D. King, J. P. Lowman, C. W. Gable, *Earth Planet. Sci. Lett.* **203**, 83 (2002).
4. J. A. Tarduno *et al.*, *Science* **301**, 1064 (2003).
5. P. Molnar, J. Stock, *Nature* **327**, 587 (1987).
6. B. Steinberger, R. Sutherland, R. J. O'Connell, *Nature* **430**, 167 (2004).
7. C. A. Finn, R. D. Müller, K. S. Panter, *Geochem. Geophys. Geosyst.* **6**, Q02005 (2005).
8. D. A. Clague, G. B. Dalrymple, *U.S. Geol. Surv. Prof. Paper* **1350** (1987).
9. I. O. Norton, *Tectonics* **14**, 1080 (1995).
10. P. Wessel, Y. Harada, L. W. Kroenke, *Geochem. Geophys. Geosyst.* **7**, Q03L12 (2006).
11. W. D. Sharp, D. A. Clague, *Science* **313**, 1281 (2006).
12. S. C. Cande, E. M. Herron, B. R. Hall, *Earth Planet. Sci. Lett.* **57**, 63 (1982).
13. D. W. Caress, H. W. Menard, R. N. Hey, *J. Geophys. Res.* **93**, 2813 (1988).
14. P. F. Lonsdale, *Bull. Geol. Soc. Am.* **100**, 733 (1988).
15. A. A. Tikku, S. C. Cande, *J. Geophys. Res.* **104**, 661 (1999).
16. C. A. Finn, D. Moore, D. Damaske, T. Mackey, *Geology* **27**, 1087 (1999).
17. C. Gaina, R. D. Müller, B. Brown, T. Ishihara, S. Ivanov, *Geophys. J. Int.* **170**, 151 (2007).
18. D. T. Sandwell, W. H. F. Smith, *Geophys. J. Int.* **163**, 79 (2005).
19. D. C. Engebretson, A. Cox, R. G. Gordon, *Geol. Soc. Am. Spec. Pap.* **206**, 1 (1985).
20. C. T. Onishi, G. Kimura, *Tectonics* **14**, 1273 (1995).
21. K. Otsuki, *Island Arc* **1**, 51 (1992).
22. M. Brown, *J. Metamorphic Geol.* **16**, 3 (1998).
23. W. P. Schellart, J. Freeman, D. R. Stegman, L. Moresi, D. May, *Nature* **446**, 308 (2007).
24. S. M. Agar, R. A. Cliff, I. R. Duddy, D. C. Rex, *J. Geol. Soc.* **146**, 893 (1989).
25. J. C. Lewis, T. B. Byrne, *Tectonics* **20**, 548 (2001).
26. C. Gaina *et al.*, *J. Geophys. Res.* **103**, 12413 (1998).
27. C. E. Hall, M. Gurnis, M. Sdrolias, L. L. Lavier, R. D. Müller, *Earth Planet. Sci. Lett.* **212**, 15 (2003).
28. W. H. F. Smith, D. T. Sandwell, *J. Geophys. Res.* **99**, 21803 (1994).
29. J.-Y. Royer, N. Rollet, *Aust. J. Earth Sci.* **44**, 543 (1997).
30. S. C. Cande, D. V. Kent, *J. Geophys. Res.* **100**, 6093 (1995).
31. G. Duclaux, P. Rey, S. Guillot, R. P. Ménot, *Geology* **35**, 715 (2007).
32. R. P. Ménot *et al.*, in *Antarctica: A Keystone in a Changing World—Online Proceedings of the 10th ISAES*, A. K. Cooper *et al.*, Eds. (USGS Open-File Rep. 2007-1047, Short Research Paper 048, 2007).
33. We thank W. Smith for providing the downward continued gravity grid. Reviews by M. Gurnis and S. Cande, as well as detailed comments on early versions of the manuscript by P. Wessel, A. Dutkiewicz, and J. Stock, improved the manuscript considerably. We acknowledge the Ministry of Natural Resources of the Russian Federation and Geoscience Australia, who funded collection of some of the new marine magnetic data used in this work.

Supporting Online Material

www.sciencemag.org/cgi/content/full/318/5847/83/DC1
Fig. S1
Tables S1 to S5
References

13 April 2007; accepted 3 September 2007
10.1126/science.1143769

Chapter 6

Discussion

Mid-ocean ridges form an integral part of the Earth's geological system and are intrinsically linked to global plate tectonic motions. Crust formed at mid-ocean ridges interacts with ocean currents to influence marine sedimentation and ocean circulation patterns. These interactions means that a solid understanding of the processes involved in shaping the morphology of oceanic crust are crucial. Subduction of a mid-ocean ridge can upset the balance of global plate motions and influences the composition and morphology of the over-riding plate margin through the development of a slab window.

This thesis uses a combination of global datasets and global and regional studies to examine how mid-ocean ridge processes shape the seafloor of the ocean basins interact with the oceanic processes of sedimentation and circulation, influence continental margins, and influence or even precipitate global plate tectonic organisations.

Parameters influencing seafloor roughness

Plate tectonic half-spreading rates and seafloor sediment cover are both known to strongly influence observed basement roughness. The results of our global analysis of sediment thickness and gravity roughness found that each kilometre of sediment [Divins, 2004] results in a $\sim 14\%$ decrease in gravity roughness. We also find that global half-spreading rates [Müller, et al., 2008] (a) faster than 35 mm/yr result in low gravity roughness ($\sim 7\text{mGal}$), (b) between 35-15 mm/yr result in increasingly rough and variable gravity roughness, and (c) slower than 15 mm/yr form high-amplitude gravity roughness ($\sim 15\text{mGal}$). These results differ from previous find-

ings [Small and Sandwell, 1989; Smith, 1998] that suggest gravity roughness continues to increase with decreasing spreading rates $< 15\text{ mm/yr}$.

Spreading obliquity is a ubiquitous phenomenon, observed at $\sim 72\%$ of spreading centres [Woodcock, 1986]. Higher angles of spreading obliquity are related to increasing ridge segmentation [Abelson and Agnon, 1997; de Alteriis, et al., 1998; Mosher and Massell Symons, 2008] and seismicity [de Alteriis, et al., 1998], both due to increased brittle fracturing at higher spreading angles [de Alteriis, et al., 1998]. An analysis of spreading obliquity and residual gravity roughness, where the influence of sediment cover and spreading rate have been removed, reveals that for obliquities between 0° and 45° , variation of residual roughness with spreading obliquity fits an inverted cosine curve. However, at spreading obliquities $> 45^\circ$ residual roughness increases much more rapidly than expected from a cosine relationship, indicating that an additional mechanism, likely brittle fracturing, causes dramatically rougher ocean basement at higher spreading obliquities.

Long-term deviations of 5-20 mGal over periods $> 40\text{ Myr}$ and in many cases $> 60\text{ Myr}$ remain in the residual roughness grid after the removal of roughness attributable to spreading rate, sediment thickness and spreading obliquity indicating an additional parameter influences oceanic roughness. It is likely that these long-term deviations are largely attributable to the temperature and fertility conditions of the underlying mantle. Spreading rates influence marine basement roughness by affecting the bulk extent of melting beneath mid-ocean ridges. However, melt volumes are also related to crustal thickness, a parameter strongly con-

trolled by mantle temperature [Asimow and Langmuir, 2003; Klein and Langmuir, 1987; McKenzie and Bickle, 1988]. Mantle fertility additionally affects the bulk extent of melting [Klein and Langmuir, 1987; Langmuir, et al., 1992], with depleted mantle producing lower melt volumes [Meyzen, et al., 2003] and thus rougher basement.

Basement in the Norwegian-Greenland Sea, where the Reykjanes Ridge interacts with the Icelandic hotspot could be expected to be relatively rough based on spreading rates of <20 mm/yr however, the area is characterised by high heat flow, anomalously thick crust, sparse fracture zones [Bown and White, 1994] and basement that is 3-10 mGal smoother than expected. It is likely that anomalously high mantle temperatures have maintained excess partial melts and reduced brittle fracturing leading to relatively smooth crust in spite of slow spreading rates. It appears likely that relatively smooth basement is formed regardless of spreading rates when the mid-ocean ridge is underlain by hot supercontinent-derived mantle, which is the case for most oceanic crust aged between 80 and 130 Myr with the main exception of crust in the North Pacific.

Relatively smooth basement is predicted for the Australian-Antarctic Discordance (AAD) based on spreading rates of 35-40 mm/yr since ~40 Myr ago. However, the AAD exhibits basement up to 8 mGal rougher than predicted. Crustal thickness in the AAD is 2-4 km thinner than adjacent crust, implying a 150 °C decrease in mantle temperature [West, et al., 1994]. Also, the AAD is located at the site of a palaeo-subduction zone, with current lavas likely sourced from depleted magmas derived from subducted oceanic crust [Ritzwoller, et al., 2003]. Both cool mantle temperatures and low mantle fertility result in reduced mid-ocean ridge melt volumes [Meyzen, et al., 2003] and have resulted in rough basement in the AAD despite relatively fast spreading rates over the past 15 Myr [Marks, et al., 1999].

Rougher than expected basement found surrounding the western Indian and central and southern Atlantic mid-ocean ridges is likely due to widespread mantle depletion. These areas are relatively distal to large mantle plumes, which results in poor upper

mantle replenishment due to dependence on slow, localised mantle upwellings [Meyzen, et al., 2007]. An unusual geochemical signature indicates that depleted rather than cold mantle is at least partly responsible for anomalously rough basement at the Southwest Indian Ridge [Meyzen, et al., 2003].

Investigation of interaction between MOR and other Earth system processes including oceanic, sedimentary and geodynamic

The patterns of seismic stratigraphy observed in the Adare Trough area are related to sediment supply and the strength of Antarctic bottom currents. Sediment cover on the western side of the Adare Trough (approx. 100 km from the central graben) is considerably thicker than on the eastern side. Antarctic Bottom Waters move from the Ross Shelf past the western side of the Adare Trough [Orsi, et al., 1999]. It is likely that this preferential bottom water flow has led to the thicker sediment observed west of the Adare Trough compared to the eastern side.

The flow pattern of Antarctic Bottom Waters are likely to have been different in the past, largely depending on bathymetric configurations. Mid-ocean ridges and transform faults can form significant barriers to bottom current flow [Bice, et al., 1998]. Our results show that although there has been movement and change in the orientation of mid-ocean ridges offshore Cape Adare there is no modelled mid-ocean ridge impediment to bottom current flow between the Ross Shelf and the Adare Basin since 33 Ma. It is possible however that transform faults, related to the mid-ocean ridge, may have impeded the flow of Antarctic Bottom Waters during the evolution of the Adare Trough.

Temporal variations in sediment supply and the strength of ocean currents are demonstrated throughout the seismic stratigraphy. Low sediment supply reaching the Southern Ocean from the isolated, subsiding basins of the Western Ross Sea during the Oligocene to late Early Miocene [Brancolini, et al., 1995; Davey, et al., 2000] likely led to the regional SU3/4 hiatus. Sedimentation in the Adare Basin region resumed at 17 Ma (SU2) and continued to 14 Ma, presumably due to greater volumes of sedi-

ment reaching the Southern Ocean as basins in the Western Ross Sea became less restricted. There is no evidence of bottom current activity during this period with Sed3 (17 to 15 Ma) exhibiting only turbidite deposited graded bedding [Hayes, et al., 1975] and experiencing a relatively high sedimentation rate [Frakes, 1975], both indicative of relatively weak bottom currents.

Bottom currents clearly strengthen at ~15 Ma with Sed2 exhibiting numerous contour channels, severe sediment winnowing [Frakes, 1975], and a seismically transparent unconformity, lasting from the Mid-Miocene to the Pliocene [Hayes, et al., 1975] all indicating that strong bottom currents were operating during the deposition of this unit. The base of Sed2 corresponds to the onset of Mid-Miocene cooling [Miller, et al., 1991; Shackleton and Kennett, 1975], which caused an intensification of gyral circulation and increased the strength of Southern Ocean oceanographic fronts [Kennett and C., 1985; Thunell and Belyea, 1982]. A consequence of increased sea-ice cover and a stronger Antarctic Slope Front, due to glacial expansion, was increased production of Antarctic Bottom Waters from the mid-Miocene. These strong bottom currents continued, leading to the winnowed sediment and hiatus observed in Sed2, until the Pliocene.

Reconstruction of Wharton Ridge slab window

Reconstructions revealing the geometry, extent and position of the slab window formed due to the subduction of the Wharton Ridge were created at 5 million year intervals from 70 Ma to the present. The palaeo-position of a slab window are normally estimated using geological data from the overriding plate, such as changes in volcanism and tectonic events such as regional uplift. Calculation of the palaeo-position of the Wharton Ridge slab window beneath Sundaland utilised the method of Thorkelson [1996] and time-dependent plate motion vectors, reconstructed palaeo-ages of the ocean floor, and the reconstructed location of the Wharton Ridge through time. The geometry of a slab window is effected by relative plate motions, pre-subduction ridge-transform fault geometry, subduction

angles, thermal erosion, deformation caused by spherical shell stress and lateral and down-dip changes in the angle of slab dip [Thorkelson, 1996]. The location of the Wharton Ridge slab window was calculated assuming a simple ridge-only geometry, a horizontal subducted slab, no thermal erosion of the diverging plate edges, and no deformation from spherical shell stress. The lateral extent of the slab window was limited to 1000 km perpendicular to the trench because at this point the slab can be assumed to have reached the 660 km mantle discontinuity and the slab window would no longer have a discernable affect on the overriding plate.

Relationship between plate kinematics and overriding plate tectonic regimes

Comparison of tectonic regimes on the Sundaland overriding plate margin with the direction and rate of plate motions at the Sundaland subduction zone since 80 Ma found that tectonic regime is strongly linked to the motion of the upper plate margin. A consistently advancing upper plate is found to correspond to compression in the overriding back-arc, caused by the collision between the down-going plate and the advancing overriding plate. An advancing upper plate, where the margin advances more rapidly than the core, correlates with extension in the upper plate (subduction hinge roll-back), for example in the southern Andaman Sea, Sumatra and Java at 30-15 Ma, 35-15, and 45-15 Ma respectively. Uniform upper plate retreat correlates with extension in the upper plate for example, Javanese non-spreading extension 60-50 Ma, and spreading in the Andaman Sea between 15-0 Ma.

While the direction of motion of the overriding plate is most closely linked with the tectonic regime experienced by the overriding margin, the subduction of active and inactive oceanic ridges can influence and even change the observed tectonic regime. For example, compression experienced in present-day Java is enhanced by subduction of the Roo Rise volcanic ridge, while in Sumatra, from 15 Ma to the present, compressional forces caused by subduction of the extinct Wharton Ridge and Investigator Fracture Zone have overridden extensional forces related to upper

plate retreat. The underlying Wharton Ridge slab window likely exacerbated extension in the Java Sea and south Kalimantan region and the possible Makassar Strait seafloor spreading between 60Ma and 45 Ma. The slab window may also have enabled extension to continue in Sumatra from 50 Ma until 35 Ma when a uniformly advancing upper plate would likely have led to a compressive regime. Progression of the slab window across Java and southern Sumatra correlates with Indonesian volcanic activity. The underlying slab window corresponds to an absence of Javanese volcanism until ~ 42 Ma [Prawirodirdjo, et al., 1997], and the progressing edge of the slab window likely related to an episode of volcanism from 60-50 Ma in southern Sumatra.

New plate reconstruction for Australia-Antarctic separation

The historical paucity of magnetic anomaly data close to the Australian and Antarctic margins, combined with slow initial spreading rates, has resulted in poorly constrained plate fits before 50 Ma [Tikku and Cande, 1999]. The Australian-Antarctic plate reconstruction model of Tikku and Cande [1999] that assumes a north-south spreading direction after 83 Ma implies that the change in spreading direction resulting in these different fabrics occurred before chron 34 (83 Ma). However, published reconstructions that assume a north-south spreading direction between Australia and Antarctica result in large overlaps of continental South Tasman Rise and Cape Adare crust [Tikku and Cande, 1999], and result in offsets in matching Australia-Antarctic geological terranes [Finn, et al., 1999]. Another problem involves India-Antarctica spreading-related magnetic anomaly identifications on crust located north of the Bruce Rise Antarctica aged 126-130 Ma [Gaina, et al., 2007]. Reconstructions where the Naturaliste Plateau is reconstructed to the north of the Bruce Rise result in the tectonically problematic juxtaposition of these India-Antarctic-related magnetic anomalies between Australia and Antarctica [Tikku and Cande, 1999]. All these problems indicate that Australia has been placed too far west with respect to a fixed Antarctica and that it is incorrect that the Perth and

Vincennes fracture zones are conjugates [Tikku and Cande, 1999].

Recently acquired high-quality magnetic data in the Bruce Rise area (90° to 115° E) and along the Terre Adelie and Wilkes Land margins (115° to 132° E) enabled new magnetic anomaly identifications to be made on the Antarctic coastline. These new magnetic anomaly identifications combined with new, high-resolution satellite-derived gravity data, that enabled identification and matching of the Antarctic margin Perth South Fracture Zone with the Australian margin Perth Fracture Zone and have enabled a revised reconstruction of early Australian-Antarctic separation. The new Australia-Antarctica plate reconstruction, based on a change in relative plate motion from northwest-southeast to north-south at ~ 50 Ma is derived from a combination of magnetic, gravity and other geological data and shows that Australian-Antarctic reconstructions should result in the Bruce Rise being located to the west of the Naturaliste Plateau. This revised model reveals a period of oblique relative motion lasting for approximately 30 million years longer than previously assumed and also resolve longstanding continental and geological terrane fit problems and provide improved constraints on the motion between East and West Antarctica and global plate circuit closure.

Model of catastrophic subduction leading to plate reorganisation

When combined with geological evidence for relative plate motion changes around the Pacific, the new Australian-Antarctic reconstructions presented in this thesis provide strong evidence for a major plate reorganization, hypothesised here to have been initiated by the subduction of the Izanagi-Pacific ridge - a top-down mechanism. Circum-Pacific fracture zone bends document relative plate motion changes precipitated by the Izanagi-Pacific ridge subduction, whereas the prominent Hawaiian-Emperor Bend formed through a combination of altered Pacific plate motion and the well-documented deceleration of Pacific mantle [Steinberger, et al., 2004; Tarduno, et al., 2003]. In the plate model presented, mid-ocean ridge subduction beneath southern Japan oc-

curs at 60 to 55 Ma, 20 million years later than proposed for Kula-Pacific [Engebretson, et al., 1985] or Farallon-Izanagi [Onishi and Kimura, 1995] ridge subduction. The difference arises because Izanagi-Pacific spreading ceases in previous models after 110 Ma, whereas this model incorporates continued spreading until the Izanagi-Pacific ridge subducts beneath eastern Asia at 60 to 55 Ma. Unreasonably high spreading rates of 35 to 40 cm/year during the Cretaceous Normal Superchron between the Pacific and Izanagi plates would be necessary to subduct the Izanagi-Pacific ridge at 85 Ma, which is more than double the fastest current spreading rate globally. Subparallel subduction of the Izanagi-Pacific mid-ocean ridge beneath Japan at 60 to 55 Ma is proposed to have resulted in nearly simultaneous slab break-off along the length of the Japanese trench (~ 2700 km). Geological observations from southern Japan support subduction of the Izanagi-Pacific ridge and subsequent slab break-off at 60 to 55 Ma.

Rapid subduction of the Izanagi-Pacific ridge, over a vast distance, triggered a chain reaction of tectonic plate reorganizations involving the change in Pacific absolute plate motions from northwest to west, cessation of Tasman Sea spreading at ~ 52 Ma [Gaina, et al., 1998], the change in Australian absolute plate motion from northwest to north, and initiation of the Tonga-Kermadec and Izu-Bonin-Marianas subduction systems. The observed slowdown of sub-Pacific mantle flow at 47 Ma [Tarduno, et al., 2003] was likely due to progressive impediment of lateral sub-Pacific mantle flow by the descending slabs of the Izu-Bonin-Marianas and Tonga-Kermadec subduction zones.

Chapter 7

Conclusion

Mid-ocean ridges control seafloor morphology and also influence the evolution of over-riding plate margins during mid-ocean ridge subduction. Understanding the role of mid-ocean ridges is crucial to understanding the landscape, composition and dynamic processes of the Earth.

Seafloor roughness varies considerably across the world's ocean basins and is fundamental to controlling circulation and mixing in the oceans. While seafloor spreading rates are well known to influence the roughness of the oceanic basement, the role of other parameters is less well understood. Relationships between both spreading rate and sediment thickness with gravity-derived roughness are determined using global datasets. The influence of these parameters is then removed creating a residual roughness grid that reveals that long-wavelength changes in mantle conditions play a major role in determining oceanic basement roughness. Smooth crust is associated with hot mantle, as well as fast spreading rates, while rough crust is associated with cool and/or depleted mantle, highly oblique spreading ($>45^\circ$) directions, and slow spreading rates. These results are important for the understanding of upper mantle convection patterns and the manner in which they interact with the lithosphere and are in contrast to previous studies of seafloor roughness, which are mostly based on very limited data sets from the mid-ocean crests.

The important role of rough seafloor features in influencing ocean circulation and climate is revealed in the analysis of seismic, bathymetric and geodynamic data from the Adare Trough, an extinct mid-ocean ridge. The rough features of the extinct ridge act as a barrier to ocean bottom currents and impact on sedi-

mentation patterns. The Adare Trough is a relatively small bathymetric feature and likely would not have acted as a regional impediment to ocean circulation and mixing. However, the way that ocean bottom currents interacted with the Adare Trough likely occurs at many more extensive mid-ocean ridges. This study shows the importance of understanding the parameters influencing seafloor roughness in order to accurately reconstruct vanished ocean basins for use in palaeo-ocean circulation and palaeo-climate models.

The kinematics and time-dependence of back-arc extension or compression is one of the most poorly understood aspects of plate tectonics, and has nearly exclusively been studied based on snapshots of present-day observations. In this paper absolute and relative plate motions are combined with reconstructions of now subducted ocean floor to analyse subduction kinematics and upper plate strain from geological observations since 80Ma along the 3200 km long Sunda Trench, one of the largest subduction systems on Earth, to show how several key factors including slab window formation, subduction of aseismic ridges, absolute/relative plate motion and hinge rollback are related to time-dependent extension and compression on the overriding plate.

The cause of the Hawaiian-Emperor seamount chain bend has been a long-standing controversy, with alternative mantle-driven and plate reorganisation hypotheses. Evidence from hotspot trails, paleomagnetism, geodynamic models, and intraplate volcanism have supported the mantle-driven mechanism hypothesis, while no evidence of coeval plate motion changes could be found in plates surrounding the Pacific. The recent redating of the Hawaiian bend from 43 Ma to 50

Ma means there are a number of contemporaneous relative plate motion changes. A previously unmapped major relative plate motion change at 53-50 Ma between Australia and Antarctica supports the plate reorganisation hypothesis for the Hawaiian-Emperor bend. Resulting plate reconstructions solve long-standing continental fit problems, and improve constraints on the motion between East and West Antarctica and global plate circuit closure. Use of a global plate tectonic reconstruction model suggests that subduction of the Izanagi-Pacific mid-ocean ridge at 60-55 Ma precipitated a major plate and mantle flow reorganisation that caused the formation of the Hawaiian-Emperor bend.

Chapter 8

References

- Abelson, M., and A. Agnon (1997), Mechanics of oblique spreading and ridge segmentation, *Earth Planet. Sci. Lett.*, **148**, 405-421.
- Asimow, P. D., and C. H. Langmuir (2003), The importance of water to oceanic mantle melting regimes, *Nature*, **421**, 815-820.
- Bice, K. L., et al. (1998), Reconstruction of realistic early Eocene paleobathymetry and ocean GCM sensitivity to specified basin configuration, in *Tectonic boundary conditions for climate reconstructions*, edited by T. J. Crowley and K. Burke, pp. 227-247, Oxford University Press, Oxford, United Kingdom.
- Billen, M. I., and M. Gurnis (2001), A low viscosity wedge in subduction zones, *Earth Planet. Sci. Lett.*, **193**, 227-236.
- Bown, J. W., and R. S. White (1994), Variation with spreading rate of oceanic crustal thickness and geochemistry, *Earth Planet. Sci. Lett.*, **121**, 435-449.
- Brancolini, G., et al. (1995), Seismic Facies and glacial history in the Western Ross Sea (Antarctica), *Antarctic Research Series*, **68**, 209-233.
- Brown, B., et al. (2006), Circum-Antarctic palaeobathymetry: Illustrated examples from Cenozoic to recent times, *Palaeogeography, Palaeoclimatology, Palaeoecology*, **231**, 158168.
- Coffin, M. F., and O. Eldholm (1994), Large Igneous Provinces: Crustal Structure, Dimensions, and External Consequences, *Reviews of Geophysics*, **32**, 1-36.
- Davey, F. J., et al. (2000), A revised correlation of the seismic stratigraphy at the Cape Roberts drill sites with the seismic stratigraphy of the Victoria Land Basin, Antarctica, *Terra Antartica*, **7**, 215-220.
- de Alteriis, G., et al. (1998), Matching satellite-derived gravity signatures and seismicity patterns along mid-ocean ridges, *Terra Nova*, **10**, 177-182.
- Dickinson, W. R., and W. S. Snyder (1979), Geometry of subducted slabs related to San Andreas transform, *Journal of Geology*, **87**, 609-627.
- Divins, D. L. (2004), Total sediment thickness of the world's oceans and marginal seas, edited, National Geophysical Data Center.
- Engebretson, D. C., et al. (1985), Relative motions between oceanic and continental plates in the Pacific Basin, *Geol. Soc. of Am. Special Paper*, **206**, 1-59.
- Finn, C. A., et al. (1999), Aeromagnetic legacy of early Paleozoic subduction along the Pacific margin of Gondwana, *Geology*, **27**, 1087-1090.
- Frakes, L. A. (1975), Paleoclimatic significance of some sedimentary components at Site 274, in

- Initial Reports of the Deep Sea Drilling Project*, edited, pp. 785-787, U.S. Government Printing Office, Washington.
- Gaina, C., et al. (1998), The tectonic history of the Tasman Sea: a puzzle with 13 pieces, *Journal of Geophysical Research*, **103**, 12413-12433.
- Gaina, C., et al. (2007), Breakup and early seafloor spreading between India and Antarctica, *Journal of Geophysics International*, **170**, 151.
- Hayes, D. E., et al. (1975), Leg XXVIII, *Initial Reports of the Deep Sea Drilling Project*, U.S. Govt. Printing Office, Washington.
- Heine, C., et al. (2004), Reconstructing the lost Eastern Tethys Ocean Basin: Constraints for the convergence history of the SE Asian margin and marine gateways, in *Continent-Ocean Interactions in Southeast Asia*, edited by P. Clift, et al., American Geophysical Union, Washington.
- Keller, W. R. (2004), Cenozoic plate tectonic reconstructions and plate boundary processes in the Southwest Pacific, Ph.D Thesis, California Institute of Technology, Pasadena, California.
- Kennett, J. P., and V. D. B. C. C. (1985), Southwest Pacific Cenozoic paleoceanography, US Government Printing Office.
- Klein, E. M., and C. H. Langmuir (1987), Global correlations of ocean ridge basalt chemistry with axial depth and crustal thickness, *J. Geophys. Res.*, **92**, 8089-8115.
- Klein, G. D. (1985), The frequency and periodicity of preserved turbidities in submarine fans as a quantitative record of tectonic uplift in collision zones, *Tectonophysics*, **119**, 181-193.
- Langmuir, C. H., et al. (1992), Petrological systematics of mid-ocean ridge basalts: constraints on melt generation beneath ocean ridges, in *Mantle Flow and Melt Generation at Mid-Ocean Ridges*, *AGU Geophysical Monograph*, edited by J. Phipps Morgan, et al., pp. 183-280.
- Malinverno, A. (1991), Inverse square-root dependence of mid-ocean-ridge flank roughness on spreading rate, *Nature*, **352**, 58-60.
- Marks, K. M., et al. (1999), Evolution of the Australian-Antarctic discordance since Miocene time, *J. Geophys. Res.*, **104**, 4697-4981.
- McKenzie, D., and M. J. Bickle (1988), The volume and composition of melt generated by extension of the lithosphere, *J. Petrol.*, **29**, 625-679.
- Meyzen, C. M., et al. (2007), Isotopic portrayal of the Earth's upper mantle flow field, *Nature*, **447**, 1069-1074.
- Meyzen, C. M., et al. (2003), A discontinuity in mantle composition beneath the southwest Indian ridge, *Nature*, **42**, 731-733.
- Miller, K. E., et al. (1991), Unlocking the ice house: Oligocene-Miocene oxygen isotopes, eustacy and margin erosion, *Journal of Geophysical Research*, **96**, 6829-6848.
- Mosher, S., and C. Massell Symons (2008), Ridge reorientation mechanisms: Macquarie Ridge Complex, Australia-Pacific plate boundary, *Geology*, **36**, 119-122.
- Müller, R. D., et al. (2005), Crustal structure and rift flank uplift of the Adare Trough, Antarctica, *Geochem. Geophys. Geosyst.*
- Müller, R. D., et al. (1997), Digital isochrons of the world's ocean floor, *Journal of Geophysical Research*, **102**, 3211-3214.
- Müller, R. D., et al. (2008), Age, spreading rates and spreading asymmetry of the world's ocean crust, *Geochem. Geophys. Geosyst.*

- O'Neill, C., et al. (2005), On the Uncertainties in Hotspot Reconstructions, and the Significance of Moving Hotspot Reference Frames, *Geochemistry, Geophysics, Geosystems*.
- Onishi, C. T., and G. Kimura (1995), Change in fabric of melange in the Shimanto Belt, Japan: Change in relative convergence?, *Tectonics*, **14**, 1273-1289.
- Orsi, A. H., et al. (1999), Circulation, mixing and production of Antarctic Bottom Water, *Progress in Oceanography*, **43**, 55-109.
- Prawirodirdjo, L., et al. (1997), Geodetic observations of interseismic strain segmentation at the Sumatra zone, *Geophysical Research Letters*, **24**, 2601-2604.
- Ritzwoller, M. H., et al. (2003), A resolved mantle anomaly as the cause of the Australian-Antarctic Discordance, *J. Geophys. Res.*, **108**, 2559-2559.
- Sandwell, D. T., and W. H. F. Smith (2005), Retracking ERS-1 altimeter waveforms for optimal gravity field recovery, *Geophys. J. Int.*, **163**, 79-89.
- Shackleton, N. J., and J. P. Kennett (1975), Paleotemperature History of the Cenozoic and the Initiation of Antarctic Glaciation: Oxygen and Carbon Isotope Analysis in D.S.D.P. Sites 277, 279, and 281., in *Initial Reports of the Deep Sea Drilling Project*, edited by J. P. Kennett, et al., U.S. Government Printing Office, Washington D.C.
- Small, C., and D. T. Sandwell (1989), An abrupt change in ridge-axis gravity with spreading rate, *Journal of Geophysical Research*, **94**, 17383-17392.
- Smith, W. H. F. (1998), Seafloor tectonic fabric from satellite altimetry, *Ann. Rev. Earth Planet. Sci.*, **26**, 697-747.
- Steinberger, B., et al. (2004), Prediction of Emperor-Hawaii seamount locations from a revised model of global plate motion and mantle flow, *Nature*, **430**, 167-173.
- Tarduno, J. A., et al. (2003), The Emperor Seamounts: Southward Motion of the Hawaiian Hotspot Plume in Earth's Mantle, *Science*, **301**, 1064-1069.
- Thorkelson, D. J. (1996), Subduction of diverging plates and the principles of slab window formation, *Tectonophysics*, **255**, 47-63.
- Thunell, R., and P. Belyea (1982), Neogene planktonic foraminiferal biogeography of the Atlantic Ocean, *Micropaleontology*, **28**, 381-398.
- Tikku, A. A., and S. C. Cande (1999), The oldest magnetic anomalies in the Australian-Antarctic Basin: Are they isochrons?, *Journal of Geophysical Research*, **104**, 661-677.
- Wessel, P. (2001), Global distribution of seamounts inferred from gridded Geosat/ERS-1 altimetry, *Journal of Geophysical Research*, **106**, 19431-19441.
- West, B. P., et al. (1994), Evidence for variable upper mantle temperature and crustal thickness in and near the Australian-Antarctic Discordance, *Earth Planet. Sci. Lett.*, **128**, 135-153.
- Wessel, P., and W. H. F. Smith (1998), New improved version of Generic Mapping Tools Released, *EOS Trans Amer Geophys Union*, **79**, 579.
- Woodcock, N. H. (1986), The role of strike-slip fault systems at plate boundaries, *Philos. Trans. R. Soc. London, Ser. A*, **317**, 13-29.

Appendix A

**Supplementary Material for Paper 1,
prepared for submission to Nature**

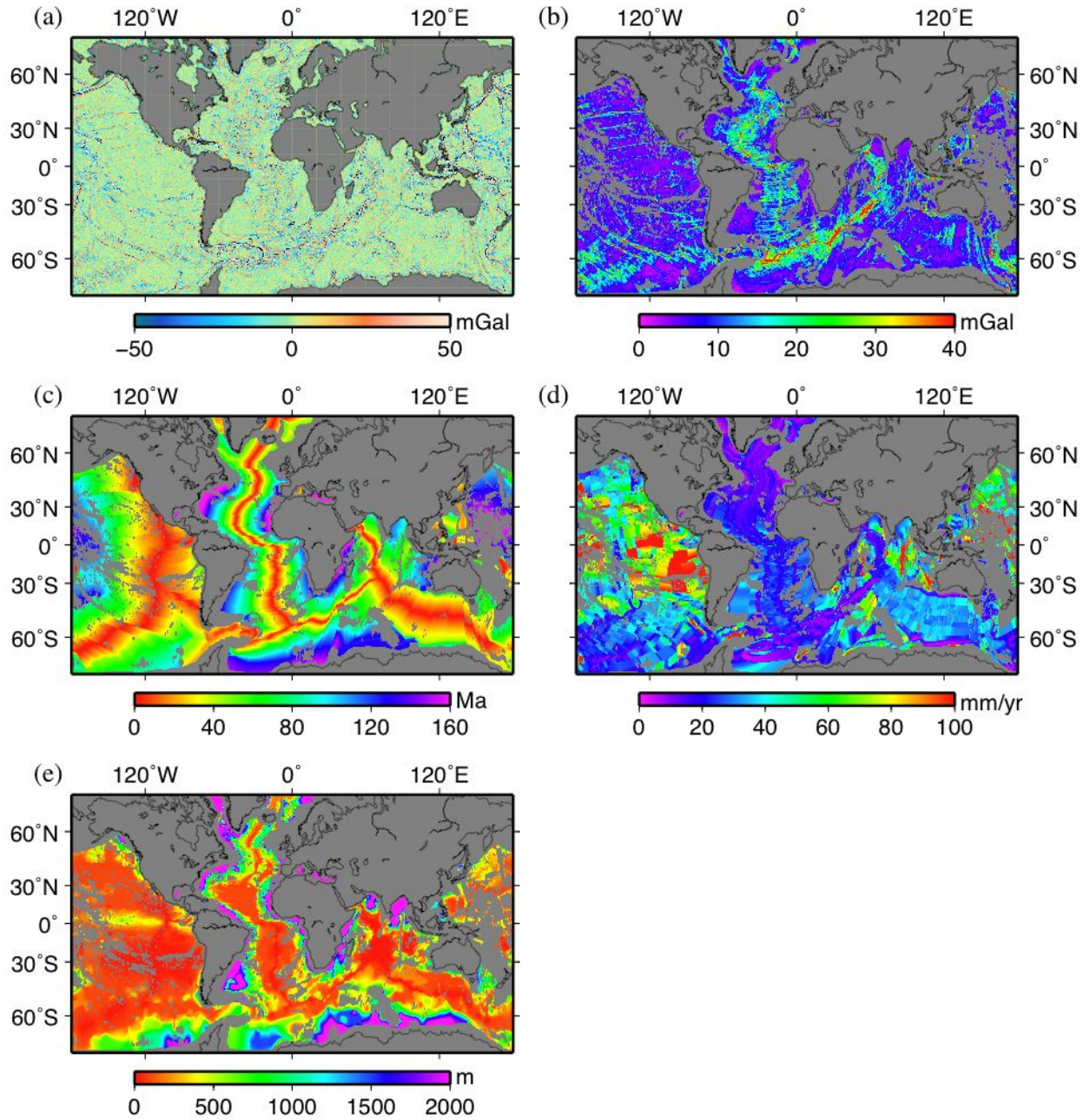


Figure A.1: Global marine 2-minute grids of (a) downward-continued marine gravity anomalies, (b) masked RMS-gravity roughness, (c) oceanic crustal age, (d) half-spreading rates, and (e) sediment thickness.

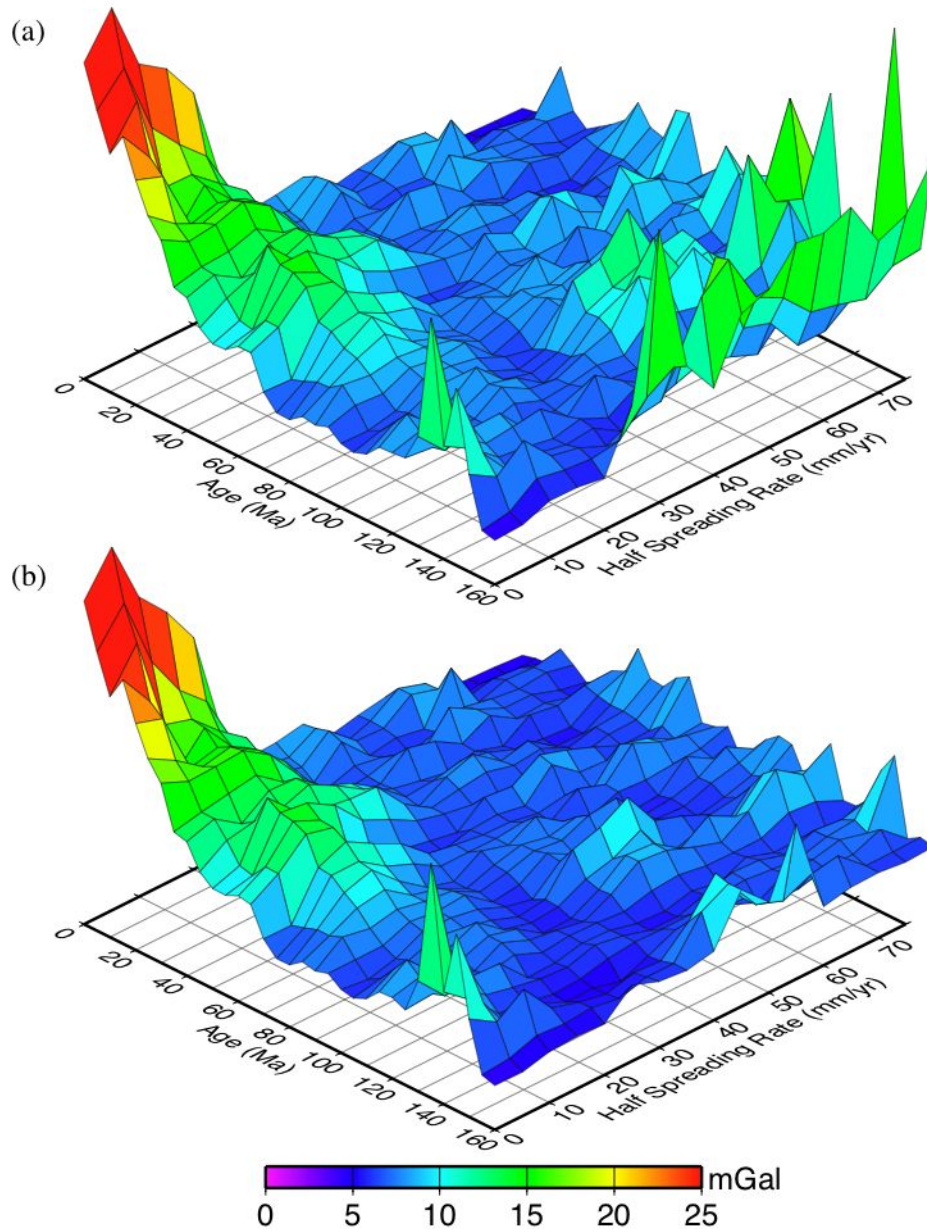


Figure A.2: (a) Unmasked, and (b) masked, gravity roughness as a function of crustal age and spreading half-rates, obtained by calculating the median roughness and its median absolute deviation in bins sized 5 m.y for crustal age, and 5 mm/yr for half-spreading rates.

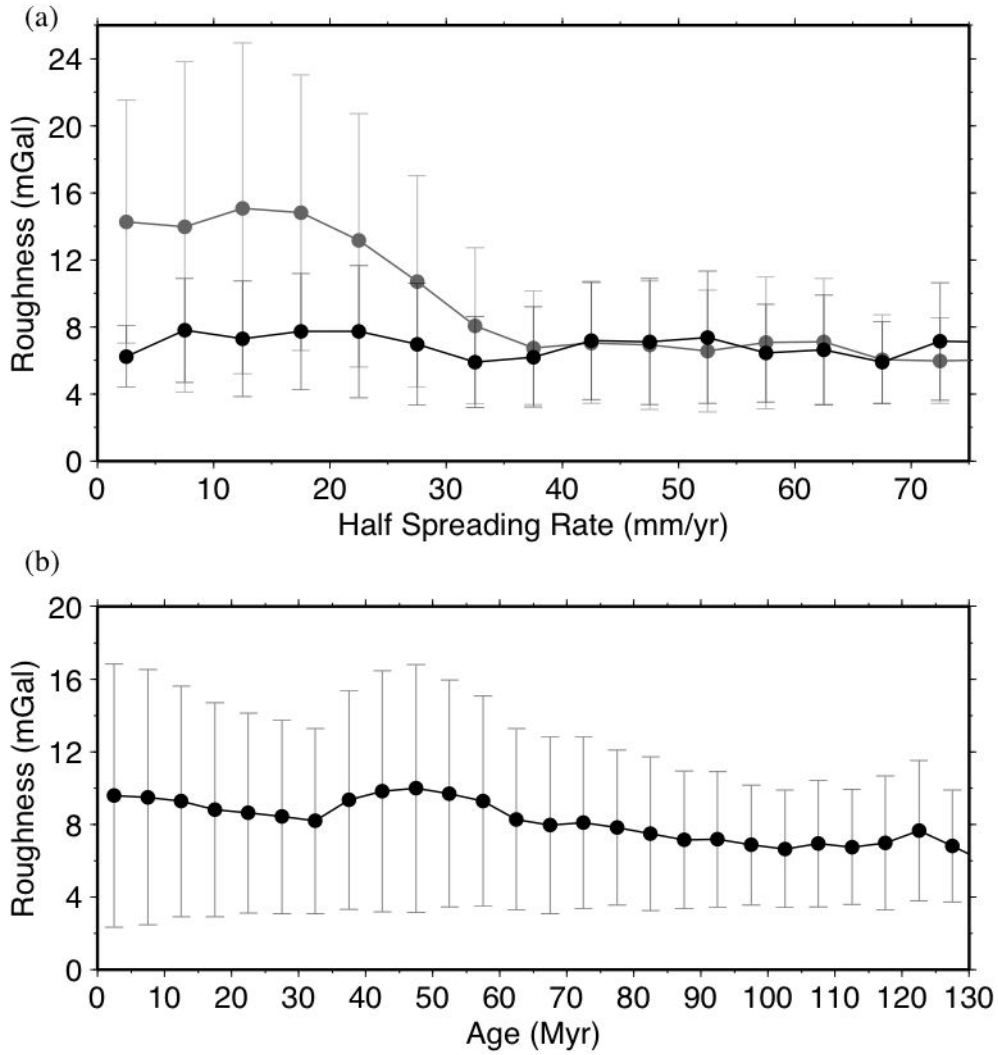


Figure A.3: Gravity roughness as a function of (a) half-spreading rate, for global crust aged 0-80 Myr (grey) and 80-130 Myr (black), and (b) crustal age. Note that basement roughness increases with slowing spreading rates for crust 0-80 Ma, but the same relationship does not exist for crust aged 80-130 Myr. However, no significant variation of roughness occurs with crustal age across all spreading rates. We suggest that most crust aged between 80 and 130 Myr exhibits relatively smooth basement irrespective of spreading rates due to underlying hot supercontinent-derived mantle.

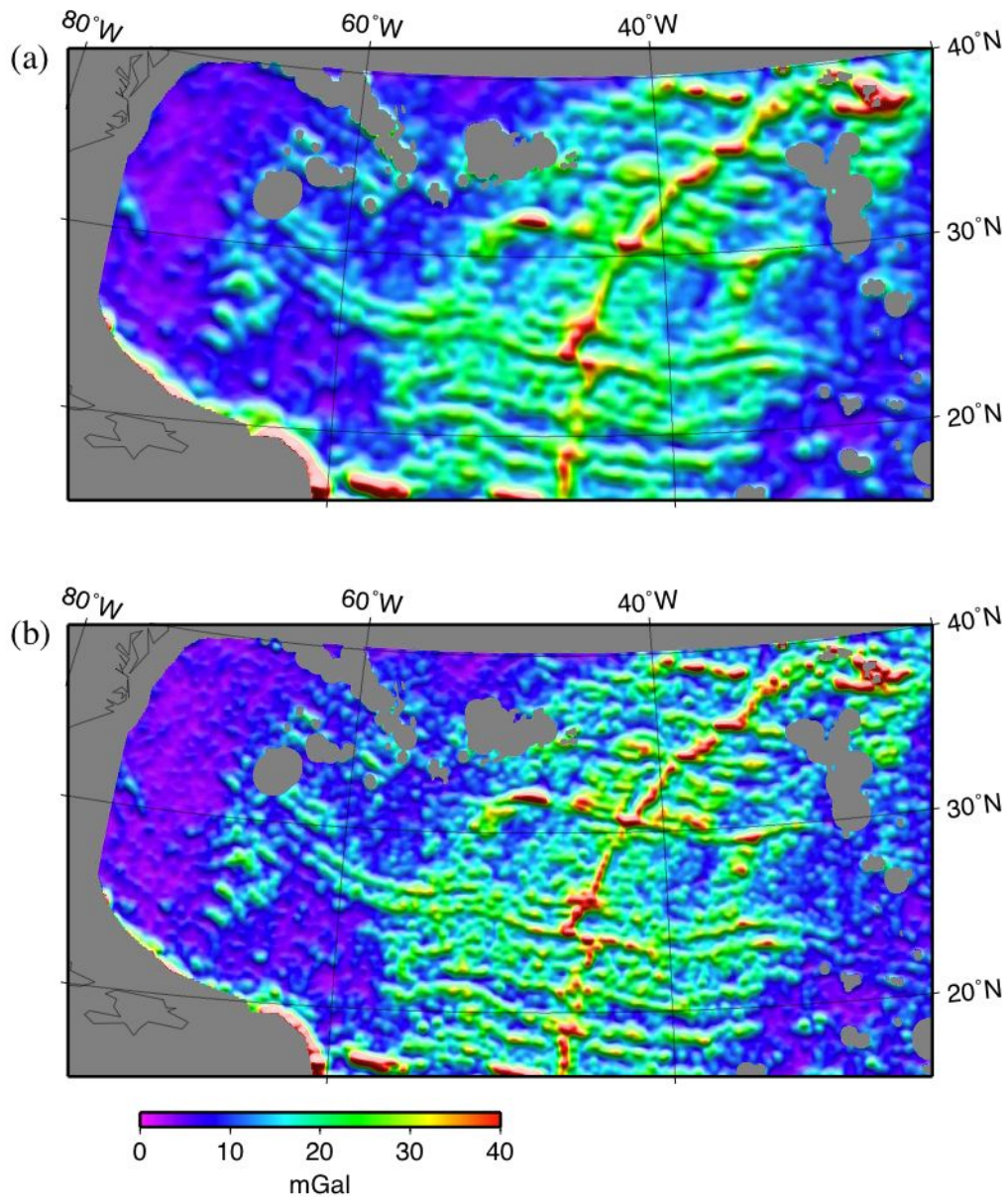


Figure A.4: Lambert equal area maps of gravity roughness calculated using a Gaussian filter of (a) 160 km, and (b) 100km.

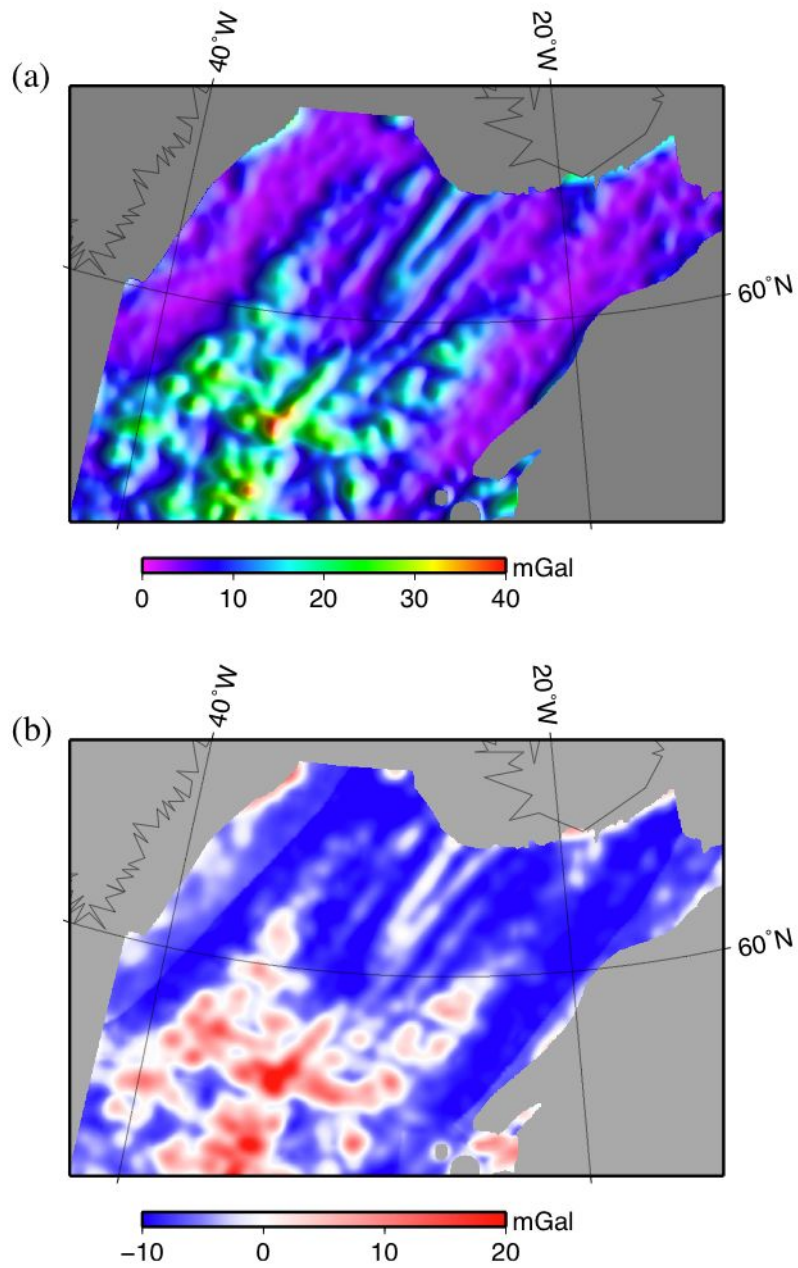


Figure A.5: North Atlantic (a) gravity roughness, and (b) residual gravity roughness. The residual roughness grid is computed using the gravity roughness grid, sediment thickness grid, and the spreading rate grid, which is based on constant spreading rates between isochrons.

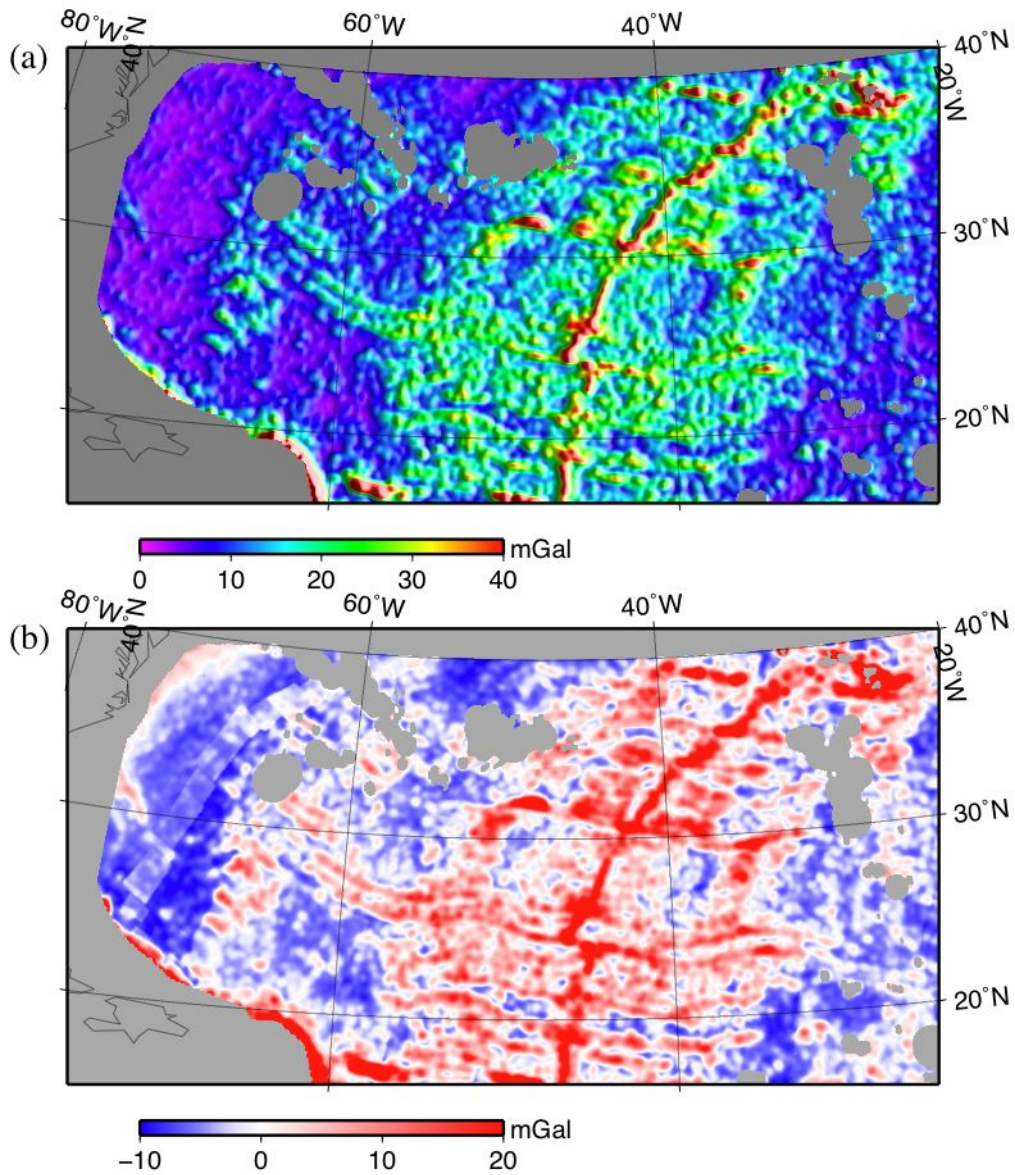


Figure A.6: Central Atlantic (a) gravity roughness, and (b) residual gravity roughness. The residual roughness grid is computed using the gravity roughness grid, sediment thickness grid, and the spreading rate grid, which is based on constant spreading between isochrons.

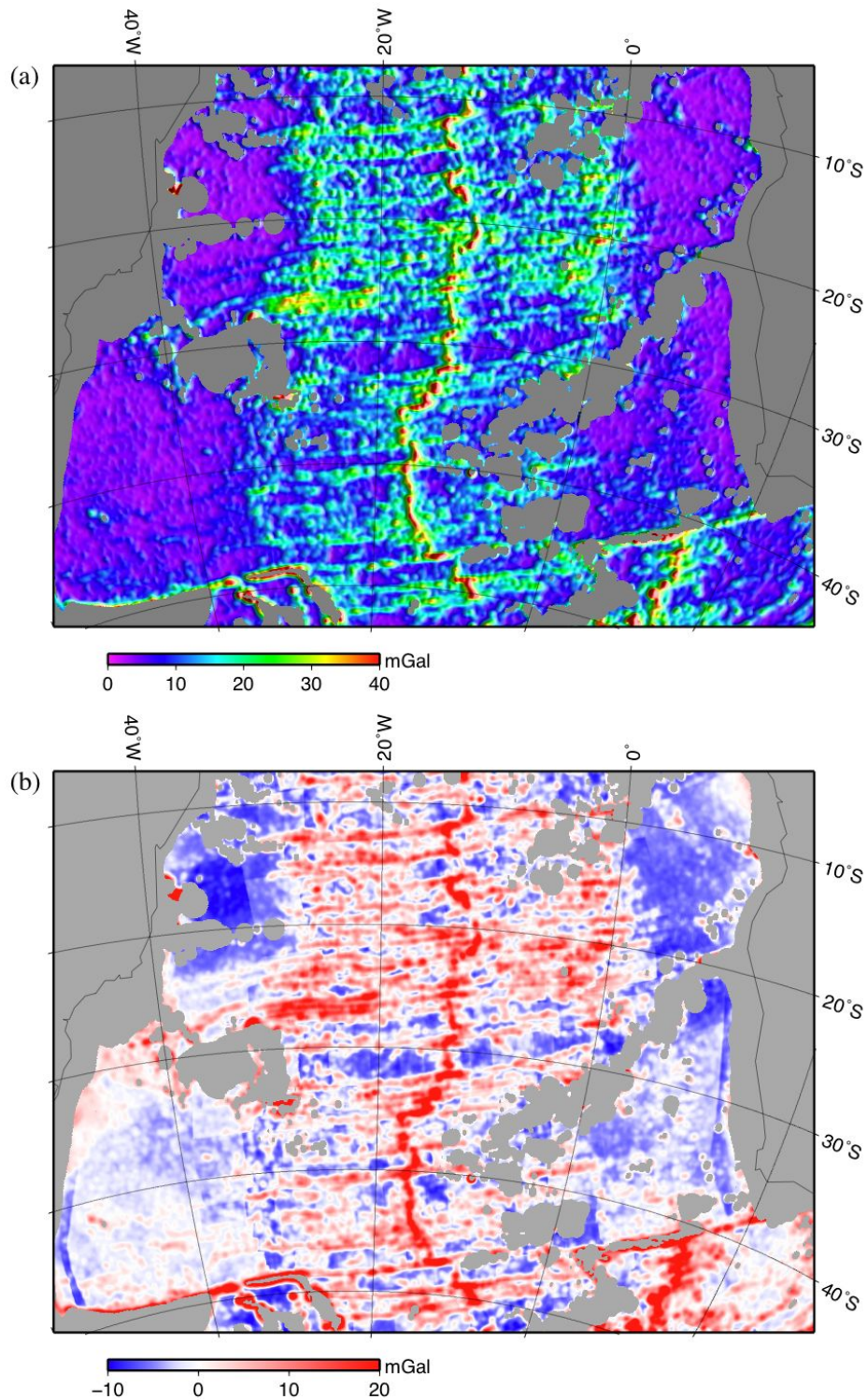


Figure A.7: South Atlantic (a) gravity roughness, and (b) residual gravity roughness. The residual roughness grid is computed using the gravity roughness grid, sediment thickness grid, and the spreading rate grid, which is based on constant spreading between isochrons.

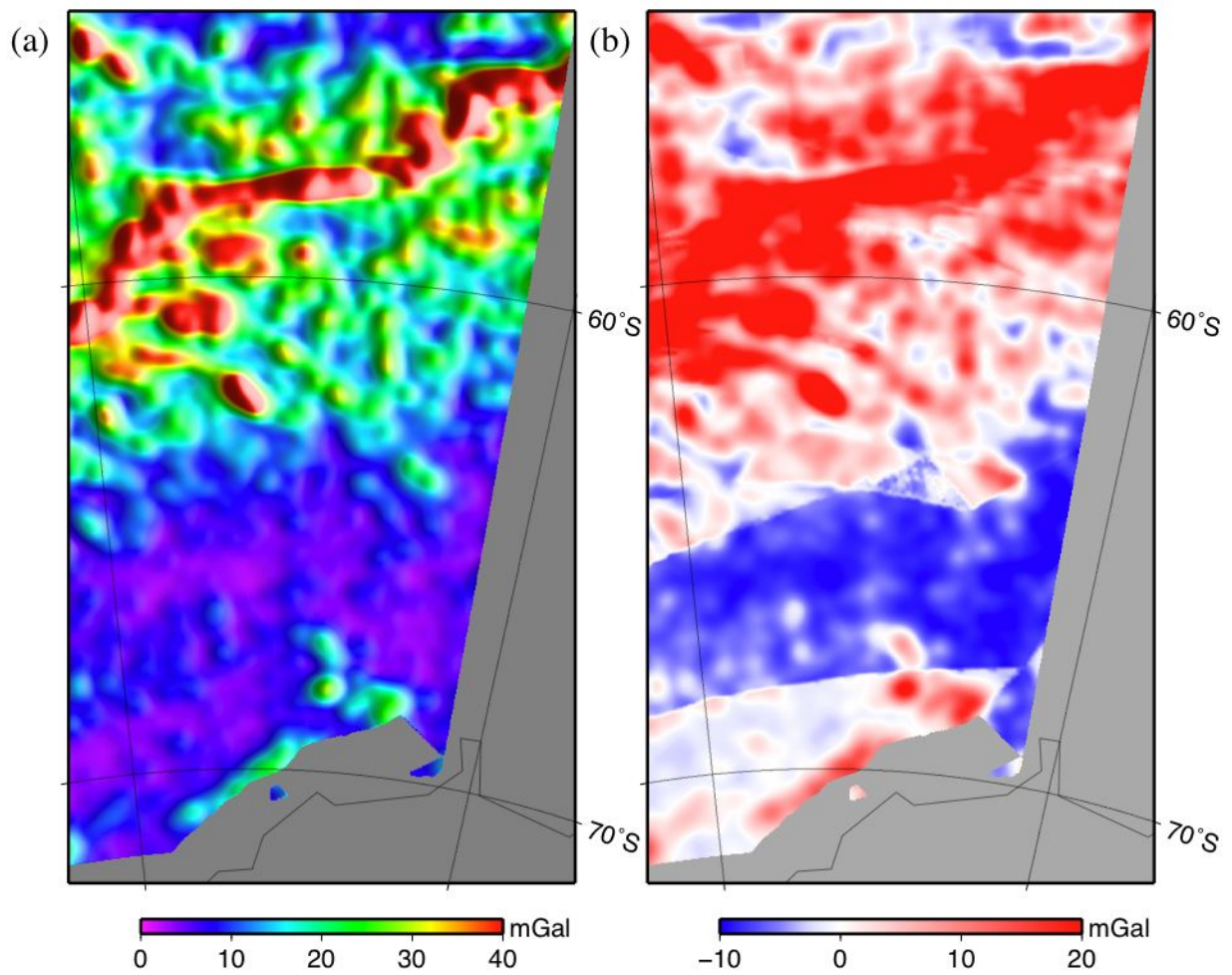


Figure A.8: South American-Antarctic Ridge (a) gravity roughness, and (b) residual gravity roughness. The residual roughness grid is computed using the gravity roughness grid, sediment thickness grid, and the spreading rate grid, which is based on constant spreading between isochrons.

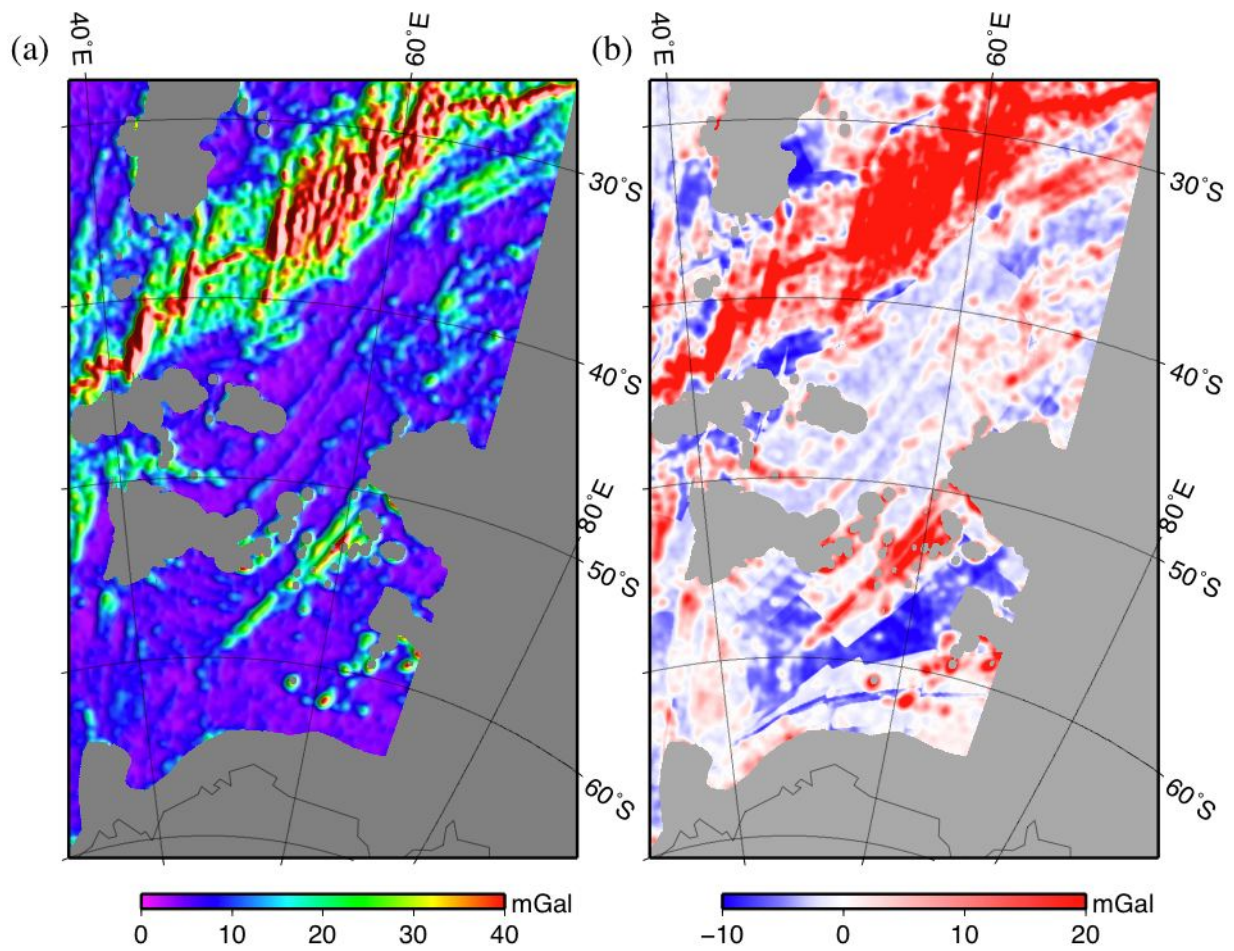


Figure A.9: Southwest Indian Ridge (a) gravity roughness, and (b) residual gravity roughness. The residual roughness grid is computed using the gravity roughness grid, sediment thickness grid, and the spreading rate grid, which is based on constant spreading between isochrons.

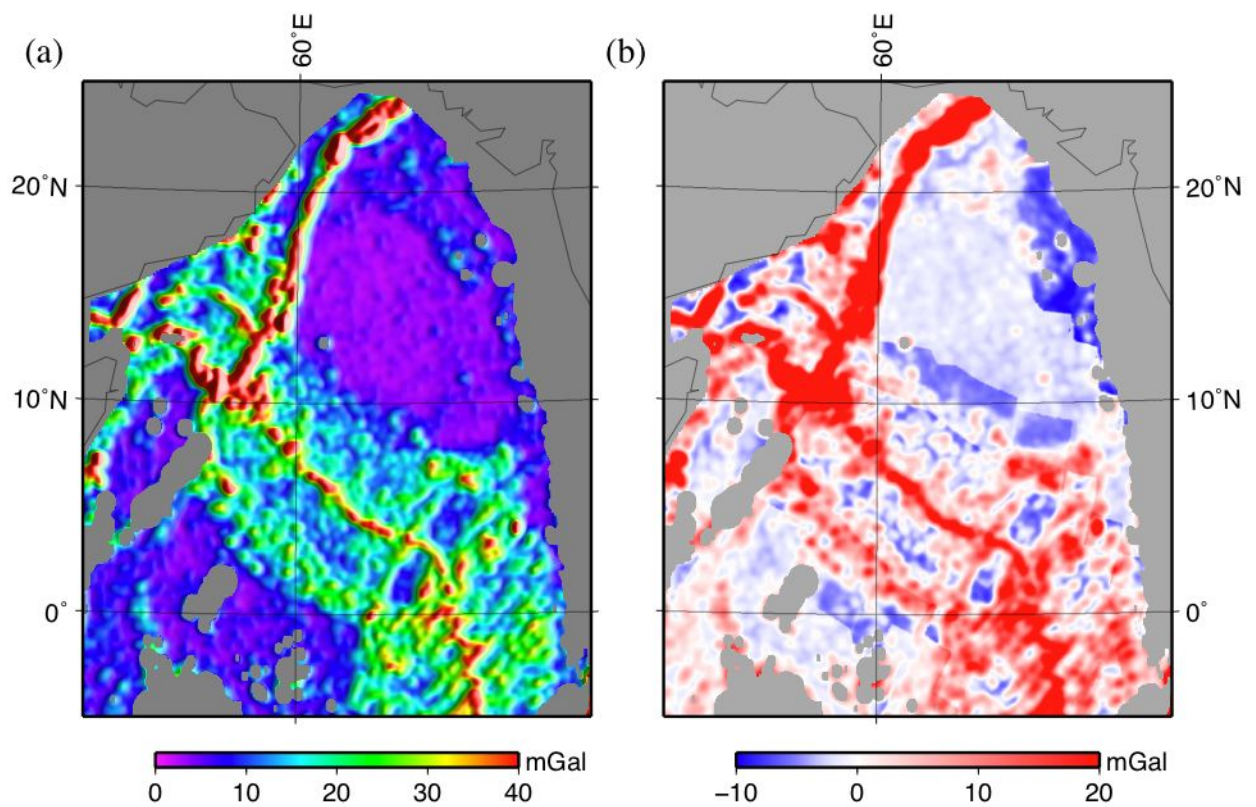


Figure A.10: Northwest Indian Ridge (a) gravity roughness, and (b) residual gravity roughness. The residual roughness grid is computed using the gravity roughness grid, sediment thickness grid, and the spreading rate grid, which is based on constant spreading between isochrons.

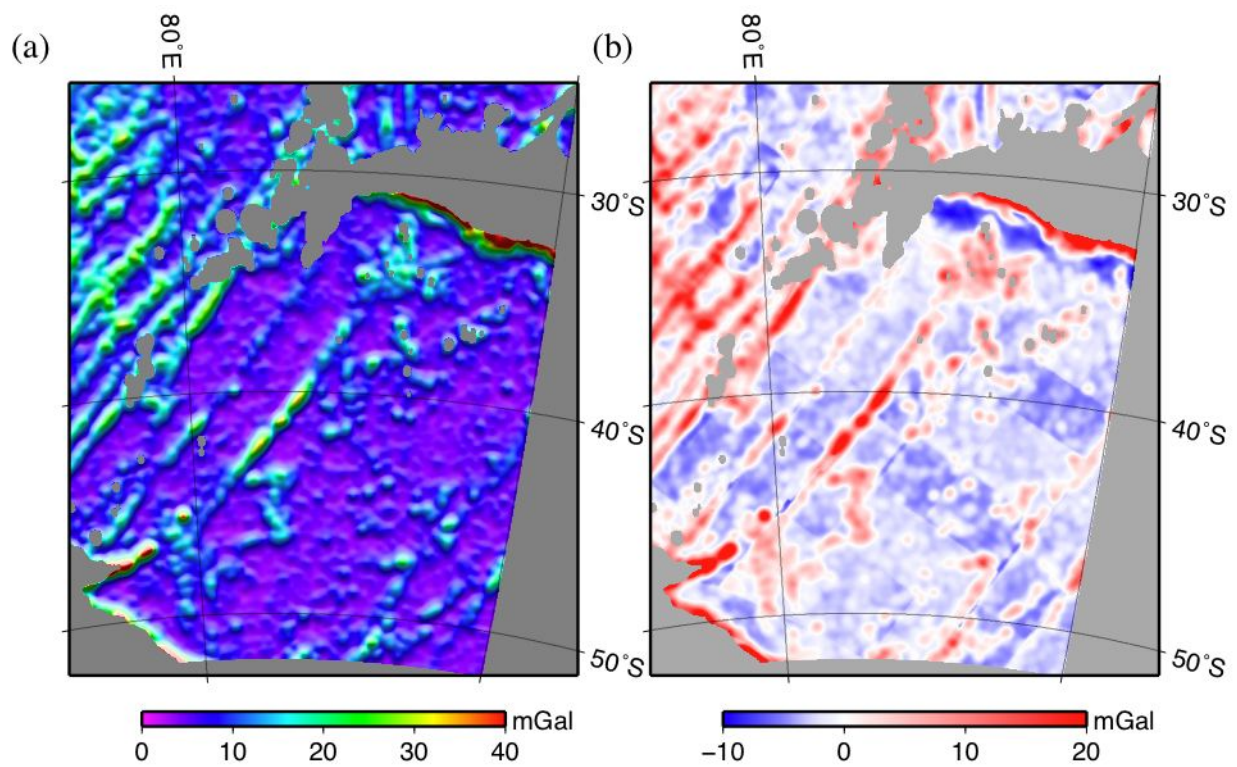


Figure A.11: Southeast Indian Ridge (a) gravity roughness, and (b) residual gravity roughness. The residual roughness grid is computed using the gravity roughness grid, sediment thickness grid, and the spreading rate grid, which is based on constant spreading between isochrons.

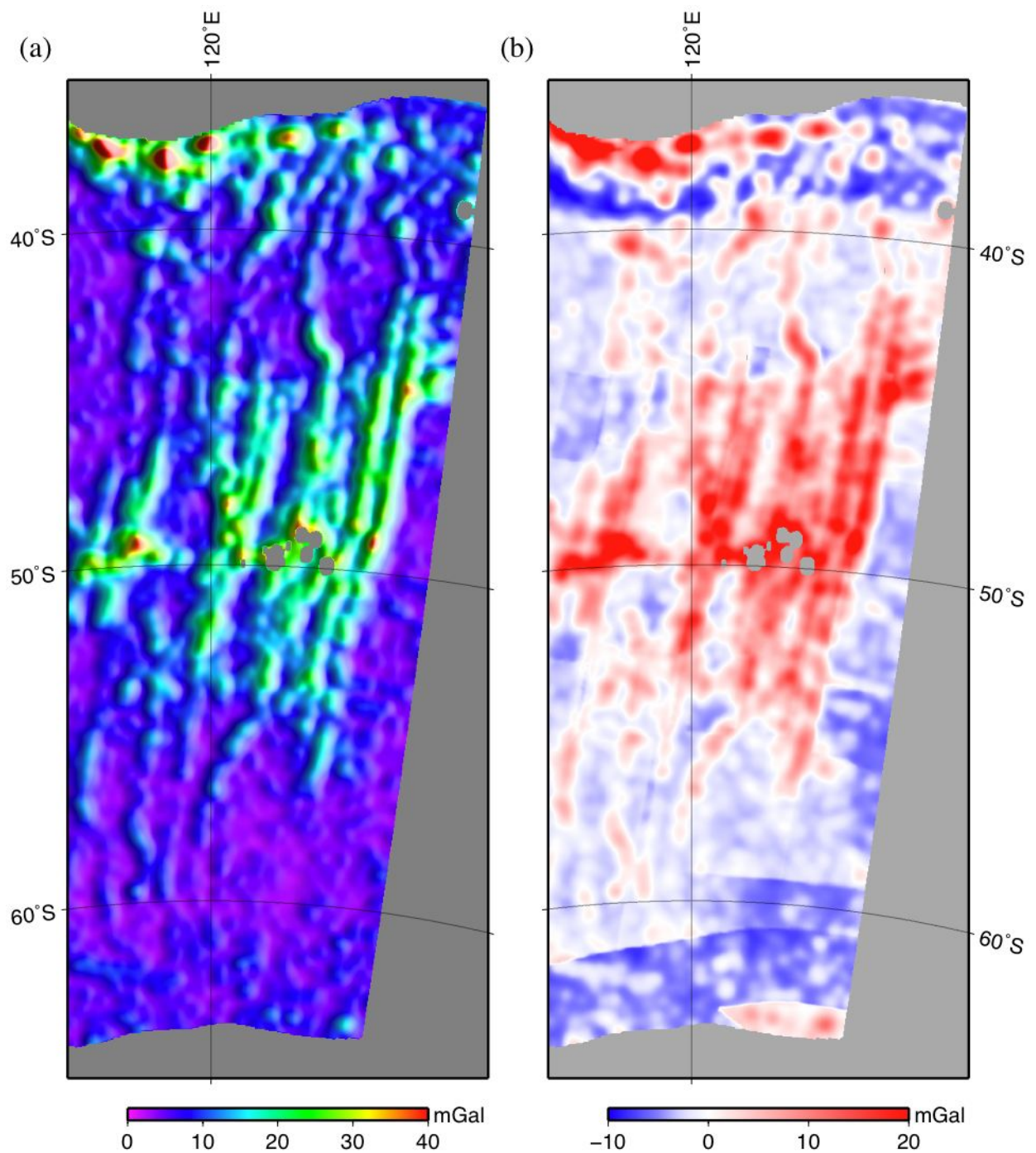


Figure A.12: Australian-Antarctic Discordance (a) gravity roughness, and (b) residual gravity roughness. The residual roughness grid is computed using the gravity roughness grid, sediment thickness grid, and the spreading rate grid, which is based on constant spreading between isochrons.

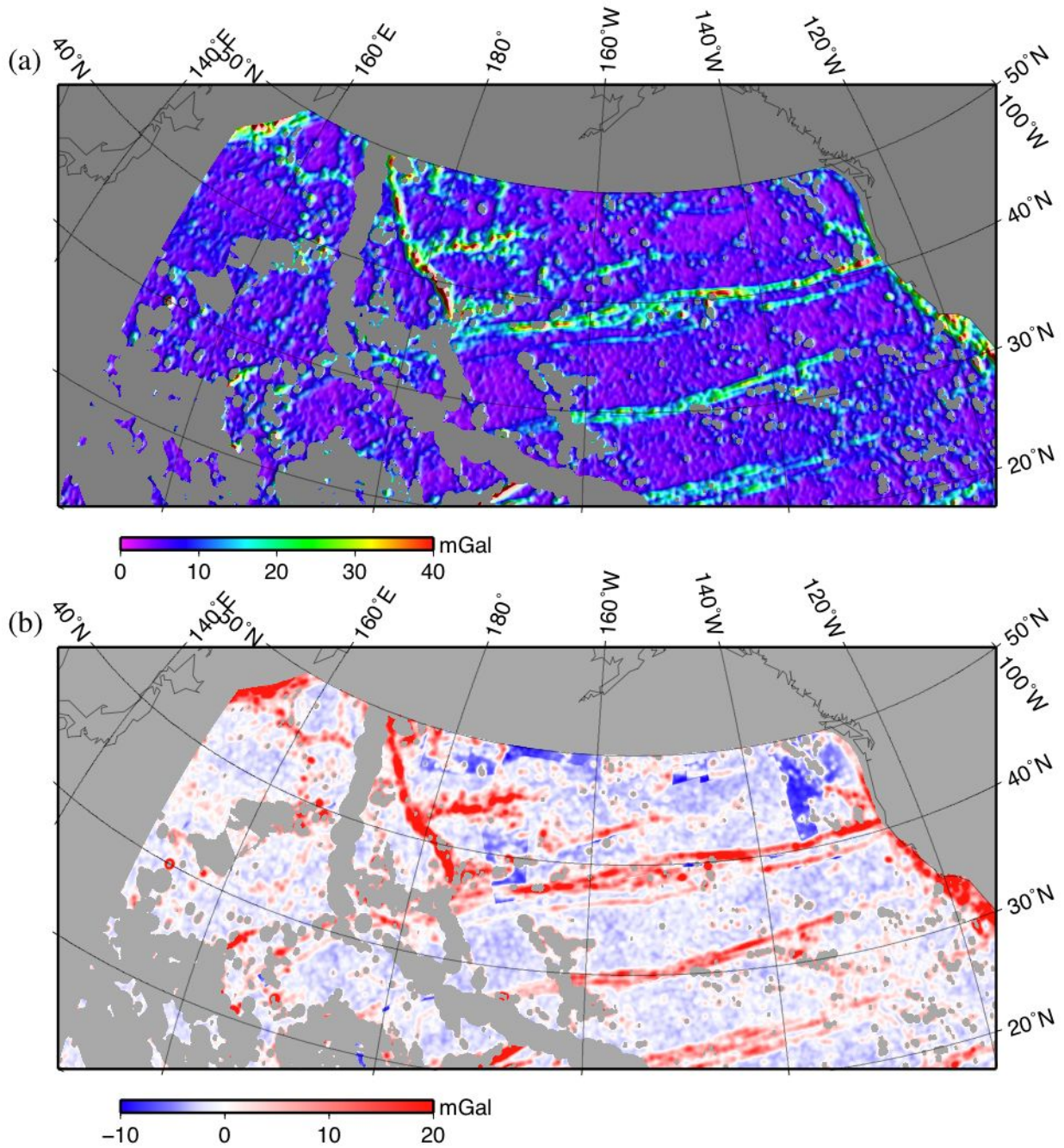


Figure A.13: North Pacific (a) gravity roughness, and (b) residual gravity roughness. The residual roughness grid is computed using the gravity roughness grid, sediment thickness grid, and the spreading rate grid, which is based on constant spreading between isochrons.

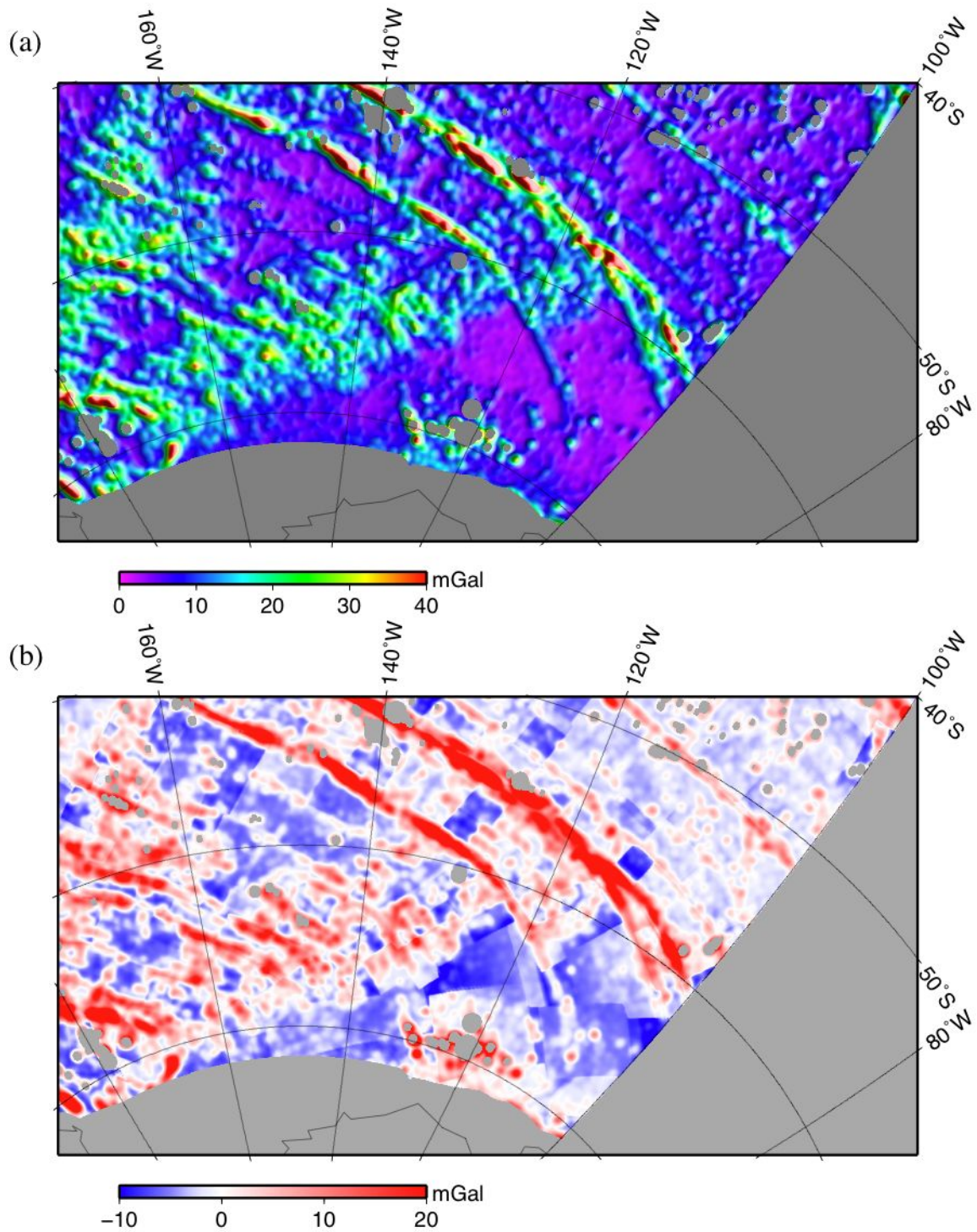


Figure A.14: South Pacific (a) gravity roughness, and (b) residual gravity roughness. The residual roughness grid is computed using the gravity roughness grid, sediment thickness grid, and the spreading rate grid, which is based on constant spreading between isochrons.

Appendix B

Supplementary Online Material for Paper 2, Whittaker et al. Science (2007)

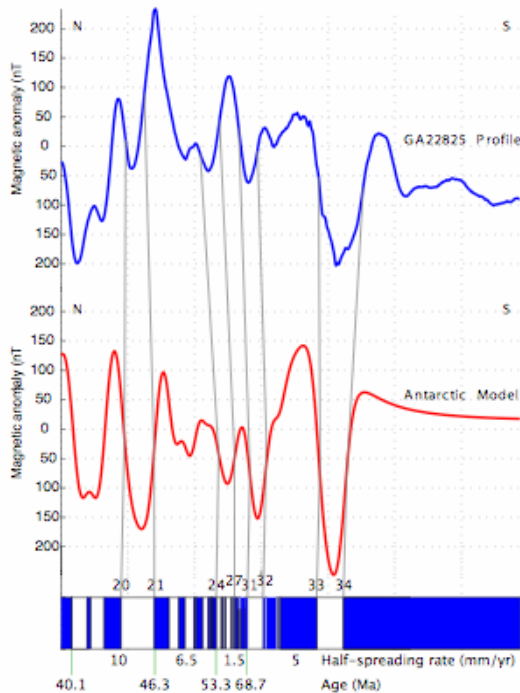


Figure S1: Spreading rate model from Tikku and Cande (*S1*) for the Southeast Indian Ridge, profile GA-22825 on the East Antarctic ridge flank (see Figure 1 for location). Magnetic anomalies identified on the model are 20o, 21y, 24o, 27y, 31o, 32y, 33o and 34y ('y' 'o' – young and old sides respectively of the magnetic anomaly chron eg 20o means the older side of magnetic anomaly chron 20) following the identification method of Tikku and Cande (*S1*). Synthetic magnetic anomaly profile computed using Modmag (*S2*) with the following input model parameters; top of magnetic source layer is 6.0 km, bottom of magnetic source layer is 6.5 km, remanent inclination = -81.2° , and remanent declination = 0.0° . Dashed vertical gridlines are at 50 km along profile spacing.

Table S1: Fracture zone identifications.

Margin	Fault	Lat	Long	Chron
Ant	1	-59.1647	107.5773	18
Ant	2	-59.1165	120.8755	18
Ant	1	-61.6597	106.1909	20
Ant	2	-61.3283	120.0833	20
Ant	1	-61.8450	106.1198	21
Ant	2	-61.5135	120.0367	21
Ant	1	-62.1521	106.6530	24
Ant	2	-61.8408	120.3321	24
Ant	1	-62.2766	106.9308	27
Ant	2	-61.9770	120.5521	27
Ant	1	-62.3716	107.1041	31
Ant	2	-62.1355	120.8298	31
Ant	1	-62.5505	107.4297	32
Ant	2	-62.2206	120.9898	32
Ant	1	-62.7386	107.7851	33
Ant	2	-62.5629	121.6207	33
Ant	1	-62.9884	108.2527	34
Ant	2	-62.9762	122.3361	34
Ant	1	-63.4574	108.9992	QZB
Ant	2	-63.6792	123.6803	QZB
Aus	1	-40.0173	117.2496	18
Aus	2	-39.6235	125.7909	18
Aus	1	-38.3646	117.8362	20
Aus	2	-37.6723	126.1553	20
Aus	1	-38.2315	117.8895	21
Aus	2	-37.5132	126.1508	21
Aus	1	-37.8522	117.4595	24
Aus	2	-37.1264	125.9286	24
Aus	1	-37.7394	117.3173	27
Aus	2	-36.9768	125.8042	27
Aus	1	-37.6546	117.1929	31
Aus	2	-36.8769	125.7020	31
Aus	1	-37.5981	117.1218	32
Aus	2	-36.7912	125.6043	32
Aus	1	-37.4565	116.9263	33
Aus	2	-36.5191	125.2799	33
Aus	1	-37.3289	116.8018	34
Aus	2	-36.2928	124.9911	34
Aus	1	-37.2194	116.6720	QZB
Aus	2	-36.0478	124.6912	QZB

Table S2: Magnetic anomaly identifications. Magnetic anomaly identifications were made using new high quality magnetic data in the Bruce Rise area (90°-115°E) collected by Russian Antarctic Expeditions 49 and 50 in 2004-2005. The total magnetic field was recorded in these surveys by a differential magnetometer to 0.01 nT accuracy. New magnetic anomaly identifications were also made for data collected during Geoscience Australia cruises 228 and 229 (S3-S6). Our new identifications were integrated with earlier identifications of Tikku and Cande (*SI*).

Side	Chron	Latitude	Longitude	Source
Ant	C20o	-57.7970	88.2870	Tikku and Cande (<i>SI</i>)
Ant	C20o	-58.2320	89.7220	Tikku and Cande (<i>SI</i>)
Ant	C20o	-58.6640	90.0560	Tikku and Cande (<i>SI</i>)
Ant	C20o	-58.8590	90.4310	Tikku and Cande (<i>SI</i>)
Ant	C20o	-58.9560	90.7470	Tikku and Cande (<i>SI</i>)
Ant	C20o	-59.3280	91.5680	Tikku and Cande (<i>SI</i>)
Ant	C20o	-59.4930	92.1130	Tikku and Cande (<i>SI</i>)
Ant	C20o	-59.5570	92.3590	Tikku and Cande (<i>SI</i>)
Ant	C20o	-60.4030	101.2300	Tikku and Cande (<i>SI</i>)
Ant	C20o	-60.6130	102.3440	Tikku and Cande (<i>SI</i>)
Ant	C20o	-61.5240	104.0334	GA-22815
Ant	C20o	-61.3460	104.1890	Tikku and Cande (<i>SI</i>)
Ant	C20o	-61.4390	104.6260	Tikku and Cande (<i>SI</i>)
Ant	C20o	-61.6340	105.2370	Tikku and Cande (<i>SI</i>)
Ant	C20o	-61.7040	105.6330	Tikku and Cande (<i>SI</i>)
Ant	C20o	-61.7041	105.7170	GA-22917
Ant	C20o	-61.7447	107.3997	GA-22817
Ant	C20o	-61.6973	108.1544	RAE-5003
Ant	C20o	-61.6420	109.0840	GA-22915
Ant	C20o	-61.4770	110.7667	GA-22818
Ant	C20o	-61.3930	112.0200	Tikku and Cande (<i>SI</i>)
Ant	C20o	-61.3946	112.4500	GA-22913
Ant	C20o	-61.4040	113.2790	Tikku and Cande (<i>SI</i>)
Ant	C20o	-61.4416	114.1371	GA-22819
Ant	C20o	-61.4870	114.5000	Tikku and Cande (<i>SI</i>)
Ant	C20o	-61.5516	115.8160	GA-22912
Ant	C20o	-61.5200	117.0000	Tikku and Cande (<i>SI</i>)
Ant	C20o	-61.4980	117.2800	Tikku and Cande (<i>SI</i>)
Ant	C20o	-61.4912	117.4998	GA-22820
Ant	C20o	-61.4770	118.0000	Tikku and Cande (<i>SI</i>)
Ant	C20o	-61.4346	119.1839	GA-22911
Ant	C20o	-61.3600	120.1180	Tikku and Cande (<i>SI</i>)
Ant	C20o	-61.3620	120.1790	Tikku and Cande (<i>SI</i>)
Ant	C20o	-61.3200	120.7120	Tikku and Cande (<i>SI</i>)
Ant	C20o	-61.2887	120.8676	GA-22910
Ant	C20o	-61.2930	121.0960	Tikku and Cande (<i>SI</i>)
Ant	C20o	-61.2682	122.5490	GA-22908
Ant	C20o	-61.2860	122.7110	Tikku and Cande (<i>SI</i>)
Ant	C20o	-61.3334	124.2350	GA-22909
Ant	C20o	-61.3190	124.9930	Tikku and Cande (<i>SI</i>)
Ant	C20o	-61.3945	125.9160	GA-22823
Ant	C20o	-61.4340	126.3350	Tikku and Cande (<i>SI</i>)
Ant	C20o	-61.4280	126.6880	Tikku and Cande (<i>SI</i>)
Ant	C20o	-61.4323	127.6003	GA-22824
Ant	C20o	-61.4330	128.5460	Tikku and Cande (<i>SI</i>)
Ant	C20o	-61.3881	129.2833	GA-22825
Ant	C20o	-61.4080	129.8450	Tikku and Cande (<i>SI</i>)
Ant	C20o	-61.2940	131.9830	Tikku and Cande (<i>SI</i>)
Ant	C20o	-61.2810	132.0170	Tikku and Cande (<i>SI</i>)
Ant	C20o	-60.9750	134.8390	Tikku and Cande (<i>SI</i>)
Ant	C20o	-60.9900	136.5670	Tikku and Cande (<i>SI</i>)
Ant	C20o	-60.9580	137.0720	Tikku and Cande (<i>SI</i>)

Aus	C20o	-31.0000	93.0870	Tikku and Cande (SI)
Aus	C20o	-31.0440	93.3390	Tikku and Cande (SI)
Aus	C20o	-31.6860	94.9560	Tikku and Cande (SI)
Aus	C20o	-32.5060	97.6070	Tikku and Cande (SI)
Aus	C20o	-33.2610	101.1840	Tikku and Cande (SI)
Aus	C20o	-33.2610	101.5040	Tikku and Cande (SI)
Aus	C20o	-35.8730	105.0720	Tikku and Cande (SI)
Aus	C20o	-36.3480	105.9530	Tikku and Cande (SI)
Aus	C20o	-36.6410	106.7610	Tikku and Cande (SI)
Aus	C20o	-37.0340	107.3980	Tikku and Cande (SI)
Aus	C20o	-37.2080	108.0800	Tikku and Cande (SI)
Aus	C20o	-37.4380	108.6440	Tikku and Cande (SI)
Aus	C20o	-37.6120	109.2650	Tikku and Cande (SI)
Aus	C20o	-37.6700	109.6900	Tikku and Cande (SI)
Aus	C20o	-37.5390	110.0540	Tikku and Cande (SI)
Aus	C20o	-37.5440	110.2740	Tikku and Cande (SI)
Aus	C20o	-37.5500	110.3550	Tikku and Cande (SI)
Aus	C20o	-37.4700	111.6610	Tikku and Cande (SI)
Aus	C20o	-37.4500	111.7460	Tikku and Cande (SI)
Aus	C20o	-37.4780	112.0760	Tikku and Cande (SI)
Aus	C20o	-37.3130	113.1890	Tikku and Cande (SI)
Aus	C20o	-37.1650	113.8050	Tikku and Cande (SI)
Aus	C20o	-37.2160	114.1170	Tikku and Cande (SI)
Aus	C20o	-37.2620	114.5250	Tikku and Cande (SI)
Aus	C20o	-37.6600	115.3740	Tikku and Cande (SI)
Aus	C20o	-38.0390	115.9810	Tikku and Cande (SI)
Aus	C20o	-38.2980	117.0870	Tikku and Cande (SI)
Aus	C20o	-38.4360	118.1340	Tikku and Cande (SI)
Aus	C20o	-38.4370	118.4170	Tikku and Cande (SI)
Aus	C20o	-38.3480	118.8260	Tikku and Cande (SI)
Aus	C20o	-38.1950	119.2410	Tikku and Cande (SI)
Aus	C20o	-37.8520	122.6020	Tikku and Cande (SI)
Aus	C20o	-37.8500	122.7230	Tikku and Cande (SI)
Aus	C20o	-37.7390	125.6480	Tikku and Cande (SI)
Aus	C20o	-37.7100	125.7580	Tikku and Cande (SI)
Aus	C20o	-37.6560	126.7140	Tikku and Cande (SI)
Aus	C20o	-37.6490	128.0040	Tikku and Cande (SI)
Aus	C20o	-37.9480	130.6820	Tikku and Cande (SI)
Aus	C20o	-37.8860	131.2260	Tikku and Cande (SI)
Aus	C20o	-37.8990	131.5000	Tikku and Cande (SI)
Aus	C20o	-37.9800	132.1130	Tikku and Cande (SI)
Aus	C20o	-38.0000	132.6360	Tikku and Cande (SI)
Aus	C20o	-37.9980	132.7980	Tikku and Cande (SI)
Aus	C20o	-37.8010	134.1210	Tikku and Cande (SI)
Aus	C20o	-37.8810	134.5960	Tikku and Cande (SI)
Aus	C20o	-37.8400	135.2130	Tikku and Cande (SI)
Ant	C21y	-60.6680	102.0110	Tikku and Cande (SI)
Ant	C21y	-61.6581	104.0334	GA-22815
Ant	C21y	-61.5380	104.2450	Tikku and Cande (SI)
Ant	C21y	-61.7510	104.6740	Tikku and Cande (SI)
Ant	C21y	-61.7320	104.9270	Tikku and Cande (SI)
Ant	C21y	-61.8218	105.6490	GA-22917
Ant	C21y	-61.8470	105.7550	Tikku and Cande (SI)
Ant	C21y	-61.8440	107.3999	GA-22817
Ant	C21y	-61.8148	108.1644	RAE-5003
Ant	C21y	-61.7554	109.0840	GA-22915
Ant	C21y	-61.5688	110.7667	GA-22828

Ant	C21y	-61.5800	112.0000	Tikku and Cande (SI)
Ant	C21y	-61.5420	112.4510	GA-22913
Ant	C21y	-61.5020	113.1620	Tikku and Cande (SI)
Ant	C21y	-61.5897	114.1387	GA-22819
Ant	C21y	-61.6300	114.5000	Tikku and Cande (SI)
Ant	C21y	-61.7044	115.4640	RAE-50067
Ant	C21y	-61.8500	115.8900	GA-22912
Ant	C21y	-61.6660	117.0000	Tikku and Cande (SI)
Ant	C21y	-61.6299	117.4998	GA-22820
Ant	C21y	-61.6200	118.0000	Tikku and Cande (SI)
Ant	C21y	-61.6140	118.0640	Tikku and Cande (SI)
Ant	C21y	-61.5632	119.1830	GA-22911
Ant	C21y	-61.5090	120.1100	Tikku and Cande (SI)
Ant	C21y	-61.4540	120.5760	Tikku and Cande (SI)
Ant	C21y	-61.4121	120.8670	GA-22910
Ant	C21y	-61.4070	121.0860	Tikku and Cande (SI)
Ant	C21y	-61.3860	122.4490	Tikku and Cande (SI)
Ant	C21y	-61.3850	122.5499	GA-22908
Ant	C21y	-61.4453	124.2330	GA-22822
Ant	C21y	-61.4690	124.7480	Tikku and Cande (SI)
Ant	C21y	-61.5120	125.9161	GA-22823
Ant	C21y	-61.5500	126.4010	Tikku and Cande (SI)
Ant	C21y	-61.5460	126.7150	Tikku and Cande (SI)
Ant	C21y	-61.5703	127.6004	GA-22824
Ant	C21y	-61.5910	127.7850	Tikku and Cande (SI)
Ant	C21y	-61.5750	128.2440	Tikku and Cande (SI)
Ant	C21y	-61.5269	129.2833	GA-22825
Ant	C21y	-61.5530	129.8310	Tikku and Cande (SI)
Ant	C21y	-61.4760	131.9830	Tikku and Cande (SI)
Ant	C21y	-61.4790	132.0130	Tikku and Cande (SI)
Ant	C21y	-61.2410	134.2200	Tikku and Cande (SI)
Ant	C21y	-61.2030	136.5670	Tikku and Cande (SI)
Ant	C21y	-61.1450	137.0000	Tikku and Cande (SI)
Ant	C21y	-61.1930	137.5730	Tikku and Cande (SI)
Ant	C21y	-61.2030	138.3860	Tikku and Cande (SI)
Ant	C21y	-61.1200	138.5720	Tikku and Cande (SI)
Ant	C21y	-61.1160	138.7760	Tikku and Cande (SI)
Ant	C21y	-61.1280	140.2090	Tikku and Cande (SI)
Aus	C21y	-37.7060	122.5950	Tikku and Cande (SI)
Aus	C21y	-37.7630	122.8490	Tikku and Cande (SI)
Aus	C21y	-37.6140	125.5840	Tikku and Cande (SI)
Aus	C21y	-37.5700	125.8730	Tikku and Cande (SI)
Aus	C21y	-37.4840	126.6750	Tikku and Cande (SI)
Aus	C21y	-37.4570	127.9830	Tikku and Cande (SI)
Aus	C21y	-37.5570	129.4100	Tikku and Cande (SI)
Aus	C21y	-37.7550	130.7100	Tikku and Cande (SI)
Aus	C21y	-37.7290	131.5080	Tikku and Cande (SI)
Aus	C21y	-37.7420	131.5970	Tikku and Cande (SI)
Aus	C21y	-37.8020	132.1110	Tikku and Cande (SI)
Aus	C21y	-37.8290	132.5240	Tikku and Cande (SI)
Aus	C21y	-37.8250	132.3630	Tikku and Cande (SI)
Aus	C21y	-37.8290	132.7990	Tikku and Cande (SI)
Aus	C21y	-37.7110	134.2200	Tikku and Cande (SI)
Aus	C21y	-37.6650	134.6450	Tikku and Cande (SI)
Aus	C21y	-37.6970	135.2940	Tikku and Cande (SI)
Ant	C24o	-61.7294	104.0333	GA-22815
Ant	C24o	-61.9408	104.8557	RAE-5002
Ant	C24o	-61.9959	105.0869	GA-22917
Ant	C24o	-62.1650	107.3013	GA-22817
Ant	C24o	-61.9571	108.1773	RAE-5003

Ant	C24o	-61.9483	109.0840	GA-22915
Ant	C24o	-61.8290	110.7668	GA-22818
Ant	C24o	-61.7760	112.0000	Tikku and Cande (SI)
Ant	C24o	-61.8400	112.5630	GA-22913
Ant	C24o	-61.8820	112.7130	Tikku and Cande (SI)
Ant	C24o	-61.7846	113.0221	RAE-5005
Ant	C24o	-61.9566	114.1430	GA-22819
Ant	C24o	-62.0260	114.5000	Tikku and Cande (SI)
Ant	C24o	-61.9847	114.8197	RAE-5006
Ant	C24o	-61.9821	115.4475	RAE-50067
Ant	C24o	-62.0221	116.1480	GA-22912
Ant	C24o	-62.0240	117.0000	Tikku and Cande (SI)
Ant	C24o	-61.9152	117.4999	GA-22820
Ant	C24o	-62.0230	118.0000	Tikku and Cande (SI)
Ant	C24o	-61.8096	119.1840	GA-22911
Ant	C24o	-61.8820	119.3990	Tikku and Cande (SI)
Ant	C24o	-61.8940	120.1650	Tikku and Cande (SI)
Ant	C24o	-61.8529	120.8680	GA-22910
Ant	C24o	-61.7660	121.1080	Tikku and Cande (SI)
Ant	C24o	-61.7040	121.6960	Tikku and Cande (SI)
Ant	C24o	-61.6004	122.5500	GA-22908
Ant	C24o	-61.8740	124.0860	Tikku and Cande (SI)
Ant	C24o	-61.8283	124.2332	GA-22822
Ant	C24o	-61.9673	125.9161	GA-22823
Ant	C24o	-61.9490	126.6500	Tikku and Cande (SI)
Ant	C24o	-61.9030	126.8300	Tikku and Cande (SI)
Ant	C24o	-61.9140	126.8980	Tikku and Cande (SI)
Ant	C24o	-61.9568	127.6001	GA-22824
Ant	C24o	-61.9700	127.7620	Tikku and Cande (SI)
Ant	C24o	-61.9039	129.2832	GA-22825
Ant	C24o	-61.8630	129.7810	Tikku and Cande (SI)
Ant	C24o	-61.9500	131.9760	Tikku and Cande (SI)
Ant	C24o	-61.9850	132.0330	Tikku and Cande (SI)
Ant	C24o	-61.7200	134.6900	Tikku and Cande (SI)
Ant	C24o	-61.6480	135.6690	Tikku and Cande (SI)
Ant	C24o	-61.7150	136.5670	Tikku and Cande (SI)
Ant	C24o	-61.6270	136.8140	Tikku and Cande (SI)
Ant	C24o	-61.5570	137.7970	Tikku and Cande (SI)
Ant	C24o	-61.5500	138.2090	Tikku and Cande (SI)
Ant	C24o	-61.4950	138.5640	Tikku and Cande (SI)
Ant	C24o	-61.4250	138.9270	Tikku and Cande (SI)
Ant	C24o	-61.5590	140.0350	Tikku and Cande (SI)
Aus	C24o	-37.4260	120.7320	Tikku and Cande (SI)
Aus	C24o	-37.3560	121.1570	Tikku and Cande (SI)
Aus	C24o	-37.3870	122.0740	Tikku and Cande (SI)
Aus	C24o	-37.3460	122.5870	Tikku and Cande (SI)
Aus	C24o	-37.4240	123.3160	Tikku and Cande (SI)
Aus	C24o	-37.2210	125.3900	Tikku and Cande (SI)
Aus	C24o	-37.1450	126.2210	Tikku and Cande (SI)
Aus	C24o	-37.0840	127.9730	Tikku and Cande (SI)
Aus	C24o	-37.1990	129.4180	Tikku and Cande (SI)
Aus	C24o	-37.1530	130.8380	Tikku and Cande (SI)
Aus	C24o	-37.2780	131.6830	Tikku and Cande (SI)
Aus	C24o	-37.2660	132.0780	Tikku and Cande (SI)
Aus	C24o	-37.1820	132.1140	Tikku and Cande (SI)
Aus	C24o	-37.3410	132.5080	Tikku and Cande (SI)
Aus	C24o	-37.4440	132.8170	Tikku and Cande (SI)
Aus	C24o	-37.3260	134.6510	Tikku and Cande (SI)
Aus	C24o	-37.3600	135.4790	Tikku and Cande (SI)
Ant	C27y	-61.8006	104.0303	GA-22815

Ant	C27y	-62.0318	104.8472	RAE-5002
Ant	C27y	-62.0404	104.9677	GA-22917
Ant	C27y	-62.1109	107.3241	GA-22817
Ant	C27y	-62.2663	108.2057	RAE-5003
Ant	C27y	-62.1635	109.0830	GA-22915
Ant	C27y	-62.0305	110.2528	RAE-5004
Ant	C27y	-62.0509	110.7668	GA-22818
Ant	C27y	-62.0010	110.8350	Tikku and Cande (SI)
Ant	C27y	-61.9740	112.0000	Tikku and Cande (SI)
Ant	C27y	-62.0350	112.5250	Tikku and Cande (SI)
Ant	C27y	-62.0161	113.0443	RAE-5005
Ant	C27y	-62.0849	113.2663	GA-22913
Ant	C27y	-62.0400	113.5000	Tikku and Cande (SI)
Ant	C27y	-62.1260	114.1448	GA-22819
Ant	C27y	-62.1600	114.2910	Tikku and Cande (SI)
Ant	C27y	-62.2920	114.4990	Tikku and Cande (SI)
Ant	C27y	-62.2685	114.7939	RAE-5006
Ant	C27y	-62.2439	115.4320	RAE-50067
Ant	C27y	-62.2920	115.9990	Tikku and Cande (SI)
Ant	C27y	-62.2452	116.4880	GA-22912
Ant	C27y	-62.2070	117.0000	Tikku and Cande (SI)
Ant	C27y	-62.0925	117.4999	GA-22820
Ant	C27y	-62.2040	118.0000	Tikku and Cande (SI)
Ant	C27y	-62.0740	119.0490	GA-22911
Ant	C27y	-62.1270	119.9600	Tikku and Cande (SI)
Ant	C27y	-62.0300	120.0510	Tikku and Cande (SI)
Ant	C27y	-62.0152	120.8671	GA-22821
Ant	C27y	-61.9300	121.0990	Tikku and Cande (SI)
Ant	C27y	-61.9260	121.1740	Tikku and Cande (SI)
Ant	C27y	-61.9043	122.5500	GA-22908
Ant	C27y	-62.0370	123.8820	Tikku and Cande (SI)
Ant	C27y	-62.0262	124.2330	GA-22822
Ant	C27y	-62.1220	125.8030	Tikku and Cande (SI)
Ant	C27y	-62.1436	125.9161	GA-22823
Ant	C27y	-62.0970	126.7390	Tikku and Cande (SI)
Ant	C27y	-62.1070	126.8200	Tikku and Cande (SI)
Ant	C27y	-62.1294	127.6003	GA-22824
Ant	C27y	-62.1430	127.7870	Tikku and Cande (SI)
Ant	C27y	-62.0295	129.2831	GA-22825
Ant	C27y	-62.1970	130.5950	Tikku and Cande (SI)
Ant	C27y	-62.3000	131.9660	Tikku and Cande (SI)
Ant	C27y	-62.2120	132.0480	Tikku and Cande (SI)
Aus	C27y	-37.3440	120.6470	Tikku and Cande (SI)
Aus	C27y	-37.2530	121.1130	Tikku and Cande (SI)
Aus	C27y	-37.2100	121.4500	Tikku and Cande (SI)
Aus	C27y	-37.1820	121.6190	Tikku and Cande (SI)
Aus	C27y	-37.2480	122.5880	Tikku and Cande (SI)
Aus	C27y	-37.2850	123.3300	Tikku and Cande (SI)
Aus	C27y	-37.2700	123.5060	Tikku and Cande (SI)
Aus	C27y	-37.0690	125.3120	Tikku and Cande (SI)
Aus	C27y	-36.9560	126.3630	Tikku and Cande (SI)
Aus	C27y	-36.9040	126.4620	Tikku and Cande (SI)
Aus	C27y	-36.7740	127.9660	Tikku and Cande (SI)
Aus	C27y	-36.8770	129.0510	Tikku and Cande (SI)
Aus	C27y	-36.9370	129.4320	Tikku and Cande (SI)
Aus	C27y	-36.9050	129.6070	Tikku and Cande (SI)
Aus	C27y	-36.9960	130.8590	Tikku and Cande (SI)
Aus	C27y	-36.9580	132.0710	Tikku and Cande (SI)
Aus	C27y	-37.2130	132.7730	Tikku and Cande (SI)
Aus	C27y	-37.1760	132.8000	Tikku and Cande (SI)

Aus	C27y	-37.2050	132.8520	Tikku and Cande (SI)
Aus	C27y	-36.9100	134.0680	Tikku and Cande (SI)
Ant	C31o	-61.8544	104.0128	GA-22815
Ant	C31o	-62.0897	104.8115	GA-22917
Ant	C31o	-62.1039	104.8586	RAE-5002
Ant	C31o	-62.1705	107.2990	GA-22817
Ant	C31o	-62.4147	108.2180	RAE-5003
Ant	C31o	-62.4364	108.3978	GA-22915
Ant	C31o	-62.2020	110.2650	RAE-5004
Ant	C31o	-62.1733	110.7669	GA-22818
Ant	C31o	-62.1720	110.8330	Tikku and Cande (SI)
Ant	C31o	-62.1030	111.9990	Tikku and Cande (SI)
Ant	C31o	-62.1250	112.4130	Tikku and Cande (SI)
Ant	C31o	-62.1464	113.0579	RAE-5005
Ant	C31o	-62.1541	113.4680	GA-22913
Ant	C31o	-62.2220	113.9750	Tikku and Cande (SI)
Ant	C31o	-62.2741	114.1466	GA-22819
Ant	C31o	-62.3835	114.7837	RAE-5006
Ant	C31o	-62.3614	115.4233	RAE-50067
Ant	C31o	-62.3940	115.9990	Tikku and Cande (SI)
Ant	C31o	-62.4164	116.7520	GA-22912
Ant	C31o	-62.3161	117.5000	GA-22820
Ant	C31o	-62.3300	118.0000	Tikku and Cande (SI)
Ant	C31o	-62.2657	118.6971	GA-22911
Ant	C31o	-62.2600	119.8430	Tikku and Cande (SI)
Ant	C31o	-62.2480	120.4120	Tikku and Cande (SI)
Ant	C31o	-62.1632	120.8673	GA-22821
Ant	C31o	-62.1100	121.1050	Tikku and Cande (SI)
Ant	C31o	-62.0549	122.6309	GA-22908
Ant	C31o	-62.1360	123.8690	Tikku and Cande (SI)
Ant	C31o	-62.1730	124.2329	GA-22822
Ant	C31o	-62.2360	125.0980	Tikku and Cande (SI)
Ant	C31o	-62.2391	125.9161	GA-22823
Ant	C31o	-62.2530	126.8130	Tikku and Cande (SI)
Ant	C31o	-62.2460	126.8230	Tikku and Cande (SI)
Ant	C31o	-62.2605	127.6003	GA-22824
Ant	C31o	-62.2730	127.7730	Tikku and Cande (SI)
Ant	C31o	-62.1618	129.2832	GA-22825
Ant	C31o	-62.2840	130.5340	Tikku and Cande (SI)
Ant	C31o	-62.4330	131.9820	Tikku and Cande (SI)
Ant	C31o	-62.3790	132.0390	Tikku and Cande (SI)
Aus	C31o	-37.2720	120.5560	Tikku and Cande (SI)
Aus	C31o	-37.1330	121.0620	Tikku and Cande (SI)
Aus	C31o	-37.0900	121.4280	Tikku and Cande (SI)
Aus	C31o	-37.0550	121.7750	Tikku and Cande (SI)
Aus	C31o	-37.1630	122.5890	Tikku and Cande (SI)
Aus	C31o	-37.1880	123.4420	Tikku and Cande (SI)
Aus	C31o	-37.1280	123.6840	Tikku and Cande (SI)
Aus	C31o	-36.9750	125.2640	Tikku and Cande (SI)
Aus	C31o	-36.8070	126.3550	Tikku and Cande (SI)
Aus	C31o	-36.8070	126.3970	Tikku and Cande (SI)
Aus	C31o	-36.7690	126.4980	Tikku and Cande (SI)
Aus	C31o	-36.6810	127.9690	Tikku and Cande (SI)
Aus	C31o	-36.7740	128.9680	Tikku and Cande (SI)
Aus	C31o	-36.7740	129.4350	Tikku and Cande (SI)
Aus	C31o	-36.8060	129.6170	Tikku and Cande (SI)
Aus	C31o	-36.8240	130.8800	Tikku and Cande (SI)
Aus	C31o	-36.9240	132.2490	Tikku and Cande (SI)
Aus	C31o	-37.0880	132.6060	Tikku and Cande (SI)
Aus	C31o	-37.0630	132.7960	Tikku and Cande (SI)

Aus	C31o	-36.7150	134.4360	Tikku and Cande (<i>SI</i>)
Ant	C32y	-61.9911	103.9680	GA-22815
Ant	C32y	-62.1404	104.6700	GA-22917
Ant	C32y	-62.2613	104.8829	RAE-5002
Ant	C32y	-62.2950	107.2462	GA-22817
Ant	C32y	-62.6003	107.7154	GA-22915
Ant	C32y	-62.5982	108.2578	RAE-5003
Ant	C32y	-62.3234	110.2747	RAE-5004
Ant	C32y	-62.3264	110.7667	GA-22818
Ant	C32y	-62.3440	110.8340	Tikku and Cande (<i>SI</i>)
Ant	C32y	-62.2340	111.9980	Tikku and Cande (<i>SI</i>)
Ant	C32y	-62.3120	112.1900	Tikku and Cande (<i>SI</i>)
Ant	C32y	-62.4110	112.9950	Tikku and Cande (<i>SI</i>)
Ant	C32y	-62.3274	113.0754	RAE-5005
Ant	C32y	-62.4130	113.5000	Tikku and Cande (<i>SI</i>)
Ant	C32y	-62.5832	114.3213	GA-22819
Ant	C32y	-62.6000	114.5000	Tikku and Cande (<i>SI</i>)
Ant	C32y	-62.5322	114.7707	RAE-5006
Ant	C32y	-62.5217	115.4150	RAE-5006
Ant	C32y	-62.5990	116.0000	Tikku and Cande (<i>SI</i>)
Ant	C32y	-62.4690	117.0000	Tikku and Cande (<i>SI</i>)
Ant	C32y	-62.6156	117.0482	GA-22912
Ant	C32y	-62.4240	117.4998	GA-22820
Ant	C32y	-62.5250	117.9990	Tikku and Cande (<i>SI</i>)
Ant	C32y	-62.5302	118.2362	GA-22911
Ant	C32y	-62.4600	119.6750	Tikku and Cande (<i>SI</i>)
Ant	C32y	-62.4460	119.9260	Tikku and Cande (<i>SI</i>)
Ant	C32y	-62.3600	120.0040	Tikku and Cande (<i>SI</i>)
Ant	C32y	-62.3315	120.8672	GA-22821
Ant	C32y	-62.2320	121.0920	Tikku and Cande (<i>SI</i>)
Ant	C32y	-62.4346	123.1990	GA-22908
Ant	C32y	-62.3690	123.8310	Tikku and Cande (<i>SI</i>)
Ant	C32y	-62.3772	124.2329	GA-22822
Ant	C32y	-62.2930	124.7230	Tikku and Cande (<i>SI</i>)
Ant	C32y	-62.4300	125.9163	GA-22823
Ant	C32y	-62.4020	126.8460	Tikku and Cande (<i>SI</i>)
Ant	C32y	-62.4300	126.9190	Tikku and Cande (<i>SI</i>)
Ant	C32y	-62.3916	127.6003	GA-22824
Ant	C32y	-62.3890	127.7470	Tikku and Cande (<i>SI</i>)
Ant	C32y	-62.2808	129.2833	GA-22825
Ant	C32y	-62.5650	130.8330	Tikku and Cande (<i>SI</i>)
Ant	C32y	-62.4870	130.3990	Tikku and Cande (<i>SI</i>)
Ant	C32y	-62.5470	131.9930	Tikku and Cande (<i>SI</i>)
Ant	C32y	-62.4820	132.0340	Tikku and Cande (<i>SI</i>)
Aus	C32y	-37.6280	117.4840	Tikku and Cande (<i>SI</i>)
Aus	C32y	-37.6250	117.5990	Tikku and Cande (<i>SI</i>)
Aus	C32y	-37.7530	118.1710	Tikku and Cande (<i>SI</i>)
Aus	C32y	-37.6710	118.5840	Tikku and Cande (<i>SI</i>)
Aus	C32y	-37.5220	119.3440	Tikku and Cande (<i>SI</i>)
Aus	C32y	-37.4360	119.6630	Tikku and Cande (<i>SI</i>)
Aus	C32y	-37.1930	120.4530	Tikku and Cande (<i>SI</i>)
Aus	C32y	-37.0450	121.0250	Tikku and Cande (<i>SI</i>)
Aus	C32y	-37.2000	120.4950	Tikku and Cande (<i>SI</i>)
Aus	C32y	-36.9240	121.9290	Tikku and Cande (<i>SI</i>)
Aus	C32y	-36.9660	123.5510	Tikku and Cande (<i>SI</i>)
Aus	C32y	-36.9100	123.9570	Tikku and Cande (<i>SI</i>)
Aus	C32y	-36.8870	125.2140	Tikku and Cande (<i>SI</i>)
Aus	C32y	-36.7030	126.2400	Tikku and Cande (<i>SI</i>)
Aus	C32y	-36.7000	126.3950	Tikku and Cande (<i>SI</i>)
Aus	C32y	-36.4780	127.1490	Tikku and Cande (<i>SI</i>)

Aus	C32y	-36.5480	127.9740	Tikku and Cande (SI)
Aus	C32y	-36.6450	128.8850	Tikku and Cande (SI)
Aus	C32y	-36.6390	129.4360	Tikku and Cande (SI)
Aus	C32y	-36.6320	129.6190	Tikku and Cande (SI)
Aus	C32y	-36.5920	130.9020	Tikku and Cande (SI)
Aus	C32y	-36.6590	132.0360	Tikku and Cande (SI)
Aus	C32y	-36.8760	132.5250	Tikku and Cande (SI)
Aus	C32y	-36.8310	132.5420	Tikku and Cande (SI)
Aus	C32y	-36.9590	132.8050	Tikku and Cande (SI)
Ant	C33o	-62.0445	103.9503	GA-22815
Ant	C33o	-62.1896	104.4910	GA-22917
Ant	C33o	-62.3662	104.8998	RAE-5002
Ant	C33o	-62.4415	107.1888	GA-22817
Ant	C33o	-62.7450	108.0110	Tikku and Cande (SI)
Ant	C33o	-62.8326	108.2580	RAE-5003
Ant	C33o	-62.7090	109.5010	Tikku and Cande (SI)
Ant	C33o	-62.5663	110.2921	RAE-5004
Ant	C33o	-62.5330	110.7666	GA-22818
Ant	C33o	-62.5690	110.8330	Tikku and Cande (SI)
Ant	C33o	-62.6150	111.7400	Tikku and Cande (SI)
Ant	C33o	-62.6270	111.8280	Tikku and Cande (SI)
Ant	C33o	-62.5090	112.0010	Tikku and Cande (SI)
Ant	C33o	-62.5736	113.0990	RAE-5005
Ant	C33o	-62.6830	113.5000	Tikku and Cande (SI)
Ant	C33o	-62.8370	114.5000	Tikku and Cande (SI)
Ant	C33o	-62.8566	114.7394	RAE-5006
Ant	C33o	-62.9550	114.8248	GA-22819
Ant	C33o	-62.8475	115.3931	RAE-50067
Ant	C33o	-62.9330	116.0010	Tikku and Cande (SI)
Ant	C33o	-62.8580	117.0000	Tikku and Cande (SI)
Ant	C33o	-62.8267	117.3500	GA-22912
Ant	C33o	-62.7787	117.5000	GA-22820
Ant	C33o	-62.7456	117.7754	GA-22911
Ant	C33o	-62.7800	118.0010	Tikku and Cande (SI)
Ant	C33o	-62.8280	119.2110	Tikku and Cande (SI)
Ant	C33o	-62.7860	119.9440	Tikku and Cande (SI)
Ant	C33o	-62.6545	120.8672	GA-22821
Ant	C33o	-62.5920	121.0950	Tikku and Cande (SI)
Ant	C33o	-62.5990	122.4310	Tikku and Cande (SI)
Ant	C33o	-62.5695	123.4057	GA-22908
Ant	C33o	-62.6310	123.8990	Tikku and Cande (SI)
Ant	C33o	-62.5879	124.2331	GA-22822
Ant	C33o	-62.6356	125.9164	GA-22823
Ant	C33o	-62.7170	126.9010	Tikku and Cande (SI)
Ant	C33o	-62.8600	127.1790	Tikku and Cande (SI)
Ant	C33o	-62.6608	127.6002	GA-22824
Ant	C33o	-62.6980	127.7480	Tikku and Cande (SI)
Ant	C33o	-62.7041	129.2833	GA-22825
Ant	C33o	-62.6860	130.2670	Tikku and Cande (SI)
Ant	C33o	-62.8100	132.0170	Tikku and Cande (SI)
Ant	C33o	-63.0090	132.0950	Tikku and Cande (SI)
Aus	C33o	-37.4990	117.3800	Tikku and Cande (SI)
Aus	C33o	-37.5350	117.5190	Tikku and Cande (SI)
Aus	C33o	-37.5210	117.9220	Tikku and Cande (SI)
Aus	C33o	-37.5410	118.4350	Tikku and Cande (SI)
Aus	C33o	-37.4200	119.1080	Tikku and Cande (SI)
Aus	C33o	-37.3570	119.5780	Tikku and Cande (SI)
Aus	C33o	-37.1160	120.3520	Tikku and Cande (SI)
Aus	C33o	-36.8680	120.9500	Tikku and Cande (SI)
Aus	C33o	-36.9590	120.7270	Tikku and Cande (SI)

Aus	C33o	-36.7830	122.1210	Tikku and Cande (SI)
Aus	C33o	-36.8170	123.5830	Tikku and Cande (SI)
Aus	C33o	-36.7830	124.1210	Tikku and Cande (SI)
Aus	C33o	-36.5610	125.0470	Tikku and Cande (SI)
Aus	C33o	-36.5030	126.0300	Tikku and Cande (SI)
Aus	C33o	-36.3990	126.3810	Tikku and Cande (SI)
Aus	C33o	-36.1650	127.0780	Tikku and Cande (SI)
Aus	C33o	-36.1750	127.9830	Tikku and Cande (SI)
Aus	C33o	-36.2340	128.6370	Tikku and Cande (SI)
Aus	C33o	-36.2420	129.4220	Tikku and Cande (SI)
Aus	C33o	-36.3620	129.6040	Tikku and Cande (SI)
Aus	C33o	-36.3110	130.9550	Tikku and Cande (SI)
Aus	C33o	-36.3430	131.6180	Tikku and Cande (SI)
Aus	C33o	-36.2440	131.7340	Tikku and Cande (SI)
Aus	C33o	-36.3870	132.2550	Tikku and Cande (SI)
Aus	C33o	-36.5630	132.8020	Tikku and Cande (SI)
Aus	C33o	-36.5920	133.2220	Tikku and Cande (SI)
Aus	C33o	-36.7500	133.5610	Tikku and Cande (SI)
Ant	C34y	-61.6723	102.3500	GA-22919
Ant	C34y	-62.0864	103.9365	GA-22815
Ant	C34y	-62.2383	104.3330	GA-22817
Ant	C34y	-62.2613	104.8829	RAE-5002
Ant	C34y	-63.0320	108.0010	Tikku and Cande (SI)
Ant	C34y	-63.0242	108.2770	RAE-5003
Ant	C34y	-62.8660	109.4990	Tikku and Cande (SI)
Ant	C34y	-62.8086	110.3090	RAE-5004
Ant	C34y	-62.9130	110.3170	Tikku and Cande (SI)
Ant	C34y	-62.8350	110.8330	Tikku and Cande (SI)
Ant	C34y	-62.8270	110.9913	GA-22818
Ant	C34y	-62.9540	111.3600	Tikku and Cande (SI)
Ant	C34y	-63.0810	112.6660	Tikku and Cande (SI)
Ant	C34y	-63.0801	113.1517	RAE-5005
Ant	C34y	-63.1070	113.5000	Tikku and Cande (SI)
Ant	C34y	-63.2030	114.5000	Tikku and Cande (SI)
Ant	C34y	-63.2216	114.7044	RAE-5006
Ant	C34y	-63.2059	115.1733	GA-22819
Ant	C34y	-63.1948	115.3702	RAE-50067
Ant	C34y	-63.2390	116.0000	Tikku and Cande (SI)
Ant	C34y	-63.1290	117.0000	Tikku and Cande (SI)
Ant	C34y	-63.1562	117.4897	GA-22820
Ant	C34y	-63.1430	118.0000	Tikku and Cande (SI)
Ant	C34y	-63.1380	118.8690	Tikku and Cande (SI)
Ant	C34y	-63.1750	118.9510	Tikku and Cande (SI)
Ant	C34y	-63.1260	119.8940	Tikku and Cande (SI)
Ant	C34y	-62.9842	120.8670	GA-22821
Ant	C34y	-62.9460	123.9810	Tikku and Cande (SI)
Ant	C34y	-62.9382	123.9816	GA-22908
Ant	C34y	-62.8943	124.2332	GA-22822
Ant	C34y	-62.9000	125.9164	GA-22823
Ant	C34y	-63.0450	127.0510	Tikku and Cande (SI)
Ant	C34y	-63.1100	127.3390	Tikku and Cande (SI)
Ant	C34y	-63.1054	127.6549	GA-22824
Ant	C34y	-63.0960	127.7820	Tikku and Cande (SI)
Ant	C34y	-62.9842	129.3701	GA-22825
Ant	C34y	-63.1920	130.4990	Tikku and Cande (SI)
Ant	C34y	-63.2530	131.9140	Tikku and Cande (SI)
Ant	C34y	-63.2670	132.2300	Tikku and Cande (SI)
Aus	C34y	-37.2940	117.6760	Tikku and Cande (SI)
Aus	C34y	-37.2720	118.1200	Tikku and Cande (SI)
Aus	C34y	-37.3360	118.7920	Tikku and Cande (SI)

Aus	C34y	-37.3050	119.0760	Tikku and Cande (SI)
Aus	C34y	-37.2260	119.4350	Tikku and Cande (SI)
Aus	C34y	-36.9530	120.1840	Tikku and Cande (SI)
Aus	C34y	-36.7650	120.9120	Tikku and Cande (SI)
Aus	C34y	-36.6990	121.0110	Tikku and Cande (SI)
Aus	C34y	-36.6010	122.0250	Tikku and Cande (SI)
Aus	C34y	-36.5620	122.4540	Tikku and Cande (SI)
Aus	C34y	-36.5700	123.1480	Tikku and Cande (SI)
Aus	C34y	-36.5360	123.5670	Tikku and Cande (SI)
Aus	C34y	-36.5050	124.2670	Tikku and Cande (SI)
Aus	C34y	-36.3370	124.9130	Tikku and Cande (SI)
Aus	C34y	-36.2260	125.7390	Tikku and Cande (SI)
Aus	C34y	-35.9920	126.3550	Tikku and Cande (SI)
Aus	C34y	-36.0100	126.7850	Tikku and Cande (SI)
Aus	C34y	-36.0460	126.9040	Tikku and Cande (SI)
Aus	C34y	-36.0120	127.2400	Tikku and Cande (SI)
Aus	C34y	-35.9400	127.9360	Tikku and Cande (SI)
Aus	C34y	-36.0030	128.4990	Tikku and Cande (SI)
Aus	C34y	-35.9470	129.3570	Tikku and Cande (SI)
Aus	C34y	-35.9960	129.5470	Tikku and Cande (SI)
Aus	C34y	-35.9660	130.7300	Tikku and Cande (SI)
Aus	C34y	-36.0710	131.0040	Tikku and Cande (SI)
Aus	C34y	-36.0790	131.2700	Tikku and Cande (SI)
Ant	QZB	-62.8140	102.7073	Gravity
Ant	QZB	-62.9762	103.6671	Gravity
Ant	QZB	-63.2339	104.7690	Gravity
Ant	QZB	-63.3778	106.2620	Gravity
Ant	QZB	-63.4892	107.8617	Gravity
Ant	QZB	-63.4256	109.3547	Gravity
Ant	QZB	-63.4733	110.6344	Gravity
Ant	QZB	-63.5210	112.1629	Gravity
Ant	QZB	-63.5686	113.7981	Gravity
Ant	QZB	-63.7266	114.9001	Gravity
Ant	QZB	-63.7580	116.5352	Gravity
Ant	QZB	-63.6792	118.4903	Gravity
Ant	QZB	-63.6160	120.3388	Gravity
Ant	QZB	-63.6002	121.6896	Gravity
Ant	QZB	-63.6076	121.8335	Gravity
Ant	QZB	-63.6240	122.1739	Gravity
Ant	QZB	-63.6403	122.5744	Gravity
Ant	QZB	-63.6477	122.8982	Gravity
Ant	QZB	-63.6625	123.2887	Gravity
Ant	QZB	-63.6950	123.8358	Gravity
Ant	QZB	-63.7124	124.1004	Gravity
Ant	QZB	-63.7275	124.3229	Gravity
Ant	QZB	-63.7382	124.4763	Gravity
Ant	QZB	-63.7423	124.5334	Gravity
Ant	QZB	-63.8209	126.3819	Gravity
Ant	QZB	-63.7895	127.5549	Gravity
Ant	QZB	-63.7580	128.8702	Gravity
Ant	QZB	-63.6160	129.8655	Gravity
Ant	QZB	-63.6477	131.8206	Gravity
Ant	QZB	-63.7423	133.9535	Gravity
Ant	QZB	-63.8837	136.7617	Gravity
Ant	QZB	-64.1177	139.0012	Gravity
Ant	QZB	-64.2263	140.6364	Gravity
Ant	QZB	-64.5034	142.3071	Gravity
Ant	QZB	-64.7930	143.8712	Gravity
Ant	QZB	-65.1991	145.7908	Gravity
Ant	QZB	-65.4517	147.3904	Gravity

Ant	QZB	-65.6579	148.8479	Gravity
Ant	QZB	-65.7896	149.8787	Gravity
Aus	QZB	-37.1228	117.3528	Gravity
Aus	QZB	-36.9804	117.9927	Gravity
Aus	QZB	-37.1228	118.7747	Gravity
Aus	QZB	-36.8948	119.3790	Gravity
Aus	QZB	-36.7233	120.1255	Gravity
Aus	QZB	-36.5227	120.7298	Gravity
Aus	QZB	-36.3503	121.5119	Gravity
Aus	QZB	-36.1200	122.1873	Gravity
Aus	QZB	-36.2064	122.7205	Gravity
Aus	QZB	-36.2352	123.2537	Gravity
Aus	QZB	-36.1776	124.0357	Gravity
Aus	QZB	-36.0045	124.9244	Gravity
Aus	QZB	-35.7731	125.5998	Gravity
Aus	QZB	-35.6281	126.4174	Gravity
Aus	QZB	-35.4829	127.0217	Gravity
Aus	QZB	-35.4247	127.5549	Gravity
Aus	QZB	-35.3956	128.5147	Gravity
Aus	QZB	-35.4829	129.9011	Gravity
Aus	QZB	-35.5410	130.5765	Gravity
Aus	QZB	-35.6861	131.9628	Gravity
Aus	QZB	-35.9467	133.3492	Gravity
Aus	QZB	-36.1488	134.5578	Gravity
Aus	QZB	-36.3791	135.3754	Gravity
Aus	QZB	-36.7233	136.2996	Gravity
Aus	QZB	-37.0089	137.1528	Gravity
Aus	QZB	-37.2650	137.7215	Gravity

Table S3: Finite rotations for East Antarctica-Australia (Antarctica fixed). Finite rotations were computed following the methods of Hellinger (S7) and Royer and Chang (S8). Parameters: r , misfit; $\hat{\kappa}$, estimated quality factor; dF , degrees of freedom; N , number of data points; s , number of great circle segments; the uncertainty of fracture zone is $\sigma = 5.0$ km following Müller et al. (S9), magnetic anomaly identifications is $\sigma = 5.5$ km for chrons 20-31 and $\sigma = 9.0$ km for chrons 32-34, and gravity anomaly identifications (QZB – Quiet Zone Boundary) is $\sigma = 15$ km; ages are after Cande and Kent (S10) timescale.

Chron	Age Ma	Latitude +°N	Longitude °E	Angle °	r (km)	$\hat{\kappa}$	dF	N	s
20o	43.79	14.92	32.50	24.51	55.37	0.74	41	58	7
21y	46.26	13.60	33.60	24.64	8.83	3.06	27	42	6
24o	53.35	9.01	36.00	25.06	36.26	0.99	36	53	7
27y	60.92	5.51	38.57	25.30	44.92	0.73	33	48	6
31o	68.74	3.97	39.11	25.51	25.21	1.19	34	49	6
32y	71.07	1.04	40.65	25.85	47.21	0.83	53	72	8
33o	79.08	-3.54	42.94	26.58	79.80	0.58	62	79	7
34y	83.00	-7.69	44.79	27.49	48.36	0.79	48	67	8
QZB	96.00	-12.69	46.58	29.06	45.45	1.03	47	66	8

Table S4: Covariance matrices for finite rotations in Table S3.
The covariance matrix is given by the formula

$$\frac{1}{\hat{\kappa}} * \begin{pmatrix} a & b & c \\ b & d & e \\ c & e & f \end{pmatrix} \times 10^{-g} \text{ where the values of a-f are given in radians squared.}$$

Chron	$\hat{\kappa}$	a	b	c	d	e	f	g
20o	0.74	0.63	-0.10	1.68	1.87	-3.10	6.76	6
21y	3.06	2.96	-4.16	9.41	6.19	-13.70	32.21	6
24o	0.99	1.35	-1.92	3.43	3.00	-5.54	12.88	6
27y	0.73	2.76	-4.03	9.38	6.20	-14.58	41.14	6
31o	1.19	3.68	-5.41	12.75	8.26	-19.41	53.67	6
32y	0.83	2.88	-4.50	8.96	7.82	-16.47	47.01	6
33o	0.58	1.67	-2.87	5.78	5.58	-11.62	30.02	6
34y	0.79	2.61	-4.23	8.12	7.52	-14.86	33.00	6
QZB	1.03	3.53	-4.06	8.19	6.09	-13.50	35.71	6

Table S5: Plate reconstructions before Izanagi-Pacific Ridge subduction involve recreating the now entirely subducted Izanagi oceanic plate. Our reconstructions (Figure 4) utilise the following assumptions:

Assumption	Explanation
Symmetrical Spreading	Subduction of the Izanagi plate at eastern Asian subduction zones means the only record of Izanagi spreading is contained in Pacific oceanic crust. Lacking the Izanagi oceanic flank we have assumed symmetrical spreading about the Izanagi-Pacific ridge. This is a reasonable assumption given that Müller et al. (<i>S11</i>) found the maximum observable cumulative ridge asymmetry to be approximately 10% globally.
Steady spreading rate	Due to the lack of magnetic reversals during the Cretaceous Quiet Zone the spreading rate of the Izanagi-Pacific plate pair from 118 Ma to 83 Ma cannot be determined directly. However, Late Jurassic to Early Cretaceous M-series magnetic anomalies in the west-central Pacific Ocean show no variation in spreading rate for at least 10 million years prior to the Cretaceous Normal Superchon (<i>S12</i>). With no other evidence for a change in spreading rate from the Pacific-Farallon or Pacific-Phoenix plate pairs, or other data, we have assumed that the Izanagi-Pacific M-sequence spreading rate continued throughout the Cretaceous Normal Superchon.

References

- S1. A. A. Tikku, S. C. Cande, *Journal of Geophysical Research* **104**, 661 (1999).
- S2. V. Mendel, M. Munsch, D. Sauter, *Computers & Geosciences* **31**, 589 (2005).
- S3. P. O'Brien, S. Stanley, R. Parums, in *Antarctica: Contributions to Global Earth Sciences* D. K. Fütterer, D. Damaske, G. Kleinschmidt, H. Miller, F. Tessensohn, Eds. (Springer-Verlag, Berlin, 2006) pp. 341-347.
- S4. H. M. J. Stagg *et al.*, "Geological framework of the continental margin in the region of the Australian Antarctic Territory" (Geoscience Australia Record 2005).
- S5. J. B. Colwell, H. M. J. Stagg, N. G. Direen, G. Bernardel, I. Borissova, in *Antarctica: Contributions to Global Earth Sciences* D. K. Fütterer, D. Damaske, G. Kleinschmidt, H. Miller, F. Tessensohn, Eds. (Springer-Verlag, Berlin, 2006) pp. 327-340.
- S6. D. I. Close, H. M. J. Stagg, P. E. O'Brien, *Marine Geology* **239**, 33 (2007).
- S7. S. J. Hellinger, *Journal of Geophysical Research* **86**, 9312 (1981).
- S8. J.-Y. Royer, T. Chang, *Journal of Geophysical Research* **96**, 11779 (1991).
- S9. R. D. Müller, D. T. Sandwell, B. E. Tucholke, J. G. Sclater, P. R. Shaw, *Marine Geophysical Researches* **13**, 105 (1991).
- S10. S. C. Cande, D. V. Kent, *Journal of Geophysical Research* **100**, 6093 (1995).
- S11. R. D. Müller, W. R. Roest, J.-Y. Royer, *Nature* **396**, 455 (1998).
- S12. M. Nakanishi, K. Tamaki, K. Kobayashi, *Geophysical Research Letters* **19**, 693 (1992).

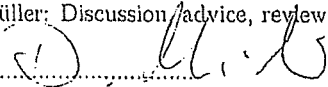
Appendix C

Co-author contribution forms

Statement identifying co-author contributions to published works

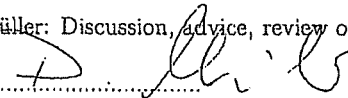
The University of Sydney policy states that candidates must provide evidence to identify the sections of work for which the candidate is responsible. The work and interpretations in Paper 2 Whittaker, J.M. and Müller, R.D., (2006) Seismic stratigraphy of the Adare Trough area, Antarctica. *Marine Geology*, 230(3-4): 179-197 are the work of the author except where stated below:

Dietmar Müller: Discussion, advice, review of manuscript

Signature: 

The work and interpretations in Paper 3 Whittaker, J., Müller, R.D., Sdrolias, M. and Heine, C., (2007) Sunda-Java trench kinematics, slab window formation and overriding plate deformation since the Cretaceous, *Earth and Planetary Science Letters*. 255: 445-457 are the work of the author except where stated below:

Dietmar Müller: Discussion, advice, review of manuscript

Signature: 

Maria Sdrolias: Methodology, discussion, advice, review of manuscript

Signature: 

Christian Heine: Discussion, advice, review of manuscript

Signature: 

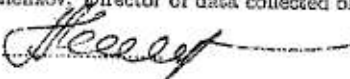
Statement identifying co-author contributions to published works

The University of Sydney policy states that candidates must provide evidence to identify the sections of work for which the candidate is responsible. The interpretations in Paper 4 Whittaker, J. M., Müller, R.D., Leitchenkov, G., Stagg, H., Scholias, M., Gaina, C. and Goncharov, A. (2007) Major Australian Antarctic Plate Reorganisation at Hawaiian-Emperor Bend Time, Science 318: 83-86 are the work of the author except where stated below:

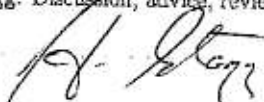
Dietmar Müller: Discussion, advice, review of manuscript

Signature: 


German Leitchenkov: Director of data collected offshore Antarctica, review of manuscript

Signature: 

Howard Stagg: Discussion, advice, review of manuscript

Signature: 

Maria Scholias: Discussion, advice, review of manuscript

Signature: 

Carmen Gaina: Review of manuscript

Signature: 

Alexey Goncharov: Discussion, advice, review of manuscript

Signature: 